

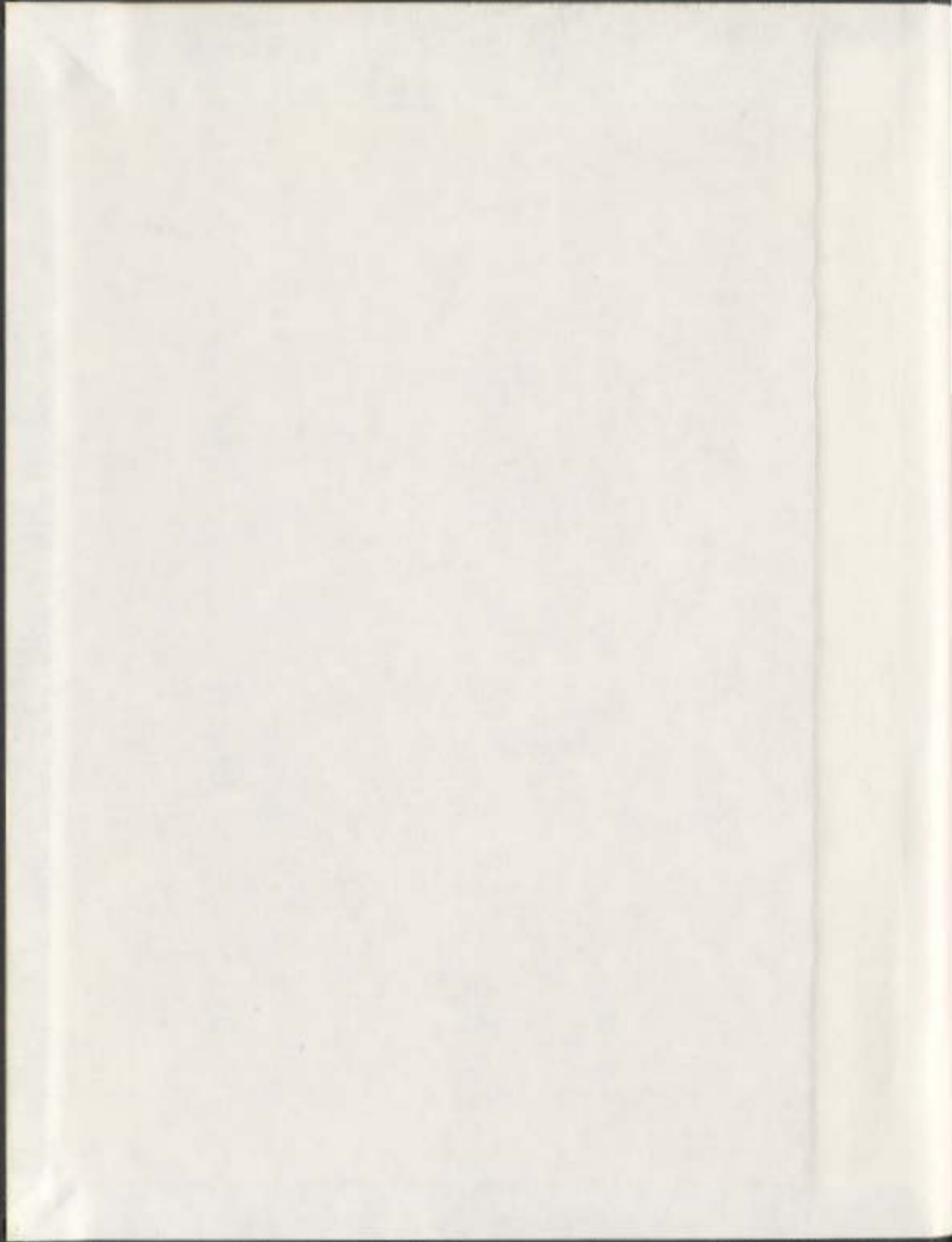
DEUTERIUM NUCLEAR MAGNETIC RESONANCE
SPECTROSCOPY AND MOLECULAR DYNAMICS STUDIES
OF TRANSMEMBRANE POLYPEPTIDES

CENTRE FOR NEWFOUNDLAND STUDIES

**TOTAL OF 10 PAGES ONLY
MAY BE XEROXED**

(Without Author's Permission)

DAVID J. GOODYEAR





Library and
Archives Canada

Bibliothèque et
Archives Canada

Published Heritage
Branch

Direction du
Patrimoine de l'édition

395 Wellington Street
Ottawa ON K1A 0N4
Canada

395, rue Wellington
Ottawa ON K1A 0N4
Canada

Your file *Votre référence*

ISBN: 0-612-99034-6

Our file *Notre référence*

ISBN: 0-612-99034-6

NOTICE:

The author has granted a non-exclusive license allowing Library and Archives Canada to reproduce, publish, archive, preserve, conserve, communicate to the public by telecommunication or on the Internet, loan, distribute and sell theses worldwide, for commercial or non-commercial purposes, in microform, paper, electronic and/or any other formats.

The author retains copyright ownership and moral rights in this thesis. Neither the thesis nor substantial extracts from it may be printed or otherwise reproduced without the author's permission.

AVIS:

L'auteur a accordé une licence non exclusive permettant à la Bibliothèque et Archives Canada de reproduire, publier, archiver, sauvegarder, conserver, transmettre au public par télécommunication ou par l'Internet, prêter, distribuer et vendre des thèses partout dans le monde, à des fins commerciales ou autres, sur support microforme, papier, électronique et/ou autres formats.

L'auteur conserve la propriété du droit d'auteur et des droits moraux qui protègent cette thèse. Ni la thèse ni des extraits substantiels de celle-ci ne doivent être imprimés ou autrement reproduits sans son autorisation.

In compliance with the Canadian Privacy Act some supporting forms may have been removed from this thesis.

Conformément à la loi canadienne sur la protection de la vie privée, quelques formulaires secondaires ont été enlevés de cette thèse.

While these forms may be included in the document page count, their removal does not represent any loss of content from the thesis.

Bien que ces formulaires aient inclus dans la pagination, il n'y aura aucun contenu manquant.


Canada

Deuterium Nuclear Magnetic Resonance Spectroscopy and Molecular Dynamics Studies of Transmembrane Polypeptides

by

©David J. Goodyear

A thesis submitted to the School of Graduate
Studies in partial fulfilment of the requirements for the
degree of Doctor of Philosophy

Department of Physics and Physical Oceanography
Memorial University of Newfoundland
December 2003

St. John's Newfoundland Canada

To my friends and family...

Abstract

^2H NMR studies of synthetic polypeptides in bilayer membranes were performed. The results suggest that such transmembrane polypeptides undergo fast, axially symmetric reorientation about the bilayer normal and have a preferred average azimuthal orientation about the helix axis. Quadrupolar splittings and quadrupolar echo decay measurements indicate that the correlation time for reorientation is on the order of 10^{-7} s. At high temperatures the spectra are indicative of peptides that rotate mainly as monomers while broadening at lower temperatures is consistent with transient peptide-peptide interactions. The appearance of a broad, low amplitude feature in spectra at low concentrations seems to indicate that a certain fraction of peptides interact and rotate as short lived dimers.

Further ^2H NMR studies of two synthetic polypeptides with glycoporphin A (GPA) motifs suggest that these model peptides are tilted in bilayers and rapidly reorient about the bilayer normal with a correlation time on the order of 10^{-7} s. Observed spectra and echo decay measurements indicate that the orientation and dynamics of each peptide depend on GPA motif position. This suggests that the position of the interaction motif in the peptide sequence may play an important role in determining peptide orientation in bilayers.

To characterize helix motion and orientation, systems consisting of 64 molecules of 1-palmitoyl-2-oleoyl-sn-glycero-3-phosphocholine (POPC) and one α -helical polypeptide with the sequence acetyl-KK-(LA)₁₁-KK-amide were examined by molecular dynamics simulation. The systems were allowed to evolve for up to 10 ns at 1 atmosphere of pressure and a temperature of 55 °C. It is was found that the polypeptide orders lipid chains and thus increases bilayer thickness in accordance with previous simulations and experimental observations. Alanine methyl groups were found to be inequivalent which is consistent with ^2H NMR splittings observed from specifically labelled polypeptides in POPC bilayers. The simulation results suggest that the

polypeptide assumes a preferred orientation with respect to the bilayer normal and about the molecular long axis.

Acknowledgements

I will begin by thanking my parents. Through their constant love and support I have achieved great things. They have made enjoyable experiences even more enjoyable. They have accompanied me through bad times without asking questions. I hope some day that I will parent children the way they have.

I thank my brother for his love of life, wittiness and humour. No matter how bad a situation is, he always finds some reason to laugh. Being brothers and roommates have been interesting experiences...

I wish to acknowledge my fiancée, Janice Butt. Her glowing personality never fails to set things straight. She has given me a new way to look at the world.

I acknowledge Dr. M. R. Morrow for his support during this project. He has been a supervisor and a friend. He has guided me through this research program and has helped me with some of life's challenges.

Dr. C. Grant's contribution to this project is also acknowledged. I thank his research group for preparation of peptide samples and useful discussions about the experimental results. Finally, I thank the Theoretical and Computational Biophysics Group (University of Illinois at Urbana Champaign, Beckman Institute) for the molecular dynamics code (NAMD2) used during this work.

Contents

Abstract	i
Acknowledgements	iii
Contents	iv
List of Figures	vi
List of Tables	ix
1 Introduction	1
1.1 Studies of EGFR Transmembrane Segments	4
1.2 Studies of Model Peptides	6
1.3 The Present Study	9
2 NMR Theory	14
2.1 The Zeeman Interaction	14
2.2 The Hamiltonian in the presence of a RF Field	18
2.3 The Quadrupolar Interaction	20
2.4 ^2H NMR Line Shape: The Pake Doublet	25
2.5 The Quadrupolar Echo Pulse Sequence	31
2.6 Molecular Motion and Relaxation	36
3 Molecular Dynamics Theory	42
3.1 The Ensemble Average	43
3.2 The Classical Potential	45
3.3 The Equations of Motion	55

4	Experimental Setup and Details	58
4.1	Sample Preparation	58
4.2	² H NMR Spectrometer Setup and Experimental Details	61
4.3	² H NMR Spectroscopy	65
5	²H NMR Studies of Transmembrane Polypeptides: Polyalanine-leucine	67
5.1	Introduction	67
5.2	Polyalanine-leucine	70
5.3	Results	71
5.4	Discussion	81
5.5	Calculation of Deuteron Splittings Based on α -helical Geometry . . .	90
5.6	Summary	93
6	Molecular Dynamics Simulation of a Transmembrane Polypeptide	97
6.1	Introduction	97
6.2	Methods	98
6.2.1	Initial System Preparation	98
6.2.2	Polypeptide Construction	100
6.2.3	Lipid-Peptide System Construction and Preparation	102
6.3	Results and Discussion	103
6.3.1	Bilayer Equilibration and Dynamics	103
6.3.2	Protein Structure and Dynamics	110
6.3.3	Comparison with ² H NMR Experiments	118
6.4	Summary	133
7	²H NMR Studies of Transmembrane Polypeptides: Polyalanine-leucine with Interaction Motifs	137
7.1	Introduction	137
7.2	Polyalanine-leucine containing GPA interaction motifs	139
7.3	Results	140
7.4	Discussion	147
7.5	Summary	152
8	Conclusions	154
	Bibliography	157
	Appendix A. NMR Theory	168

List of Figures

1.1	A phospholipid molecule	2
1.2	Transmembrane polypeptides with tryptophan and lysine end residues.	8
2.1	Zeeman splitting of nuclear spin energy levels.	16
2.2	Probability distribution for a spherical distribution of C-D bond orientations.	27
2.3	Coordinate systems involved in the transformation of the quadrupolar Hamiltonian electric field gradient tensor from the principal axis system to the laboratory frame of reference.	28
2.4	The quadrupolar splitting and the Pake Doublet.	29
2.5	The quadrupolar echo sequence.	32
3.1	The dihedral angle.	47
3.2	The dihedral potential function $U_d(\phi_{ijkl})$	49
3.3	The Ewald Summation.	52
3.4	The van der Waals Potential.	54
4.1	Block diagram of the ^2H NMR spectrometer.	62
4.2	Block diagram of the quadrature detector.	64
5.1	Four amino acid residues and their respective sidechains.	69
5.2	^2H NMR spectra of alanine deuterated $\text{CH}_3\text{CO-KK-(LA)}_{11}\text{-KK-CO-NH}_2$ (LA22-1) dispersed in POPC bilayers at varying temperatures. The position of the deuterated methyl group is indicated in Table 5.1.	73

5.3	^2H NMR spectra correspond to alanine deuterated $\text{CH}_3\text{CO-KK-(LA)}_8\text{L-KK-CO-NH}_2$ (LA17-1) at varying temperatures. The position of the deuterated methyl group is indicated in Table 5.1.	74
5.4	^2H NMR spectra of alanine deuterated $\text{CH}_3\text{CO-KK-(LA)}_{11}\text{-KK-CO-NH}_2$ (LA22-1) at 60 °C and 30 °C in POPC bilayers. The position of the deuterated methyl group is indicated in Table 5.1.	75
5.5	^2H NMR spectra of alanine deuterated $\text{CH}_3\text{CO-KK-(LA)}_8\text{L-KK-CO-NH}_2$ (LA17-1) at 60 °C and 30 °C in POPC bilayers. The position of the deuterated methyl group is indicated in Table 5.1.	76
5.6	Quadrupolar echo decay times and calculated correlation times for short and long polypeptides at varying concentrations.	80
5.7	The angle $\beta_{ }$ between the alanine methyl group bond axis and the long axis of the polypeptide.	83
5.8	^2H NMR spectra correspond to $\text{CH}_3\text{CO-KK-(LA)}_{11}\text{-KK-CO-NH}_2$ at 60 °C and 30 °C in POPC bilayers and deuterated at 7 alanine methyl group positions.	85
5.9	An illustration of molecular rotations involved when calculating alanine quadrupolar splittings using the constructed molecular model.	92
6.1	Bilayer RMSD.	105
6.2	Area per lipid headgroup	107
6.3	Unsaturated chain deuterium order parameter profile for POPC.	108
6.4	Saturated chain deuterium order parameter profile for POPC.	109
6.5	Bilayer thickness.	111
6.6	Ramachandran plot of the ϕ and ψ dihedral angles for the polypeptide during the simulation were the peptide was initially aligned along the z axis.	113
6.7	Dihedral angles along the helix backbone of the polypeptide for the simulation were the peptide was initially aligned along the z axis.	114

6.8	Various angular orientations for the polypeptide calculated during the simulation where the peptide was initially oriented along the z axis.	119
6.9	Various angular orientations for the polypeptide calculated during the simulation where the peptide was initially tilted in the bilayer.	120
6.10	Peptide tilt and azimuthal orientation during the simulation with the peptide initially aligned along the z axis.	123
6.11	Peptide tilt and azimuthal orientation during simulation with the peptide initially tilted in the bilayer.	124
6.12	Peptide tilt and instantaneous quadrupolar splitting during the simulation with the peptide initially aligned along the z axis	130
6.13	Z position of the lysine C_α carbon atoms and the average z position of the lipid phosphorus atoms during the simulation trajectory.	132
6.14	Z position of the lysine nitrogen atoms and the average z position of the lipid phosphorus atoms during the simulation trajectory.	134
7.1	^2H NMR spectra of GPA22-1 peptides at a concentration of 4 mol% for varying temperatures.	142
7.2	^2H NMR spectra of GPA22-2 peptides at a concentration 4 mol % for varying temperatures.	143
7.3	Quadrupolar echo decay curves for GPA22-1 (A) or GPA22-2 (B) peptides at a concentration of 4 mol % in POPC bilayers.	145
7.4	Quadrupolar echo decay times (T_2^{qe}) for GPA22-1 (A) or GPA22-2 (B) peptides at a concentration of 4 mol % in POPC.	146
7.5	Correlation times for GPA22-1 (\diamond) and GPA22-2 (\circ) peptides at a concentration of 4 mol % in POPC bilayers	148
A.1	Net magnetization in the NMR experiment.	169
A.2	The effect of an RF pulse on equilibrium magnetization	173
A.3	Zeeman splitting of nuclear spin energy levels	176

List of Tables

1.1	Peptide sequence and deuteron label positions in LA peptides used in this study	11
4.1	Peptide sequence and deuteron label positions in LA peptides used in this study.	60
5.1	Peptide sequence and deuteron label positions in LA peptides used in this study.	72
5.2	Splittings calculated for 7 alanine positions within the transmembrane domain at a tilt of 12° and a rotation angle of 4°.	94
6.1	Absolute value of the calculated ^2H NMR splittings for the polypeptide in the simulation with the peptide initially aligned along the z axis. . .	128
6.2	Absolute value of the calculated ^2H NMR splittings for the polypeptide in the simulation with the peptide initially tilted in the bilayer. . . .	129
6.3	Z positions of the lysine side-chain nitrogens with respect to the lysine C_α carbon positions.	135
7.1	Samples used in this ^2H NMR investigation.	141
A.1	Unitary transformation of the operator \hat{O}_n about the operator \hat{O}_1 . .	193
A.2	Unitary transformation of the operator \hat{O}_n about the operator \hat{O}_2 . .	194
A.3	Transformation of the operator \hat{O}_n under the influence of first order quadrupolar coupling.	196

Chapter 1

Introduction

Biological membranes play a central role in the structure and function of cells in all living species. Although the compositions of biological membranes vary, the main constituents are lipids and proteins [1]. Phospholipids are found in most biological membranes and form a fluid bilayer matrix [1, 2]. These lipids are typically composed of non-polar hydrocarbon chains and a polar headgroup. Figure 1.1 illustrates a common phospholipid known as 1-palmitoyl-2-oleoyl-sn-glycero-3-phosphocholine (POPC). Biological membranes typically have proteins embedded in the lipid bilayer. Some of these proteins have hydrophobic regions that span the fluid region of the lipid bilayer (integral membrane proteins) while other proteins may be only partially buried in the bilayer membrane (peripheral membrane proteins). Properties of transmembrane segments of integral membrane proteins may be relevant to biological processes. Such processes might involve interactions between transmembrane segments of integral membrane proteins or interactions of transmembrane protein segments with the surrounding lipid environment. Peptides that are peripheral in nature and interact mainly with the membrane surface may also be biologically relevant.

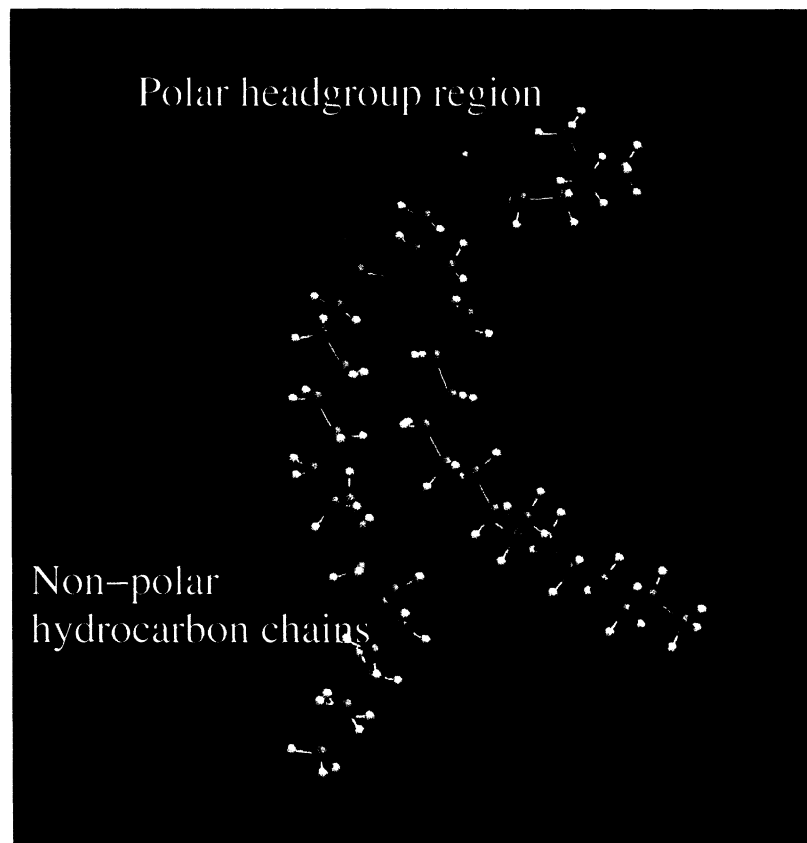


Figure 1.1: A phospholipid molecule composed of a polar headgroup region and non-polar hydrocarbon chains. Carbon is represented by light blue, nitrogen is dark blue, red is oxygen, yellow is phosphorous and hydrogens are represented by white.

To investigate the behavior of integral membrane proteins one strategy is to consider the protein transmembrane segment or simpler peptides modeled on such segments. The interactions between transmembrane protein segments and bilayers raise interesting questions about the behaviour of self assembled structures containing components with different properties. For instance, the lipids are flexible since they contain many internal degrees of freedom while helical transmembrane protein segments composed of amino acid residues are typically more rigid, but may have very different surfaces depending on the types of amino acids in the transmembrane polypeptide sequence.

Other interesting questions arise with regard to physiological processes which involve transmembrane proteins [3, 4]. For example, the interactions between transmembrane segments of the epidermal growth factor receptor (EGFR) protein are likely important to cellular growth. This project investigates the dynamics of model transmembrane peptides. The study presented here was initially motivated by earlier studies of peptides based on EGFR transmembrane segment[5–9]. In some of those studies, transmembrane segments of EGFR were labelled on peptide alanine residues and observed using wide-line NMR. The results provided evidence for rapid rotation about the bilayer normal with essentially no rotation about the helix axis. In addition, there was some evidence for transient peptide-peptide interactions between EGFR transmembrane segments.

In this work, we have looked at simple uniform peptides composed of leucine-alanine subunits (LA) which have hydrophobic sidechains. The peptide ends are terminated with charged lysines. One question which arises is whether the dynamics

of EGFR transmembrane segments (*i.e.* no rotation about helix axis and limited association) were specific to the EGFR peptide sequence or are more general properties of transmembrane peptides. In addition, the interactions between transmembrane segments of EGFR are characterized by special amino acid sequences or motifs, and another interesting issue was whether the tendency of uniform peptides to self associate is dependent on the presence of such interaction motifs. To address these issues we have used ^2H NMR and molecular dynamics (MD) to study alanine labeled peptides. We have also studied two LA-based peptides containing a glycoporphin A (GPA) motif sequence in different orientations to address issues of whether peptide association is sensitive to the positioning of specific interaction motifs.

1.1 Studies of EGFR Transmembrane Segments

In this project we are investigating the dynamics of model transmembrane peptides. The work presented here was initially motivated by issues arising from earlier ^2H NMR studies of specific transmembrane segments relevant to EGFR [5–9]. In some of those studies deuterium probe nuclei were located on methyl side chains of alanine residues. ^2H NMR studies of the transmembrane domain of deuterated alanine methyl groups on EGFRs [6] showed that these segments undergo rapid axially symmetric rotation on a time scale shorter than the NMR experiment (*i.e.* $< 10^{-5}$ s). In those experiments the transmembrane domains behaved mainly as monomers but spectral broadening with decreasing temperature suggested some side-to-side association of transmembrane segments [6].

The methyl group is attached to the helix backbone by a carbon-carbon bond. Because the quadrupolar interaction is averaged by fast rotation about its symmetry

axis, the quadrupolar splitting, $\Delta\omega$, for deuterated alanine methyl groups attached to a polypeptide undergoing fast axially symmetric reorientation reflects the angle between polypeptide rotation axis and the methyl group carbon-carbon bond. Molecular modeling and molecular dynamics simulations [7, 10] of peptide helices, show that the angle between the methyl axis and the helix axis is about 56° . As shown in Chapter 5, rotation about the helix axis for a methyl group having this orientation should give a very small quadrupolar splitting. The quadrupolar splittings obtained by Grant and co-workers [5, 7, 9] for the EGFR transmembrane domain were larger than could be explained by rapid axially symmetric rotation about the helix axis. However, the results could be explained in terms of a helix undergoing rapid reorientation about the bilayer normal. It was suggested by Grant and co-workers [7] that interference with rotation about the helix axis might arise from the energetic cost of exposing hydrophobic amino acid side chains to the hydrophilic membrane-water interface.

The observations reported in this work place constraints on helix orientation and dynamics which may be important to understanding self-association of EGFR. The way in which the charged end residues interact with the membrane surface may lock the helix in a specific orientation which would prevent the exposure of hydrophobic amino acid side-chains to the hydrophilic membrane-water interface. The resulting orientation of the protein segments might then affect the extent of association through side-to-side interactions. If motions about the helix axis are constrained then small fluctuations about the equilibrium orientation may be significant to regulating intermolecular contact, which has implications for association of proteins like EGFR. These observations may also be important to other biologically relevant processes that involve protein association.

1.2 Studies of Model Peptides

The peptides used in the first part of this study are LA units terminated by charged lysine residues. The interactions between bilayer lipids and $(LA)_n$ peptides terminated by polar groups have been the subject of many previous studies [10–14]. Peptides with LA subunits that are terminated with charged tryptophan residues, or WALPs have been studied extensively by Killian and coworkers [11, 15–18]. The current work is based on LA peptides terminated with lysines (K). This class of peptides (KALPs) has been investigated by several research groups including Killian and coworkers [11, 15–18] and McElhaney and coworkers [19–21]. Figure 1.2 illustrates both WALP and KALP peptides with terminal tryptophan and lysine residues respectively. Differential scanning calorimetric and FTIR spectroscopic studies of KK- $(LA)_{12}$ -KK provide evidence that these peptides are predominantly α -helical when dispersed in diacylphosphatidylcholines in both the gel and liquid crystalline phases, thus providing a model to investigate properties of transmembrane segments of natural proteins [19]. Killian and co-workers have investigated interactions between model peptides and bilayers and the effects of peptide length on peptide orientation and bilayer morphology using several experimental techniques including circular dichroism, NMR and FTIR [11, 15–18]. Studies concerning the structure of peptides in bilayer environments and the effect of peptides on bilayer order using ESR and FTIR have been carried out by McElhaney and coworkers [19–21].

The structures of these model peptides allow us to address interesting questions about interactions of peptides with the membrane environment and the effects of these interactions on peptide structural, dynamical, and aggregation characteristics. These

characteristics may have implications for biological processes that involve transmembrane segments of integral membrane proteins. The central regions of these peptides (composed of LA subunits) are highly hydrophobic while the lysine and tryptophan terminal residues have charged or polar side chains. The charged ends of these peptides can interact electrostatically with the polar lipid headgroups at the membrane-water interface [16, 22] while the hydrophobic regions may preferentially interact with the bilayer interior. The combination of a hydrophobic central region and charged lysines or tryptophans near the polar bilayer surface constrains peptide orientation and dynamics.

Hydrophobic mismatch can be an issue when the hydrophobic length of transmembrane protein segments differs from the hydrophobic thickness of lipid bilayers. Effects of hydrophobic mismatch for artificial polypeptides in bilayers have been studied using NMR, CD and FTIR spectroscopy [15, 18, 23] and it is found that mismatch leads to changes in bilayer ordering and affects peptide orientation. Changes in the bilayer phase behaviour for varying degrees of peptide hydrophobic mismatch have been reported by Killian and co-workers [15, 18]. ^{31}P NMR spectra of phosphatidylcholines obtained in those studies confirm that WALP and KALP peptides may deform bilayers and promote the formation of nonlamellar phases when hydrophobic mismatch is present [18]. The deformation of bilayers due to hydrophobic mismatch may be important to the lateral organization of membrane proteins and might contribute to understanding of processes like protein segregation [18]. Stress induced in bilayers through hydrophobic mismatch may also influence peptide conformation which may be a factor in controlling the function of transmembrane proteins.

The mismatch between hydrophobic lengths of protein transmembrane segments

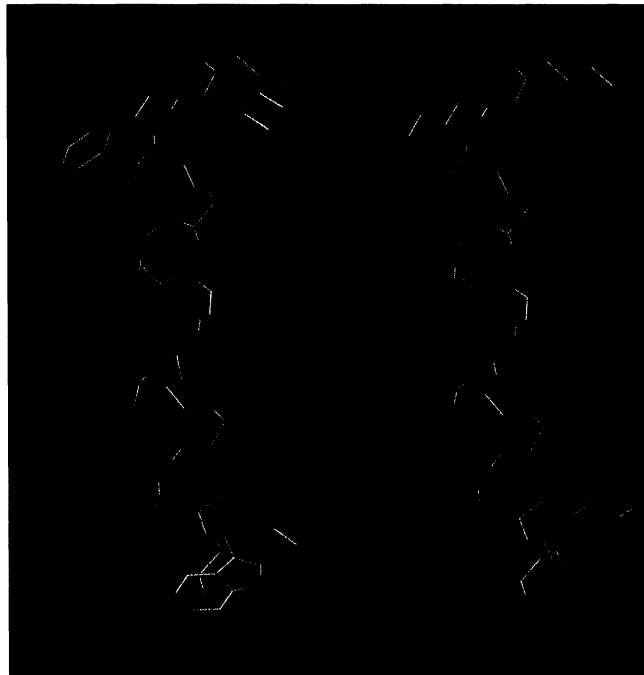


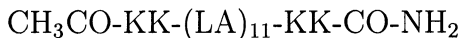
Figure 1.2: Transmembrane polypeptides with tryptophan (left) and lysine (right) end residues. Carbon is represented by light blue, nitrogen is dark blue and red is oxygen. Hydrophobic sidechains and hydrogens have been omitted for clarity.

and the hydrophobic bilayer interior can influence both bilayer phase behaviour and orientation of transmembrane protein segments. The interactions of peptide terminal residues with the polar membrane surface may also play a key role in determining the orientation and dynamics of transmembrane proteins. Killian and von Heigne [22] suggest that interactions between proteins and the membrane-water interface depend strongly on the specific properties of the amino acid side chains. ^2H NMR and ESR studies carried out by de Planque *et al.* [12] on α -helical WALP and KALP peptides in phosphatidylcholine membranes, indicate that some peptides are tilted in the bilayer and the degree of association with the membrane is dependent on the flanking end residues. This supports the notion that the interactions between peptides and lipid bilayers are strongly dependent on specific side chain properties [12]. Additional studies carried out by de Planque *et al.* [16] using NMR, ESR, CD and molecular modeling of WALP peptides support an orientational model where tryptophan tends to maintain a well defined position around the level in the bilayer where the lipid carbonyl groups reside. The same study suggests that the charged lysine ends interact preferentially with lipid phosphate groups at the membrane-water interface [16], thus confirming the specificity of interactions between bilayers and peptide terminal side chains. More generally, the interactions of transmembrane peptides with the bilayer interior and at the membrane interfacial region will strongly depend on amino acid side chain properties such as hydrophobicity, charge, and polarity [22].

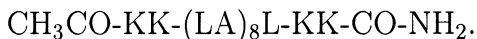
1.3 The Present Study

In order to further clarify some of the physical characteristics of transmembrane polypeptides in bilayers, and gain some insight into the fundamental behaviour of

transmembrane proteins in biological membranes, we have investigated selected artificial polypeptides. The peptides used in these studies are of the KALP variety and the amino acid sequences are given by



and



Several experiments have been carried out for each peptide with deuterons substituted on various alanine methyl groups within the transmembrane region. The specific positions of deuteration for these peptides are illustrated in Table 1.1. These deuterated alanines have been used to probe the orientation of KALP peptides in bilayers and obtain the correlation times for reorientation.

Previous FTIR spectroscopic studies of $\text{KK-(LA)}_{12}\text{-KK}$ confirm that peptides with 12 LA subunits are α -helical when dispersed in PC bilayers and therefore these peptides are also expected to be α -helical. Several parameters may be used to characterize α -helical geometry of these transmembrane segments. For an ideal α -helix there are 3.6 amino acid residues per turn of the helix coil and each turn corresponds to an increase in length of 1.5 Å [24]. Since the repeat LA subunits have hydrophobic side chains then the longer peptide used in this study has 22 hydrophobic residues while the shorter peptide has 17 hydrophobic residues. This corresponds to a hydrophobic length of approximately 33 Å and 25.5 Å for each peptide respectively. The differing lengths for these peptides will enable us to investigate the effect of hydrophobic mismatch on peptide orientation in bilayers.

These polypeptides are more uniform than natural protein transmembrane segments like EGFR which often have special amino acid motifs that are thought to

Peptide Sample	Peptide Sequence
LA17-1	CH ₃ CO-KK-LALALALALaLALALAL-KK-CO-NH ₂
LA22-1	CH ₃ CO-KK-LALALALALALaLALALALALA-KK-CO-NH ₂
LA22-2	CH ₃ CO-KK-LALALALALALaLaLALALALA-KK-CO-NH ₂
LA22-7	CH ₃ CO-KK-LALALaLaLaLaLaLaLaLaLALA-KK-CO-NH ₂

Table 1.1: Peptide sequence and deuterium label positions in LA peptides used in this study. The number appended to the LA peptide sample prefix indicates the number of hydrophobic residues in the amino acid sequence. The lowercase A's represent the position of alanine deuterated methyl groups. The number following the "-" indicates the number of deuterated alanines.

promote protein association. This particular sequence of amino acids may remove some potentially specific interactions between amino acid side chains of transmembrane segments. An interesting issue which can then be addressed is the tendency of uniform peptides to self associate in the absence of specific side chain interactions. Since ^2H NMR spectra are sensitive to molecular orientation and motions these experiments can provide information about the peptide dynamical properties, the interactions between polypeptides and interactions with the membrane environment.

Using molecular dynamics simulations, the behaviour of the longer model polypeptide was also investigated on a timescale which is much shorter than the NMR timescale of 10^{-5}s . MD simulations and molecular modeling allow us to validate some of the assumptions made during the spectral analysis such as the assumption of a uniform α -helix. The combination of both experimental and simulation techniques helps us to better characterize polypeptide behaviour and gain some insight into the fundamental physical behaviour of membrane spanning proteins like EGFR.

Peptide association may be important to the function of membrane proteins with single and multiple transmembrane helices. The interactions leading to peptide association are often characterized by special motifs. For example, the transmembrane region of glycophorin A, a single span transmembrane protein, has a special motif which is thought to lead to the formation of dimers [25]. This glycophorin A (GPA) motif provides a simple model for understanding peptide-peptide interactions between single-span transmembrane proteins. To address issues of whether peptide association is sensitive to positioning of specific interaction motifs we have also considered KALP peptides with GPA motifs in different orientations. This is important since it can

provide us with insight into the specificity of interactions between transmembrane protein segments. The sequences are



and



where lowercase “a” indicates the position of the deuterated methyl group along the sequence and the bolded characters, **L_{ixx}GV_{xx}GV_{xx}T**, form a motif found in natural glycoporphin A [25]. Both peptides have the same hydrophobic length based on α -helical geometry and are deuterated at the same position along the amino acid sequence. However, the peptides differ in the motif position, which has been shifted by one amino acid residue. This shift in position along the helix corresponds to a 100° difference in angular orientation of the motif about the helix axis. Since the lengths of both peptides are the same then we expect that the design of these peptides minimize any potentially different interactions of the peptide terminal residues with the bilayer surface. Therefore, we may be able to characterize possible specific interactions between helices with motifs in differing positions and observe the effect of motif position on peptide dynamics. This will provide insight into possible specific interactions between transmembrane segments of natural proteins such as EGFR.

Chapter 2

NMR Theory

The study presented in this thesis involves ^2H NMR observations of deuterated polypeptides. In order to understand how ^2H NMR is used to probe the dynamical and orientational characteristics of polypeptides in bilayers, it is useful to begin with some theory of the NMR phenomenon using a quantum description. A description of the Zeeman interaction is presented first in order to provide an overview of the quantum nature of the deuterium nucleus and an overview of the NMR experiment. For a deuteron, the quadrupolar interaction perturbs the Zeeman interaction and this perturbation is orientation dependent. Through the quadrupolar interaction we can obtain both dynamical and orientational information and therefore place constraints on peptide conformation, orientation, and dynamics in bilayer membranes.

2.1 The Zeeman Interaction

The NMR phenomenon is a direct result of the quantum spin angular momentum of the nucleus. The spin angular momentum of an atomic nucleus results in a magnetic dipole moment and the magnetic dipole operator for a single spin can be written as

[26]

$$\begin{aligned}\hat{\boldsymbol{\mu}} &= \gamma\hbar\hat{\boldsymbol{I}} \\ &= \gamma\hbar(\hat{I}_x\mathbf{i} + \hat{I}_y\mathbf{j} + \hat{I}_z\mathbf{k})\end{aligned}\tag{2.1.1}$$

where γ is the gyromagnetic ratio of the nucleus, \hbar is Planck's constant divided by 2π , and $\hat{\boldsymbol{I}}$ is the nuclear spin operator. For an isolated dipole moment, interacting with a static magnetic field oriented along the z direction, the Hamiltonian is given by [27, 28]

$$\begin{aligned}\hat{H}_Z &= -\hat{\boldsymbol{\mu}} \cdot \vec{H}_0 \\ &= -\gamma\hbar\vec{H}_0\hat{I}_z\end{aligned}\tag{2.1.2}$$

which is analogous to the potential energy of a classical dipole in a magnetic field (see Appendix A). Identifying $|m\rangle$ as the eigenvectors of the operator \hat{I}_z , the Schrödinger equation yields

$$-\gamma\hbar H_0\hat{I}_z|m\rangle = -\gamma\hbar H_0 m|m\rangle\tag{2.1.3}$$

where $m = -I, -I + 1 \dots I$, and I is the nuclear spin quantum number [27].

The deuteron has a nuclear spin of 1 so the eigenvalues of \hat{I}_z are $m = \pm 1, 0$ and the energy eigenvalues are given by

$$E_1 = -\gamma\hbar H_0, \quad E_0 = 0, \quad E_{-1} = \gamma\hbar H_0.\tag{2.1.4}$$

The application of a static magnetic field splits the degenerate spin energy level into three energy eigenstates referred to as Zeeman levels (See Figure 2.1). The energy of each Zeeman level is dependent on the projection of nuclear spin along the H_0 field direction and therefore describes the alignment of the nuclear spin in

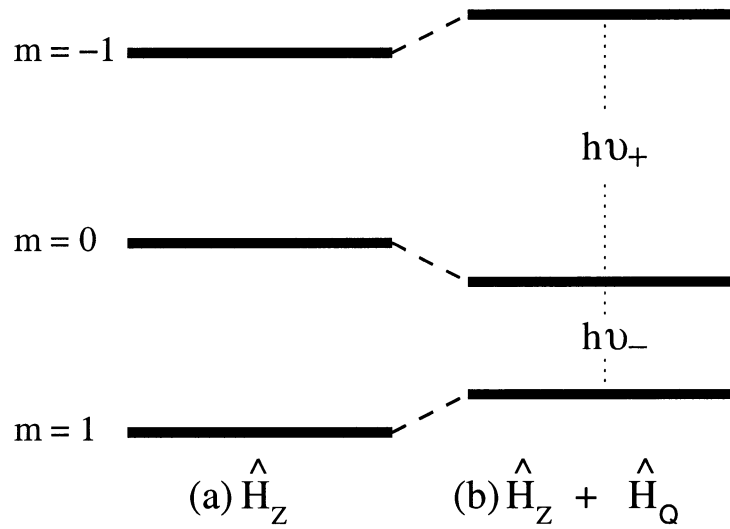


Figure 2.1: Zeeman splitting of nuclear spin energy levels. (a) When placed in a static magnetic field the degenerate $I = 1$ state splits into three states that describe the orientation of the magnetic dipole in the magnetic field. (b) For a deuteron the Zeeman energy levels are shifted by the quadrupolar interaction.

the magnetic field. The energy difference between the Zeeman levels is $\hbar\omega_0$ where $\omega_0 = \gamma H_0$ is referred to as the Larmor frequency. The energy difference between the spin states is typically small so transitions may be induced between the energy levels using short duration pulses of radio frequency (RF) radiation [29]. Application of RF radiation is achieved by surrounding the sample containing the nuclear spins by a conductive coil (perpendicular to the field) and applying an alternating current at the appropriate frequency. Inducing transitions between the nuclear spin states corresponds to manipulation of the z component of the nuclear spin.

The relative populations of the Zeeman levels are governed by Boltzmann statistics. In terms of the partition function Z for the system, the population of energy level E_m is

$$p(E_m) = \frac{e^{-\frac{E_m}{k_b T}}}{Z}. \quad (2.1.5)$$

In the high temperature approximation we can expand the exponential using a Taylor series which gives

$$p(E_{-1}) = \frac{1}{3} \left(1 + \frac{\hbar\omega_0}{k_b T} \right), \quad p(E_0) = \frac{1}{3}, \quad p(E_1) = \frac{1}{3} \left(1 - \frac{\hbar\omega_0}{k_b T} \right) \quad (2.1.6)$$

for the populations for the Zeeman levels [30]. Since the energy difference (*i.e.* $\hbar\omega_0$) between levels is small compared to $k_b T$ this leads to an excess of approximately one in 10^8 spins occupying the lower energy level where the nuclear dipoles are aligned with the magnetic field direction.

From the expectation values of the z component of the dipole operator, $\langle \hat{\mu}_z \rangle = \gamma \hbar m$, the statistical average of the z component of the nuclear dipole is [31]

$$\bar{\mu}_z = \sum_m \gamma \hbar m p(E_m) \quad (2.1.7)$$

and the summation is over the possible spin orientations. Upon substitution of $p(E_m)$ into the above equation we have,

$$\bar{\mu}_z = \frac{2\gamma^2\hbar^2}{3k_B T} H_0. \quad (2.1.8)$$

Since the magnetization is proportional to the average dipole moment then [27]

$$\begin{aligned} M_z &= N\bar{\mu}_z \\ &= \frac{2N\gamma^2\hbar^2}{3k_B T} H_0 \end{aligned} \quad (2.1.9)$$

where N is the number of spins in the system. Due to the difference in populations of the spin states, the system has non-zero equilibrium magnetization which is analogous to the classical description for a system of magnetic dipoles.

2.2 The Hamiltonian in the presence of a RF Field

The Hamiltonian of a nuclear dipole in the laboratory frame in the presence of a static magnetic field and an applied RF pulse is given by

$$\begin{aligned} \hat{H} &= \hat{H}_Z + \hat{H}_{RF} \\ &= -\hat{\boldsymbol{\mu}} \cdot (\vec{H}_0 + \vec{H}_{RF}). \end{aligned} \quad (2.2.1)$$

The oscillatory RF field can be decomposed into two rotating components one of which, \vec{H}_{RF} , is given by

$$\vec{H}_{RF} = H_1(\cos(\Omega t)\mathbf{i} + \sin(\Omega t)\mathbf{j}). \quad (2.2.2)$$

As discussed in Appendix A, the other rotating component can be ignored. Substitution of expression 2.2.2 into the Equation 2.2.1 yields [28]

$$\hat{H} = -\gamma\hbar H_0 \hat{I}_z - \gamma\hbar H_1 \hat{I}_x \cos(\Omega t) - \gamma\hbar H_1 \hat{I}_y \sin(\Omega t) \quad (2.2.3)$$

which is a logical extension of the static field Hamiltonian presented in Equation 2.1.2. Factoring $-\gamma\hbar H_1$ from the 2nd and 3rd terms of Eq. 2.2.3 yields

$$\hat{I}_x \cos(\Omega t) + \hat{I}_y \sin(\Omega t).$$

This describes the rotation of an operator, in the plane subtended by \hat{I}_x and \hat{I}_y , about the z axis and can be written in terms of a unitary transformation [32]. Using the unitary transformation [28, 33]

$$e^{-i\Omega t \hat{I}_z} \hat{I}_x e^{i\Omega t \hat{I}_z} = \hat{I}_x \cos(\Omega t) + \hat{I}_y \sin(\Omega t),$$

Equation 2.2.3 can be written as

$$\hat{H} = -\gamma\hbar H_0 \hat{I}_z - \gamma\hbar H_1 e^{-i\Omega t \hat{I}_z} \hat{I}_x e^{i\Omega t \hat{I}_z}. \quad (2.2.4)$$

The wavefunction Ψ describing the nuclear state in the laboratory frame can also be described in terms of a unitary transformation of the wavefunction in a frame of reference (x', y', z') rotating with an angular velocity $\vec{\Omega} = \Omega \mathbf{k}'$ where the z' axis coincides with the z axis of the laboratory frame. Rotation of the coordinate frame associated with the scalar wavefunction leads to

$$|\Psi\rangle = e^{-i\Omega t \hat{I}_z} |\Psi'\rangle \quad (2.2.5)$$

where Ψ' is the wavefunction in the rotating frame of reference [27]. Substituting Equations 2.2.4 and 2.2.5 into the Schrödinger equation leads to the Hamiltonian in the rotating frame of reference. In a frame of reference rotating with the frequency of the applied RF (*i.e.* Ω) the Hamiltonian is [27, 28]

$$\hat{H} = -\gamma\hbar \left(\frac{\Omega}{\gamma} + H_0 \right) \hat{I}_z - \gamma\hbar H_1 \hat{I}_x \quad (2.2.6)$$

which consists of two parts. The first term is the Zeeman Hamiltonian in the rotating frame (*i.e.* \hat{H}'_Z) and the second term is the RF Hamiltonian in the rotating frame (*i.e.* \hat{H}'_{RF}). The resonance condition is satisfied when $\Omega = -\gamma H_0$ in which case Equation 2.2.6 reduces to

$$\hat{H} = -\gamma\hbar H_1 \hat{I}_x. \quad (2.2.7)$$

In a frame of reference rotating at the Larmor frequency the nuclear spin interacts solely with the applied RF field. Since \hat{I}_x can be written as a linear combination of raising and lowering operators then this Hamiltonian changes the z component of nuclear spin. It should be noted that application of a pulse along the y direction of the rotating frame gives the Hamiltonian $-\gamma\hbar H_1 \hat{I}_y$.

Classically, a system of dipoles exhibits a net magnetization as derived in Equation 2.1.9, resulting from the difference in the populations of Zeeman levels. The results presented in this section can be used to show the precession of net magnetization at the Larmor frequency and the rotation of the net magnetization into the plane perpendicular to the applied H_0 magnetic field. A pulse of RF energy which rotates the net magnetization into a plane perpendicular to the applied field (H_0) is referred to as a $\frac{\pi}{2}$ pulse. The classical description of NMR, including the effect of a RF field on net magnetization, is further developed in Appendix A.

2.3 The Quadrupolar Interaction

When a nuclear dipole is placed in a magnetic field its degenerate energy level splits. In addition to a magnetic dipole, the deuteron has a small electric quadrupole moment arising from the asymmetrical distribution of charge in the nucleus. This leads to an additional term in the Hamiltonian due to the interaction of the quadrupole moment

with an electric field gradient (EFG) at the nuclear center [28, 30]. This field gradient may be due to the distribution of electronic charge surrounding the nucleus. The total Hamiltonian can be written as [34]

$$\hat{H} = \hat{H}_Z + \hat{H}_Q \quad (2.3.1)$$

and results in a shift of the Zeeman energy levels as illustrated in Figure 2.1. The perturbation is exaggerated in this illustration. The quadrupole interaction is typically several orders of magnitude smaller than the Zeeman interaction energy and can be treated as a small perturbation to the Zeeman energy levels. The perturbation can be calculated using classical electrostatics by employing the energy of a charge distribution in a electric potential [28, 35]:

$$E = \int \rho(\vec{r})V(\vec{r})d\vec{r}. \quad (2.3.2)$$

Expanding $V(\vec{r})$ in a Taylor series about the position of the nucleus and integrating over nuclear coordinates leads to the energy of a charge distribution in an electric field [30]. The third term in the energy expansion is calculated to be

$$E_Q = \frac{1}{2} \sum_{i,j} V_{ij}Q_{ij}, \quad (2.3.3)$$

where V_{ij} and Q_{ij} are elements of the EFG tensor and the quadrupole moment tensor of the deuterium nucleus respectively. It is important to note that the EFG tensor is a symmetric traceless second rank tensor so that there exists some coordinate transformation which will diagonalize the tensor [36]. The coordinate system which yields the diagonalized EFG is referred to as the principal axis system of the tensor. By diagonalizing this tensor we can more easily calculate the energy shifts of the quadrupolar interaction using the Wigner-Ekharth theorem [28, 30]. Transformation

of coordinates through Euler angles θ and ϕ from the principal axis system of the EFG tensor to the laboratory frame of reference yields the quadrupole Hamiltonian, \hat{H}_Q , given by [30]

$$\hat{H}_Q = \frac{e^2 q Q}{8} \left(\frac{3 \cos^2 \theta - 1}{2} + \frac{1}{2} \eta \sin^2 \theta \cos 2\phi \right) (3\hat{I}_z^2 - 2). \quad (2.3.4)$$

In Equation 2.3.4, eq is the principal value of the electric field gradient tensor, eQ is the quadrupole moment of the deuteron [36] and η is referred to as the asymmetry parameter. This is the secular part (commutes with \hat{I}_z) of the quadrupolar Hamiltonian and thus is the only part which contributes to first order shift in the Zeeman energy levels.

Since the basis vectors $|m\rangle$ are eigenvectors of the operator \hat{I}_z , the energies corresponding to the Hamiltonian given in Equation 2.3.4 are

$$E_Q^m = \frac{e^2 q Q}{8} \left(\frac{3 \cos^2 \theta - 1}{2} + \frac{1}{2} \eta \sin^2 \theta \cos 2\phi \right) (3m^2 - 2). \quad (2.3.5)$$

For the $m = \pm 1$ eigenstates the quadrupole interaction shifts the Zeeman levels upwards by an amount

$$\Delta = \frac{e^2 q Q}{8} \left(\frac{3 \cos^2 \theta - 1}{2} + \frac{1}{2} \eta \sin^2 \theta \cos 2\alpha \right) \quad (2.3.6)$$

and for $m = 0$ the Zeeman level is shifted downward by 2Δ . If the quadrupole interaction is neglected the spectrum will be a single line at the resonance frequency ω_0 . With the quadrupole interaction included the transitions $\Delta m = \pm 1$, are split by

$$\Delta\omega(\theta, \phi) = \frac{3 e^2 q Q}{2 \hbar} \left(\frac{3 \cos^2 \theta - 1}{2} + \frac{1}{2} \eta \sin^2 \theta \cos 2\phi \right). \quad (2.3.7)$$

The spectrum of a ^2H nucleus attached to a carbon atom is thus a doublet centered about the resonance frequency ω_0 and the splitting, $\Delta\omega$, is referred to as the

quadrupole splitting. Since $\eta \approx 0.007$ [26] for carbon-deuterium bonds then the expression is essentially independent of ϕ and can be written as,

$$\Delta\omega(\theta) = \frac{3}{2} \frac{e^2 q Q}{\hbar} \left(\frac{3 \cos^2 \theta - 1}{2} \right). \quad (2.3.8)$$

In the presence of molecular motion the quadrupolar splitting is modulated by the variations in molecular orientation. In order to derive an expression for the resultant averaged splitting in this case we consider transformations through several frames of reference. We start by considering the laboratory coordinate frame and another coordinate frame which is fixed to the bilayer. These coordinate systems provide a reference orientation for the axis about which the molecule reorients. We also consider the principal axis system of the EFG which defines a system fixed to a C-D bond that can move about the frame fixed to the bilayer. For the studies presented here, the frame fixed to the bilayer has an axis which is normal to the lipid bilayer. If the deuterated molecule reorients about bilayer normal, then transformation through the Euler angles α , β , and γ from the principal axis system of the EFG to the bilayer fixed frame and then through the angles α' , θ , and γ' to the laboratory frame results in the splitting [30]

$$\Delta\omega(\theta, \beta, \alpha) = \frac{3}{2} \frac{e^2 q Q}{\hbar} \left(\frac{3 \cos^2 \theta - 1}{2} \right) \left(\frac{3 \cos^2 \beta - 1}{2} + \frac{1}{2} \eta \sin^2 \beta \cos 2\alpha \right). \quad (2.3.9)$$

If the correlation time for reorientation of the C-D bond within the frame attached to the bilayer is much shorter than the minimum time required for such motion to contribute to motional narrowing (*i.e.* $\tau_c \ll 1/\sqrt{\Delta M_2}$), the splitting reflects the average quadrupole interaction and the splitting becomes

$$\Delta\omega(\theta, \beta, \alpha) = \frac{3}{4} \frac{e^2 q Q}{\hbar} \left(\frac{3 \cos^2 \theta - 1}{2} \right) \langle (3 \cos^2 \beta - 1) + \eta \sin^2 \beta \cos 2\alpha \rangle \quad (2.3.10)$$

where $\langle \dots \rangle$ denotes an average over the all possible orientations of α and β modulated by the molecular motion. In other words, molecular motion effectively averages the quadrupolar interaction and leads to a reduced splitting.

For axially symmetric C-D bonds $\eta \approx 0$ [36]. However, if the molecular motions have two-fold symmetry or lower symmetry, the spectrum can still exhibit an effective asymmetry parameter even though the EFG is axially symmetric [37]. Axially symmetric motion about a single molecular axis is considered to be fast compared to the experiment timescale when the molecule samples all orientations about the rotation axis with a correlation time that satisfies the short correlation time limit (*i.e.* $\tau_c \ll 1/\sqrt{\Delta M_2}$). When motion is rapid and axially symmetric the term containing η disappears and the quadrupolar splitting becomes

$$\Delta\omega(\theta, \beta) = \frac{3}{2} \frac{e^2 q Q}{\hbar} \left(\frac{3 \cos^2 \theta - 1}{2} \right) \left\langle \frac{3 \cos^2 \beta - 1}{2} \right\rangle \quad (2.3.11)$$

where β defines the angle between the C-D bond vector and the bilayer normal. The averaged quantity (denoted by $\langle \dots \rangle$) is often referred to as the deuterium orientational order parameter, S_{CD} , and is an average over the reorientation. This parameter can be determined by measuring the width of the ^2H NMR spectrum and provides information concerning molecular ordering and the average orientation of the C-D bond in the molecular environment.

When considering deuterated methyl groups attached to polypeptides one must also account for rapid rotation about the methyl group symmetry axis. The transformation of coordinates from the principal axis coordinate system of the EFG tensor for the CD bond to the laboratory frame leads to an additional term in the splitting,

$\langle \frac{3 \cos^2 \theta_{methyl} - 1}{2} \rangle \approx \frac{1}{3}$ since $\theta_{methyl} \approx 109.5$, and the splitting can then be written as

$$\Delta\omega(\theta, \beta) = \frac{1}{2} \frac{e^2 q Q}{\hbar} \left(\frac{3 \cos^2 \theta - 1}{2} \right) \left\langle \frac{3 \cos^2 \beta - 1}{2} \right\rangle \quad (2.3.12)$$

where, in this case for rapidly rotating methyl groups, it is convenient to define β as the angle between the methyl group rotation axis and the molecular rotation axis (ie bilayer normal). For the polypeptides investigated here, the deuterated alanine methyl groups are rigidly attached to the helix backbone. The quadrupolar splitting is therefore a direct probe of average peptide orientation in bilayers.

The quadrupolar splitting derived above applies to a single bilayer fixed coordinate system with the bilayer normal oriented at θ with respect to the applied magnetic field. For a distribution of such bilayer normal vectors, as is the case for spherical lipid vesicles, the spectrum will be a continuous distribution of doublets reflecting the distribution of bilayer normal orientations. The case for a spherical distribution of deuterated molecules is most important to this research and is described in the next section.

2.4 ^2H NMR Line Shape: The Pake Doublet

In the previous section the ^2H NMR spectrum was described in terms of transitions between deuteron energy levels. For an aligned system where the deuterated molecules reorient about axes having the same orientation θ with respect to the applied magnetic field the spectrum will be two lines split by $\Delta\omega(\theta, \beta)$. If there is a distribution of bilayer orientations within the system then the lineshape reflects the geometrical distribution of molecules in the system.

Various geometrical distributions of molecules have been reviewed and can provide information concerning phase behaviour of the lipid system [36]. In this research we

deal with deuterated peptides dispersed in multilamellar vesicles in the fluid L_α phase and are thus concerned with a spherical distribution of molecular orientations.

We assume a uniform distribution of C-D bond orientations over the surface of a sphere. The number of orientations between θ and $\theta + d\theta$ with respect to the applied field H_0 can be written as [36]

$$\begin{aligned} dN &= \frac{N}{4\pi} 2\pi \sin \theta d\theta \\ &= \frac{N}{2} \sin \theta d\theta. \end{aligned} \quad (2.4.1)$$

In other words, the probability density of finding an orientation at angle θ is equal to

$$p(\theta) = \frac{1}{2} \sin \theta. \quad (2.4.2)$$

Following the analysis of Seelig [36], two transition frequencies can be calculated from the energy eigenvalues of the Zeeman and quadrupolar Hamiltonians and used to define a reduced frequency,

$$\zeta_{\pm} = \pm \frac{3 \cos^2 \theta - 1}{2}. \quad (2.4.3)$$

Using Equation 2.4.3 and the definition for the probability for C-D bond orientations given in Equation 2.4.2 the probability density $p(\zeta)$ for each of the reduced transition frequencies can be written as

$$p(\zeta_{\pm}) = \frac{1}{\sqrt{\pm 2\zeta_{\pm} + 1}}. \quad (2.4.4)$$

The spectrum will contain both reduced resonances so that [36]

$$p(\zeta) = p(\zeta_+) + p(\zeta_-). \quad (2.4.5)$$

This is illustrated in Figure 2.2.

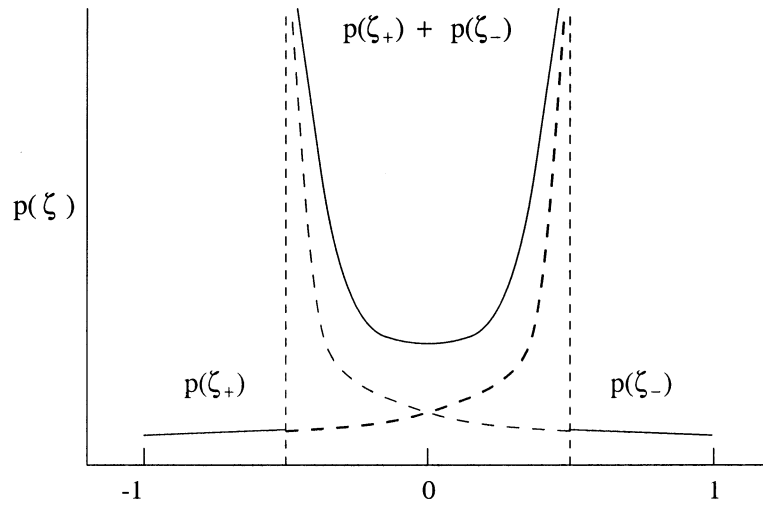


Figure 2.2: Probability distribution for a spherical distribution of C-D bond orientations.. This spectrum is typically referred to as a Pake doublet.

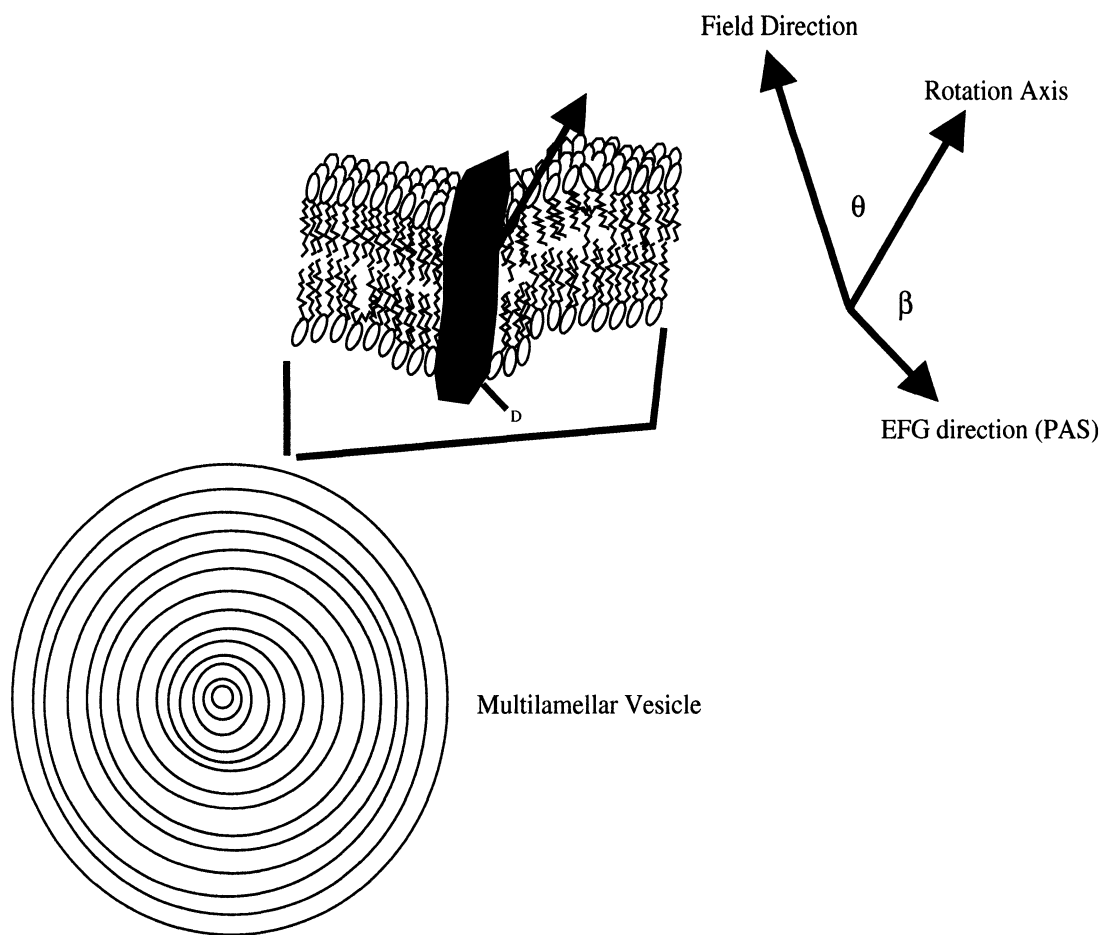
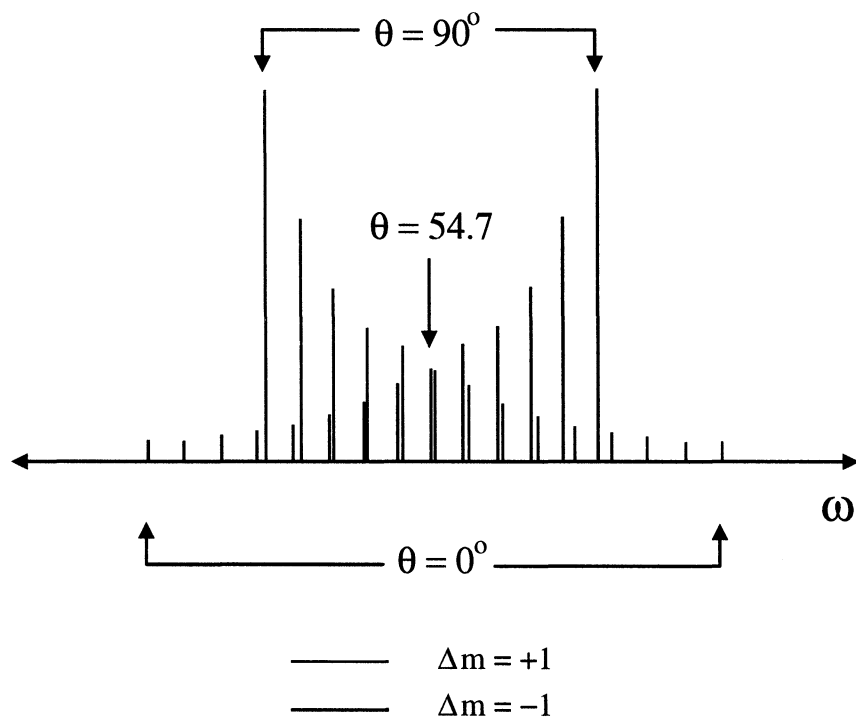
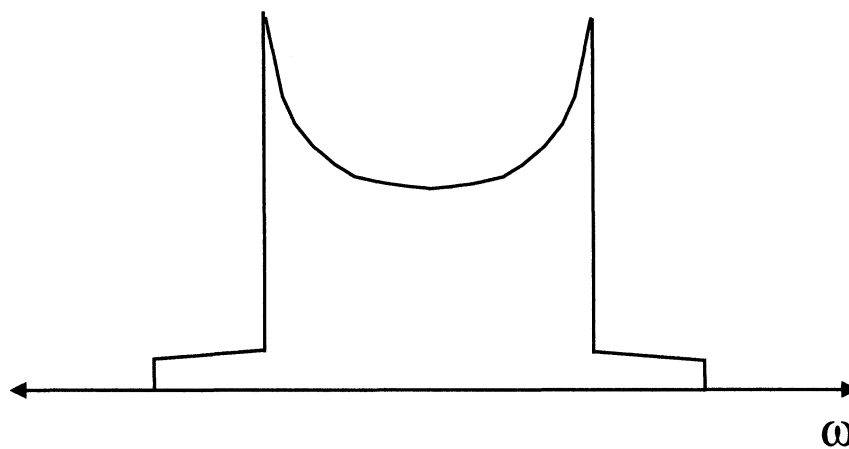


Figure 2.3: Coordinate systems involved in the transformation of the quadrupolar Hamiltonian electric field gradient tensor from the principal axis system to the laboratory frame of reference. This transformation accounts for reorientation of the C-D bond about the molecular symmetry axis oriented at angle θ with respect to the applied magnetic field.



(a) Individual quadrupolar splittings ($\Delta m = \pm 1$) for deuterated molecules dispersed throughout multilamellar lipid vesicles as illustrated in Figure 2.3. The intensity of the absorption lines are largest for $\theta = 90^\circ$.



(b) The "Pake Doublet" resulting from all possible orientations of θ .

Figure 2.4: The quadrupolar splitting and the Pake Doublet.

This lineshape can be related to the doublets arising from particular orientations as follows. We consider a uniform distribution of deuterated molecules dispersed throughout multilamellar lipid vesicles and undergoing rapid rotation about the symmetry axis (oriented at θ with respect to H_0) as illustrated in Figure 2.3. The absorption of RF radiation leading to transitions between the perturbed Zeeman levels depends on θ through the orientation dependence of the quadrupolar interaction. Each orientation θ gives two absorption lines corresponding to the two transitions ($\Delta m = \pm 1$) for the deuteron spin as illustrated in Figure 2.4(a). Each red line ($\Delta m = +1$) has a corresponding black line ($\Delta m = -1$) of equal intensity which gives the quadrupolar splitting for a given molecular orientation. The distribution of intensity is simply due to the fact that for a uniform spherical distribution there will be more deuterated molecules situated about the equator (*i.e.* $\theta = 90^\circ$) of these vesicles than in the polar regions (*i.e.* $\theta = 0^\circ$).

Reorientation of the C-D bond with respect to the molecular rotational axis due to fluctuations which modulate the angle β in Equation 2.3.11, lead to averaging of the quadrupolar splitting through the order parameter S_{CD} . This is similar for each deuterated molecule so that the width of the whole spectrum is scaled by S_{CD} . This orientational order parameter reflects the mobility and orientation of deuterated molecules in the lipid membrane environment. In this study, the quadrupolar splitting (proportional to S_{CD}) is measured from the 90° edges of the Pake spectrum and reflects the average orientation of the deuterated methyl group bond axis with respect to the bilayer normal. In this way, the spectral shape can be directly related to peptide orientation in bilayers.

2.5 The Quadrupolar Echo Pulse Sequence

Excitation of the spin system through RF radiation is typically followed by detection of the NMR signal. In liquids these signals have lifetimes on the order 1 ms - 1 s, due to effective averaging of the orientation dependent nuclear tensor interactions, resulting from rapid molecular tumbling. However, for deuterium in partially ordered systems where motion is restricted the observed signals decay quickly within the first few microseconds after RF excitation. During the first few microseconds after the pulse the receiver is saturated with RF power. This “deadtime” thus becomes an issue when considering short lived free induction decays [30].

In order to circumvent the problem of signal acquisition and receiver “deadtime” the quadrupolar echo technique was introduced [30]. This pulse sequence is illustrated in Figure 2.5. The sequence consists of two 90° RF pulses separated by some time interval, τ , and shifted in phase by 90° .

Evolution of a spin-1 system under the influence of interactions with RF fields and the quadrupolar interaction is best described in terms of a density matrix operator which contains information concerning the energy states of the spin system. Detailed quantum statistical descriptions of NMR, the density matrix and the quadrupolar echo sequence are presented in Appendix A. For a deuteron (spin-1) the density matrix can be represented by a vector in a space that is spanned by 9 orthogonal operators. Following the notation of Davis [30] we choose

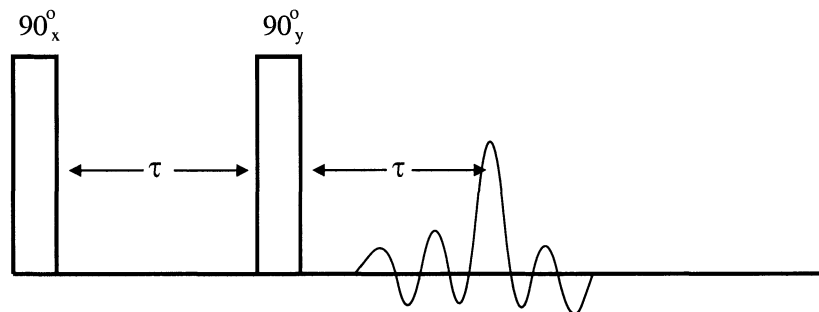


Figure 2.5: The quadrupolar echo sequence. The first 90° pulse excites the spin system. During τ the magnetization dephases due to a distribution of dipole precession frequencies. The second pulse refocuses the dephasing magnetization into an echo at time τ after the second pulse. Molecular motion leads to irreversible dephasing of the magnetization and therefore leads to decay of the measured echo. In this way the quadrupolar echo sequence provides information about the molecular motion.

$$\begin{aligned}
\hat{O}_1 &= \frac{1}{\sqrt{2}}\hat{I}_x & \hat{O}_2 &= \frac{1}{\sqrt{2}}\hat{I}_y & \hat{O}_3 &= \frac{1}{\sqrt{2}}\hat{I}_z \\
\hat{O}_4 &= \frac{1}{\sqrt{6}}(3\hat{I}_z^2 - I^2) & \hat{O}_5 &= \frac{1}{\sqrt{2}}(\hat{I}_x\hat{I}_z + \hat{I}_z\hat{I}_x) & \hat{O}_6 &= \frac{1}{\sqrt{2}}(\hat{I}_y\hat{I}_z + \hat{I}_z\hat{I}_y) \\
\hat{O}_7 &= \frac{1}{\sqrt{2}}(\hat{I}_x^2 + \hat{I}_y^2) & \hat{O}_8 &= \frac{1}{\sqrt{2}}(\hat{I}_x\hat{I}_y + \hat{I}_y\hat{I}_x) & \hat{O}_9 &= \frac{1}{\sqrt{3}}\hat{1}
\end{aligned}$$

as the basis for our orthogonal set. It is important to note that all elements of the orthogonal set obey $Tr(\hat{O}_m\hat{O}_n) = \delta_{mn}$ [30] and are, in fact, orthonormal operators.

In order to define a starting configuration for the spin-1 system, we consider the equilibrium density operator. This is obtained by considering the Boltzmann distribution for populations of the Zeeman states. Neglecting the perturbation to the Zeeman levels by the quadrupolar interaction the equilibrium density operator is [28]

$$\hat{\rho} = \frac{e^{-\frac{\hat{H}_Z}{k_B T}}}{Z}. \quad (2.5.0)$$

Using the definition of the Zeeman Hamiltonian, given by Equation 2.1.2, to simplify expression 2.5.0 and then expanding the exponential we can write

$$\begin{aligned}
\hat{\rho} &= \frac{e^{\frac{\gamma\hbar H_0 \hat{I}_z}{k_B T}}}{Z} \\
&= \frac{1}{Z} \left(1 + \frac{\gamma\hbar H_0 \hat{I}_z}{k_B T} \right)
\end{aligned} \quad (2.5.1)$$

Using a Taylor series, each exponential term in Z can be expanded at high temperatures and the density matrix in this new basis is written as

$$\hat{\rho} = \frac{1}{3} \left(\frac{1}{\sqrt{3}} + \frac{\sqrt{2}\gamma\hbar H_0}{k_B T} \hat{O}_3 \right).$$

Since the observable quantities are defined by the trace of the density matrix with any of the nine orthonormal operators, and $Tr(\frac{1}{\sqrt{3}}\hat{1}\hat{O}_n) = 0$, then the density operator

can be rewritten in the reduced form [33]

$$\begin{aligned}\hat{\rho} &= \frac{\gamma\hbar H_0}{3k_B T} \hat{I}_z \\ &= \frac{\sqrt{2}\gamma\hbar H_0}{3k_B T} \hat{O}_3.\end{aligned}\tag{2.5.2}$$

Using the properties of the density operator it is possible to calculate the quantum statistical average of any system observable. As shown in Appendix A the trace of a system operator with the density operator gives the quantum statistical average. The total z-magnetization operator can be written as [31]

$$\begin{aligned}\widehat{M}_z &= N\hat{\mu}_z \\ &= \gamma\hbar N\hat{I}_z\end{aligned}\tag{2.5.3}$$

$$= \sqrt{2}\gamma\hbar N\hat{O}_3\tag{2.5.4}$$

where N is the number of spins in the ensemble. Consequently, the expectation value of z-magnetization is

$$\begin{aligned}\langle\widehat{M}_z\rangle &= Tr(\hat{\rho}\widehat{M}_z) \\ &= \frac{1}{3} \left(2\frac{\gamma^2\hbar^2 N}{k_b T} H_0 Tr(\hat{O}_3^2) \right)\end{aligned}\tag{2.5.5}$$

and since $Tr(2\hat{O}_3^2) = I(I+1)(2I+1)/3$ [32], the equilibrium magnetization for a system of spin-1 particles is given by

$$\langle\widehat{M}_z\rangle = \frac{2\gamma^2\hbar^2 N}{3k_b T} H_0.\tag{2.5.6}$$

In order to track the time evolution of the equilibrium density matrix under the influence of RF pulses we can expand $\hat{\rho}$ in terms of the orthonormal set by writing [30],

$$\hat{\rho} = \sum_{n=1}^8 c_n(t) \hat{O}_n\tag{2.5.7}$$

where we have taken into account that writing the ninth operator (*i.e.* $\hat{1}$) has no affect on the final state of the density matrix. That is, the trace of any observable with this operator is zero [33]. We can think of $c_n(t)$ as the components of a vector $\hat{\rho}$ which change in time as it rotates in this 9-D operator space under the influence of specific Hamiltonians. Substituting this expansion of $\hat{\rho}$ into the Liouville equation and taking the trace with an operator \hat{O}_p yields,

$$\frac{dc_p(t)}{dt} = -\frac{i}{\hbar} \sum_n c_n(t) Tr(\hat{O}_n[\hat{H}, \hat{O}_p]) \quad (2.5.8)$$

as described by Davis [30]. The solutions to these differential equations have been presented by Davis [30] and Schmidt *et al.* [38] for various RF pulse Hamiltonians and quadrupolar coupling. The effect of various RF pulse Hamiltonians and the quadrupolar interaction Hamiltonian on the set of operators described above are illustrated in Tables A.1 through A.3 (see Appendix A) and are presented in a notation similar to that of Schmidt *et al.* [38].

By solving coupled differential equations associated with the evolution of the spin-1 density operator during the quadrupolar echo sequence, Davis [30] has shown that $\hat{\rho}$ after the second pulse is

$$\hat{\rho} = \frac{\sqrt{2}\hbar\omega_0}{3k_B T} (\cos(\omega_Q[t - \tau])\hat{O}_2 + \sin(\omega_Q[t - \tau])\hat{O}_5). \quad (2.5.9)$$

At $t = \tau$ after the second pulse, the density operator is

$$\hat{\rho} = \frac{\sqrt{2}\hbar\omega_0}{3k_B T} \hat{O}_2 \quad (2.5.10)$$

and taking the trace with the operator $M_y = \sqrt{2}N\gamma\hbar\hat{O}_2$ yields

$$\begin{aligned}
 Tr(\rho\hat{M}_y) &= Tr\left(\frac{\sqrt{2}\hbar\omega_0}{3k_B T}\hat{O}_2\sqrt{2}N\gamma\hbar\hat{O}_2\right) \\
 &= \frac{2N\gamma^2\hbar^2}{3k_B T}H_0Tr(\hat{O}_2^2) \\
 &= \frac{2N\gamma^2\hbar^2}{3k_B T}H_0
 \end{aligned} \tag{2.5.11}$$

which is precisely the magnitude of the equilibrium magnetization calculated previously. So at $t = \tau$ after the second pulse the ‘‘coherence’’ created by the first pulse is refocused along the y axis. Expectation values of the \hat{O}_1 and \hat{O}_2 operators correspond to components of magnetization. A more detailed treatment of the quadrupolar echo using the density matrix is presented in Appendix A.

Application of the quadrupole echo in this study serves two purposes. First, taking the Fourier transform of the quadrupolar echo signal following the echo maximum gives a frequency domain spectrum of the alanine deuterated polypeptides. The spectrum provides information concerning peptide structure, orientation and molecular motions. Secondly, varying the time (τ) between the pulses provides information about decay of the quadrupole echo due to motions that modulate the quadrupole interaction. This is described in more detail in Section 2.6.

2.6 Molecular Motion and Relaxation

The application of RF pulses to the spin system depletes the net z-magnetization and creates a coherence in the density matrix. As seen in the previous section, this coherence evolves under the influence of the quadrupolar interaction and can be manipulated using RF pulses to obtain an echo. For a time-independent Hamiltonian, the coherence would rotate indefinitely in the 9D operator space. However, due to

relaxation processes described in this section, the coherence eventually decays and equilibrium magnetization is restored in the spin system.

Relaxation mechanisms result from random field fluctuations generated by dipolar, chemical shielding, quadrupolar, and a multitude of other nuclear interactions [27, 39]. Since chemical shielding has a small effect compared to the quadrupolar interaction for the deuteron it is not considered here. There may be dipolar interactions between deuterons on alanine methyl groups and protons along the peptide backbone or protons attached to the amino acid sidechains. However, when compared to the proton-proton dipolar interaction, the proton-deuteron dipolar interaction is about six times weaker while the deuteron-deuteron dipolar interaction is about thirty-six times weaker [33]. Additionally, the dipolar coupling constant for proton-deuteron dipole interactions is on the order of several kHz [33]. This is significantly small when compared with the quadrupolar coupling constant between carbon and the attached deuteron which is approximately 167 kHz. Therefore we are mainly concerned with the effects of the quadrupolar interaction since dipole-dipole interactions have little influence on deuterons attached to polypeptides.

All relaxation mechanisms are influenced by molecular motion and fluctuating electromagnetic fields experienced by nuclear spins. Molecular motions lead to rapid, random fluctuations in the magnetic and electric fields that nuclei experience. These fluctuations may induce transitions, between the Zeeman levels, which then restore the net magnetization to the equilibrium direction. To effectively contribute to relaxation, the local fields must be time-dependent such that the spectrum of the fluctuating fields contains non-zero components at frequencies equal to those of the nuclear magnetic dipole transition [39]. The stimulation of transitions through interactions

leads to relaxation of the excited spin system. The relaxation time associated with the regrowth of equilibrium magnetization (T_1) after an RF excitation is only considered when choosing some quadrupolar echo pulse sequence timings.

Relaxation times govern the decay of coherence in the density matrix and the return to equilibrium. For a spin-1 particle each observable in the density matrix has an associated decay parameter [40]. In this work we measure the relaxation time associated with quadrupole echo decay (T_2^{qe}). These relaxation time provides information concerning molecular motion and the chemical/physical environment of the nuclear spins. Molecular motions that modulate the quadrupolar interaction lead to irreversible dephasing of the nuclear spins and therefore affect the quadrupolar echo amplitude. The extent of echo decay due to this dephasing therefore provides information concerning motions with correlation times that change the orientation of the electric field gradient principal axis system and therefore modulate the quadrupole interaction. These correlation times reflect decay of the correlation function associated with the quadrupolar interaction (*i.e.* $P_2(\cos \theta)$). Davis [41] observed that $T_1 \gg T_2^{qe}$ for ^2H NMR nuclei in the acyl chains of lipid molecules in bilayers. This implies that there exist motions with correlation times τ_1 which are fast (on the order of the Larmor frequency) that contribute to T_1 relaxation while slower motions with correlation times τ_2 contribute to T_2^{qe} relaxation. Thus relaxation time measurements provide a way to investigate molecular motions with different correlation times. The hierarchy of correlation times which contribute to relaxation is best represented by

$$\tau_1 \leq \omega_0^{-1} \ll \tau_2 \ll \tau_M$$

where $\tau_M = (\Delta M_2)^{-\frac{1}{2}}$ represents the minimum correlation time required for motions to lead to motional narrowing of the NMR spectrum and ΔM_2 is the apparent second

moment of the spectrum.

In the fast motion regime (ie $\Delta M_2 \tau_c^2 \ll 1$) the echo decay time, T_2^{qe} , is related to the correlation time for the motion, τ_c , and the apparent second spectral moment by [34, 42]

$$\frac{1}{T_2^{qe}} = \Delta M_2 \tau_c. \quad (2.6.1)$$

and is expected to give rise to exponential relaxation [34]. Through variation of the pulse separation τ in the quadrupolar echo sequence one finds a characteristic transverse relaxation time, T_2^{qe} , governing the decay of the quadrupolar echo. The resulting echo amplitude at 2τ after the initial pulse obeys,

$$A(2\tau) = A(0) e^{-\frac{2\tau}{T_2^{qe}}}, \quad (2.6.2)$$

where T_2^{qe} is sensitive to the reorientational processes which occur over the experiment timescale. For a spin system where deuterons have different echo decay times, for instance due to different orientations or molecular motions, the relaxation behaviour can be represented by a sum of exponentials. This expression can be written as

$$A(2\tau) = \sum_i A_i(0) e^{-\frac{2\tau}{T_{2i}^{qe}}} \quad (2.6.3)$$

where $A_i(0)$ is proportional to the population of deuterons with relaxation time T_{2i}^{qe} .

For small τ each exponential can be expanded and rearranged to give

$$\begin{aligned} A(2\tau) &= \sum_i A_i(0) \left(1 - 2\tau \frac{1}{\sum_i A_i(0)} \left(\sum_i \frac{A_i(0)}{T_{2i}^{qe}} \right) \right) \\ &= \sum_i A_i(0) \left(1 - 2\tau \left\langle \frac{1}{T_2^{qe}} \right\rangle \right) \end{aligned} \quad (2.6.4)$$

where $\left\langle \frac{1}{T_2^{qe}} \right\rangle$ is the averaged relaxation rate resulting from deuterons which have different relaxation times due to different orientations and/or are affected by different motions.

For the special case where quadrupole echo decay is dominated by rotation of a rigid molecule about a fixed axis, we follow the analysis of Pauls *et al.* [42]. The model assumes rotation of a deuterated polypeptide about a single rotational axis and does not take into account fluctuations in deuterated methyl group orientation due to peptide conformational changes or fluctuations of the bilayer normal direction. It is reasonable to assume that peptide conformational fluctuations are fast on the experiment timescale and contribute mainly to T_1 relaxation. In this model we assume that the observed relaxation behaviour is therefore mainly due to the variations in the quadrupolar interaction resulting from reorientation of peptides about the bilayer normal. Taking into account rapid rotation about the methyl group axis, the quadrupolar splitting for static polypeptides is

$$\Delta\omega(\theta) = \frac{e^2qQ}{2\hbar} \left(\frac{3 \cos^2 \theta - 1}{2} \right). \quad (2.6.5)$$

Rotation about the bilayer normal modulates the quadrupolar interaction and reduces the splitting to

$$\Delta\omega(\theta, \beta) = \frac{e^2qQ}{2\hbar} \left(\frac{3 \cos^2 \theta - 1}{2} \right) \left\langle \frac{3 \cos^2 \beta - 1}{2} \right\rangle. \quad (2.6.6)$$

This also leads to random accumulation of phase during the quadrupolar echo experiment and therefore leads to ineffective refocusing of the quadrupolar echo [42]. In this case the echo decay is exponential as predicted by the theory of motional narrowing for the fast motion regime [34] and the measured T_2^{qe} is due to the powder average over all possible orientations and can be interpreted in terms of the apparent second moment of the spectrum. The change in the apparent second moment can be written as [42]

$$\Delta M_2 = \langle \omega(\theta)^2 \rangle - \langle \omega(\beta, \theta)^2 \rangle \quad (2.6.7)$$

where $\langle \dots \rangle$ represents an average over all possible orientations. Upon taking the powder average it can be shown that [42],

$$\Delta M_2 = \frac{1}{5} \left(\frac{e^2 q Q}{4\hbar} \right)^2 \left(1 - \left\langle \frac{3 \cos^2 \beta - 1}{2} \right\rangle^2 \right) \quad (2.6.8)$$

for systems where the asymmetry parameter is negligible.

The quadrupolar splitting given by Equation 2.3.11 is clearly dependent on $P_2(\cos \beta)$ so it can be shown that

$$\Delta M_2 = \frac{1}{5} \left(\omega_Q^{methyl} \right)^2 \left[1 - \left(\frac{\Delta\omega(\theta = 90^\circ, \beta)}{\omega_Q^{methyl}} \right)^2 \right]. \quad (2.6.9)$$

This is a modified version of the equation presented by Pauls *et al.* [42] for deuterons attached to polypeptides. Since we are investigating methyl group deuterated polypeptides, this equation accounts for rapid rotation about the methyl symmetry axis through the effective quadrupolar coupling constant $\omega_Q^{methyl} = \frac{e^2 Q q}{4\hbar}$ for deuterons attached to alanine methyl groups. Since the apparent second moment is dependent on the experimental splitting $\Delta\omega(\theta = 90^\circ, \beta)$ for the prominent 90° edges of the spectrum, this theory provides a quantitative way to estimate the correlation time of motion leading to narrowing of the NMR spectrum by using Equation 2.6.1. Since the observed echo decays presented in this study approximate exponential behaviour, we assume that the main contribution to echo decay is from variations in the quadrupolar interaction resulting from reorientation of the peptide about the bilayer normal.

Chapter 3

Molecular Dynamics Theory

Molecular dynamics (MD) is a technique used to compute the properties of an atomic many body system using classical mechanics [43]. The first MD simulations for a real material were reported by Vineyard who simulated radiation damage in crystalline copper [44]. Later, Rahman reported the first simulation of liquid argon [45] and since then MD simulations have become a common practice to test theoretical results. Today, increasing availability of fast computing resources have made it possible to simulate more complicated biological systems composed of lipids and proteins. The results from these computer experiments are often useful for comparison with experimental results.

In this thesis ^2H NMR experiments are used to probe polypeptide dynamics in a lipid environment. As a complement to the NMR studies, MD simulations were used to investigate structural and dynamical properties of polypeptides on a timescale which is much shorter than the characteristic NMR timescale. The NMR results provide us with a picture of the behaviour of polypeptides in model membranes and MD tests the assumptions made during the NMR analysis.

The MD code used for the simulation study presented here was NAMD2 [46]. The

code was chosen based on several qualities. First, the code employs the CHARMM forcefield which is discussed in more detail in Section 3.2. This force field has been used extensively in MD studies of a wide variety of biological systems including lipids and proteins as is studied here in this thesis [17, 47, 48]. The results of previous studies which employ the CHARMM force field agree well with experimental studies on similar biological systems. Secondly, the code is scalable which means that computationally intensive MD calculations can be distributed over many processors to decrease the total simulation time. Finally, the methods employed in the code are of the same caliber as many commercial MD packages yet the code is open source. Based on these items it seems that NAMD2 is an excellent choice for simulating a lipid-peptide system.

3.1 The Ensemble Average

Molecular dynamics involves defining a classical interaction potential between atoms in order to approximate the quantum energy surface for the system. The forces on atoms can be calculated from the gradient of this potential and used in a set of dynamical equations to propagate the evolution of the system in time. In the classical limit, the thermal average of a measurable quantity A is expressed as [43]

$$\langle A \rangle_{ensemble} = \frac{\int d\vec{p}^N d\vec{r}^N e^{-\beta\{\sum_i \frac{p_i^2}{2m_i} + U(\vec{r}^N)\}} A(\vec{p}^N, \vec{r}^N)}{\int d\vec{p}^N d\vec{r}^N e^{\beta\{\sum_i \frac{p_i^2}{2m_i} + U(\vec{r}^N)\}}} \quad (3.1.1)$$

$$= \int d\vec{p}^N d\vec{r}^N A(\vec{p}^N, \vec{r}^N) \rho(\vec{p}^N, \vec{r}^N) \quad (3.1.2)$$

where \vec{r} denotes the positions of the particles (*i.e.* $\vec{r}^N = \{\vec{r}_1, \vec{r}_2, \vec{r}_3 \dots, \vec{r}_N\}$), \vec{p} the momenta (*i.e.* $\vec{p}^N = \{\vec{p}_1, \vec{p}_2, \vec{p}_3, \dots, \vec{p}_N\}$), $U(\vec{r}^N)$ is the potential between interacting particles, and the integration is over all of phase space. This is often referred to as

an ensemble average [43].

The atomic positions and momenta change with time according to the interactions with neighbouring atoms under the influence of the potential $U(\vec{r}^N)$. The principle of measurement in an MD simulation is based on the ergodic assumption which essentially states that the ensemble average is equivalent to a measurement averaged over the course of the system's natural evolution [49]. Assuming that the ergodic principle applies, we may run the simulation for a sufficiently long duration and average specific quantities over time [31]. In this case, the time average is equivalent to the ensemble average [43, 49, 50] which is explicitly stated as [31]

$$\langle A \rangle_{time} \implies \langle A \rangle_{ensemble} = \lim_{T \rightarrow \infty} \frac{1}{T} \int_0^T A(\vec{p}^N(t), \vec{r}^N(t)) dt. \quad (3.1.3)$$

We see that the framework of MD computer simulations is based on statistical mechanics and the ergodic assumption relating the time average of a quantity to an ensemble average.

If we wish to obtain information about any of the lipid or peptide properties in the system simulated here, then an ensemble average of the quantity of interest must be carried out. In order to carry out a calculation one must have a time line of the MD system evolution. The MD trajectory contains all information concerning types of atoms present and their respective positions with a prescribed time step between time frames in the simulation. Calculations of both lipid and peptide properties are carried out in several steps. To begin, the physical property to be “measured” from the trajectory is calculated for the first frame of the simulation. Successive measurements are then extracted from the time frames of the simulation after which the average of all measurements is calculated. The results of the simulation can then be compared with experimental measurements. In this study we compare simulations

of a polypeptide in a bilayer with ^2H NMR observations from a similar lipid-peptide system.

In order to further develop this framework for MD simulation we explore the classical potential in the next section. It is from the classical potential that the quantum energy surface is approximated and used to calculate the intermolecular and intramolecular forces from which follows the time evolution of the system.

3.2 The Classical Potential

An accurate description of the MD system composed of many atoms requires that intermolecular and intramolecular forces be correctly modeled. In the simulations reported here an all-atom potential referred to as the CHARMM potential is used [51]. The CHARMM potential [51, 52],

$$\begin{aligned}
 U(\vec{r}^N) = & \sum U_b(r_{ij}) + \sum U_a(\theta_{ijk}) + \sum U_d(\phi_{ijkl}) \\
 & + \sum U_e(R_{ij}) + \sum U_{vdW}(R_{ij}) + U_{UB} + U_{inp}, \tag{3.2.1}
 \end{aligned}$$

is a sum of bonded and non-bonded potentials that describe a variety of interactions between atoms. A short description of each term follows.

The first term in the potential, $U_b(r_{ij})$, describes the interaction between two atoms due to molecular bonds. Through a Taylor expansion about the equilibrium separation for the atoms one may approximate this potential to second order by a harmonic spring potential [43]

$$U_b(r_{ij}) \approx \frac{\ddot{U}_b(r_0)}{2}(r_{ij} - r_0)^2 \tag{3.2.2}$$

$$= \frac{k_{ij}}{2}(r_{ij} - r_0)^2 \tag{3.2.3}$$

where r_{ij} is the distance between two bonded atoms and r_0 is their equilibrium separation. The constant $\ddot{U}_b(r_0) = k_{ij}$ is called the force constant. This is representative of the stiffness of the bond and is specific to the types of bonded atoms. Bending of the bond angles between three consecutively bonded atoms is also represented by a harmonic potential [43, 49]. Vibrations of atoms about the equilibrium bond lengths occur on a timescale of 10^{-15} s. These bond vibrations have little effect on the physical properties we wish to measure in the lipid-peptide simulation presented here so the bond lengths are constrained at a fixed length. The time step between integration of Newton's equations can therefore be increased in order to decrease simulation time. In these simulations time steps of 1 fs and 2 fs are used. The time step is chosen based on a conserved quantity which is constant in the NPT ensemble. This has been described by Frenkel [43].

If we consider four consecutively bonded atoms, the dihedral energy, $U_d(\phi_{ijkl})$, describes the potential between atoms separated by 3 bonds [43, 49, 53]. The second bond provides a rotational degree of freedom through which the dihedral angle ϕ_{ijkl} varies. This is probably best illustrated through a simple picture. Figure 3.1 illustrates four consecutive methylene groups along the acyl chain of a lipid molecule. As the dihedral angle around the central bond changes, the proximity of the first and last methylene groups changes. Due to approximate tetrahedral geometry for each methylene group one could imagine that as the end groups are rotated about the central bond, the potential energy between them will change. However it should be periodic and there should be certain configurations for which the potential is maximized and others for which the potential is minimized. The potential energy is

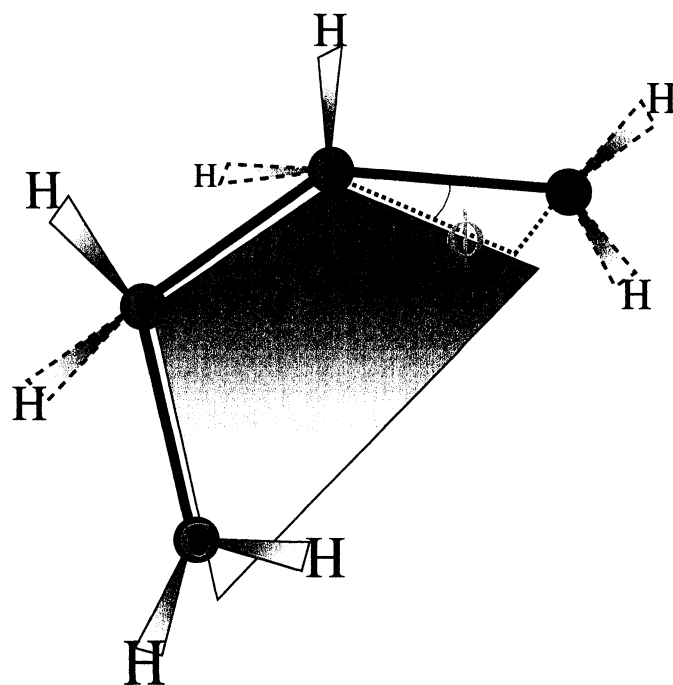


Figure 3.1: The dihedral angle for methylene groups separated by 3 bonds. Solid triangles represent bonds between carbon and hydrogen which point out of the page. Dotted triangles represent bonds between carbon and hydrogen which point into the page. The dihedral angle ϕ is the angle between one carbon-carbon bond and the plane formed by 3 consecutively bonded carbon atoms.

typically represented by[49, 53]

$$U_d(\phi_{ijkl}) = \sum_{n=0}^6 \frac{1}{2} \Phi_{ijkl} (1 - \cos n\phi) \quad (3.2.4)$$

where Φ_{ijkl} is the potential energy constant and is dependent on the atoms or groups of atoms present. An illustration of this potential is presented in Figure 3.2. It is important that this potential is accurately modeled since it is inherent to the properties of the internal degrees of freedom of the lipid acyl chains and headgroups. In addition, the polypeptide must be accurately modeled. Although all potential terms are equally important to the calculation of interaction forces between components of the lipid-peptide system, the parameters associated with this potential will ensure that peptide conformation is precisely modeled. The dihedral potential term is also important to the lipid components of the simulated bilayer which have many internal rotational degrees of freedom.

The next two terms in the potential describe the electrostatic interactions between charged atoms and the van der Waals interaction. The electrostatic interaction is represented by the Coulomb potential [35, 43]

$$U_e(R_{ij}) = \frac{1}{4\pi\epsilon_0} \frac{q_i q_j}{R_{ij}} \quad (3.2.5)$$

where q_i and q_j are the charges assigned to the atoms i and j , and R_{ij} is the distance between them. Since the potential varies as $\frac{1}{R_{ij}}$ it is considered to be a long range interaction. Early simulation studies provided a cutoff distance beyond which electrostatic interactions were not considered for atoms. However, these simulation methods were unrealistic since in most cases the electrostatic interaction extends beyond the choice of cutoff. In modern simulations, full electrostatic integration is

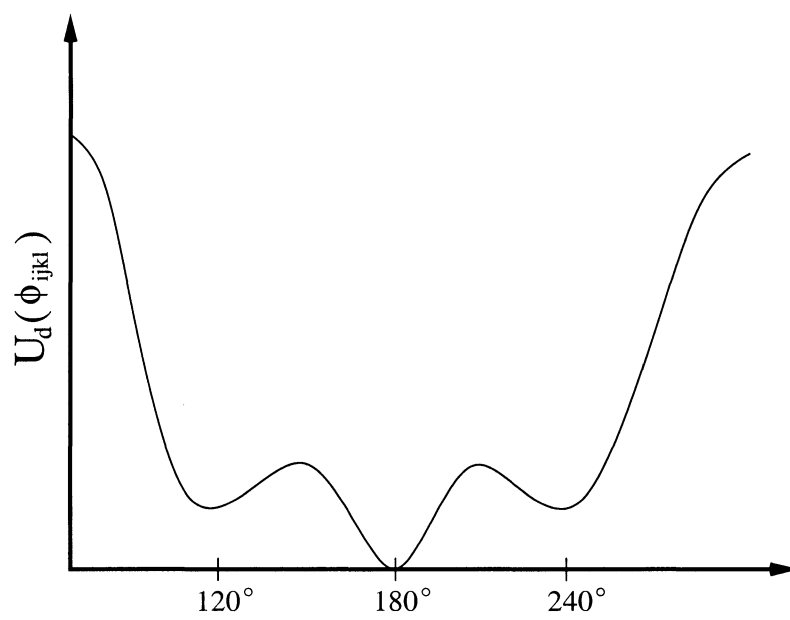


Figure 3.2: The dihedral potential function $U_d(\phi_{ijkl})$. The global minimum is reached when the dihedral angle is 180° or when the chain segment is in a trans conformation. The local minima are reached when the segment of the chain is in either of 2 possible gauche conformations.

employed through the Ewald summation technique. Since this technique is applied in the simulations presented here, a further description is provided.

In the MD simulation, each atom has a set of 3D coordinates and an assigned partial charge. Instead of considering a 3D coordinate space we consider a 1-D space as illustrated in Figure 3.3. The atom is represented by a delta function with a weighting equal to the partial charge [43]. Now, if we wish to calculate the electrostatic potential energy of a small test charge at the point x_0 , we need to sum over all electrostatic potential energy between charges represented in Eq. 3.2.5. There may be a significant contribution to the potential energy even for large distances (on the molecular scale) since the potential varies as $\frac{1}{R_{ij}}$ [43]. For larger 3D systems, the summation would be quite long and very slow computationally. The idea of the Ewald sum is to split a slowly converging summation into two separate sums which both converge rapidly. The first step is to surround each atom position by a distribution whose total charge is equal to the partial charge on the atom but opposite in sign [43]. The distribution has a functional form which extends beyond the position of the partial charge. If we consider the potential energy of a small test charge at the position x_0 it would now see each atom as being surrounded by a cloud of charges which effectively shield it. This summation converges rapidly since the contribution due to each partial charge not only decreases with distance but also has an effective shielding factor due to the surrounding charged cloud [43]. Now, since clouds of charge were set to surround the original partial charges, an additional charge distribution is added which is equal (but opposite in sign to the original) so that we arrive at the proper final result [43]. Now, in order to compute the potential energy of a charge at the position x_0 we still need to carry out a summation over the charge distribution. In fact, solving the potential

at this position involves numerically integrating to solve Poisson's equation [54, 55],

$$\vec{\nabla}^2 \Phi(\vec{x}) = -\frac{\rho(\vec{x})}{\epsilon_0} \quad (3.2.6)$$

which could potentially be a lengthy process. If we consider the Fourier relationships, we have

$$\Phi(\vec{x}) = \int_{-\infty}^{\infty} \Phi(\vec{k}) e^{i\vec{k}\vec{x}} d\vec{k} \quad (3.2.7)$$

$$\rho(\vec{x}) = \int_{-\infty}^{\infty} \rho(\vec{k}) e^{i\vec{k}\vec{x}} d\vec{k} \quad (3.2.8)$$

where $\Phi(\vec{k})$ and $\rho(\vec{k})$ are the potential and charge density in Fourier space. Substitution into Poisson's equation and rearranging yields,

$$\Phi(\vec{k}) = \frac{\rho(\vec{k})}{\epsilon_0 k^2} \quad (3.2.9)$$

which is a purely algebraic expression for the Fourier potential. This is the basis for the numerical particle mesh Ewald (PME) technique [56]. If the charge density has a continuous functional form then it can be laid out on a regularly spaced grid. A fast Fourier transform (FFT) is applied to calculate $\rho(\vec{k})$ from which $\Phi(\vec{k})$ may be calculated algebraically. An inverse FFT is then applied to obtain a numerical estimate of the electrostatic potential in real space. It is often the case that the shielding charge density is chosen to be a Gaussian function. Since the Fourier transform of a Gaussian function is another Gaussian function, the application of FFTs makes the algorithm much faster than the original summation over ordinary electrostatic terms. The Ewald method provides a way to calculate the electrostatic potential accurately but in a very fast manner.

The van der Waals interaction is modeled using the Leonard-Jones 6-12 potential

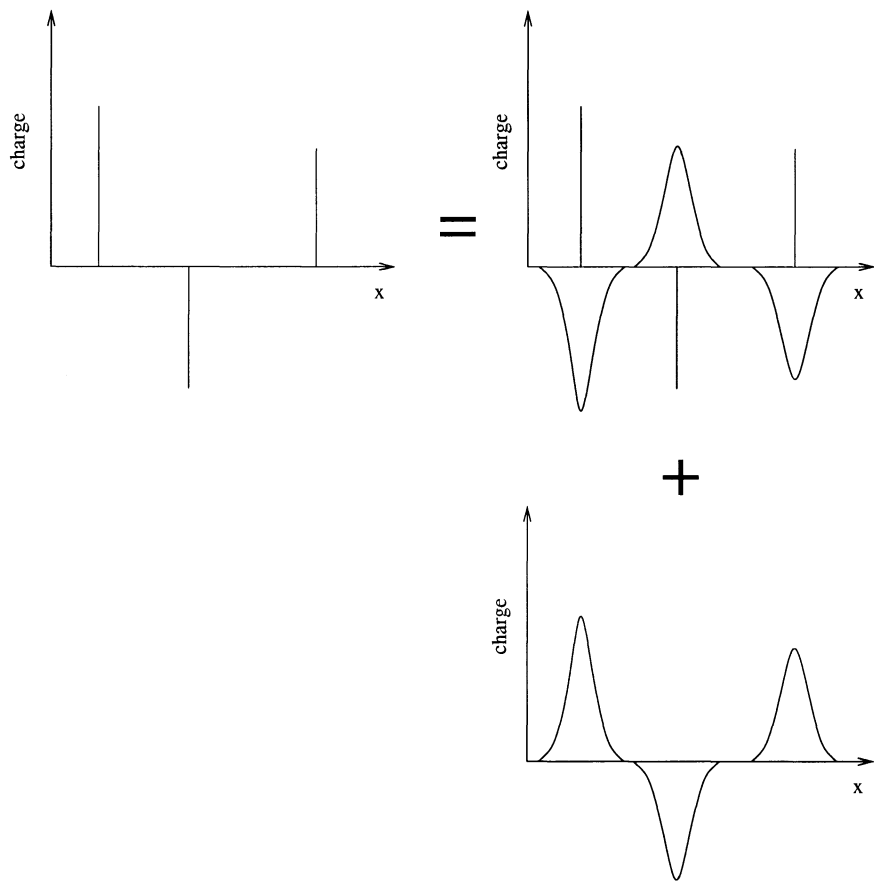


Figure 3.3: The Ewald summation. The summation technique involves splitting the sum into two parts: One part which converges rapidly in real space and another sum which can be calculated more efficiently using Fourier transforms.

[43, 49], namely,

$$U(R_{ij}) = \sum_i^N \sum_{j>i}^N 4\epsilon_{ij} \left(\left(\frac{\sigma_{ij}}{R_{ij}} \right)^{12} - \left(\frac{\sigma_{ij}}{R_{ij}} \right)^6 \right), \quad (3.2.10)$$

where ϵ_{ij} is the potential well depth, σ_{ij} is the equilibrium separation between atoms i and j , and R_{ij} is the distance between atoms i and j . An illustration of this function is included in Figure 3.4(a). This empirical potential has been modeled using a combination of attractive and repulsive terms. To a good approximation, for large internuclear separations (ie $R_{ij} \gg \sigma_{ij}$) the potential is

$$U(R_{ij}) \approx - \sum_i^N \sum_{j>i}^N 4\epsilon_{ij} \left(\frac{\sigma_{ij}}{R_{ij}} \right)^6.$$

The force due to this potential is often considered to be negligible and therefore a cut off is applied such that atoms falling outside the cutoff are not included in the calculation of the potential. A switching function is often applied to the van der Waals potential in order to smoothly force it to zero over a short distance. This is illustrated in Figure 3.4(b). Both electrostatic and van der Waals forces must provide a detailed picture of the inter and intramolecular interactions in the lipid-peptide system.

The final two terms, U_{UB} and U_{imp} , are the Urey-Bradley and improper dihedral potentials respectively [51, 52]. The function forms for these potentials are [51]

$$U_{UB} = \sum_i \frac{1}{2} K_{UB_i} (r_{UB_i} - R_{UB_i})^2 \quad (3.2.11)$$

$$U_{imp} = \sum_i \frac{1}{2} K_{\chi_i} (\chi_i - \chi_{0i})^2. \quad (3.2.12)$$

For the Urey-Bradley potential, K_{UB_i} the summation is a sum over the improper dihedral angles, K_{UB_i} is a force constant, r_{UB_i} is the distance between the two atoms

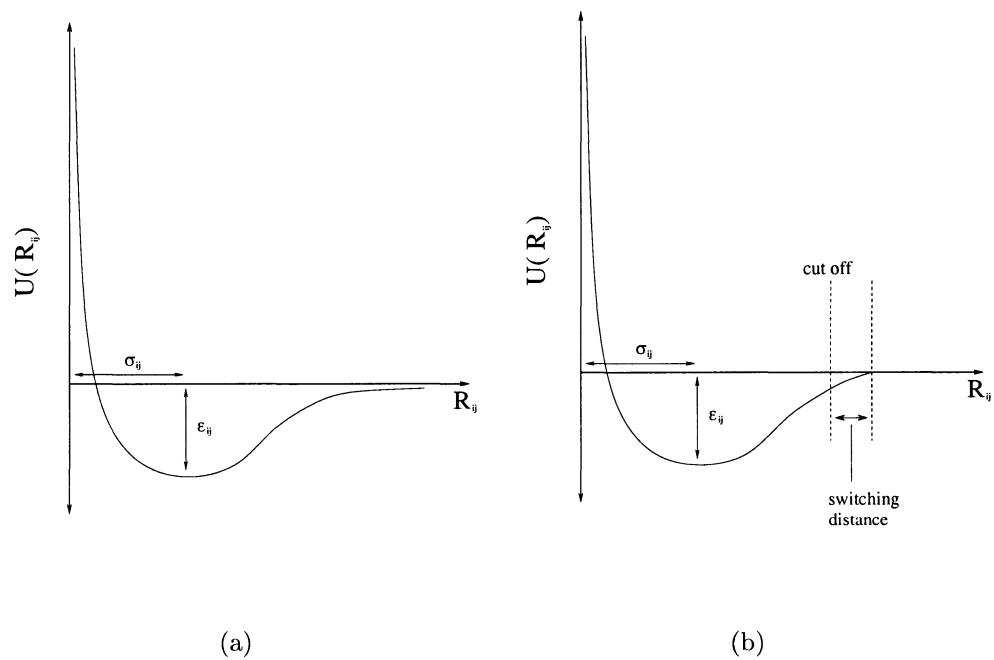


Figure 3.4: (a) The van der Waals potential between two atoms i and j . At small internuclear separations the potential is highly repulsive. For large internuclear separation the potential is slightly attractive. (b) For large internuclear separations the potential is consider to be negligible. A cut off is applied beyond which the contribution to the potential energy is not calculated. A switching function is applied which smoothly forces the potential to zero over a specified distance.

under consideration and R_{UB_i} is their equilibrium separation. For the improper dihedral potential, U_{imp} , K_{χ_i} is the force constant, χ_i is the improper dihedral angle and χ_{0i} is the equilibrium improper angle. These terms are added to the CHARMM when the angle potential term, U_a , does not accurately describe the interaction between 3 atoms, and since they often provide a better fit to experimental data [52].

As previously stated this force field has been used extensively in MD studies of a wide variety of biological systems of lipids and proteins [17, 47, 48]. Simulations which employ the CHARMM potential function agree well with experimental studies on similar biological systems. Based on this, we are confident that the CHARMM force field will accurately describe interactions within the lipid peptide system investigated in this thesis.

3.3 The Equations of Motion

It is desirable to produce MD trajectories such that the time average over the trajectory produces some statistical ensemble. For biological systems, simulations at fixed temperature and pressure provide the most realistic scenario. The lipid-peptide system presented in this work is therefore simulated at constant temperature and pressure.

The equations of motion of the atoms in the MD simulation are often similar to Newton's equations which may be derived from the Lagrangian [50],

$$L = \sum_{i=1}^N \frac{1}{2} m_i \dot{r}_i^2 - U(\vec{r}^N) \quad (3.3.1)$$

where the summation is over the number of atoms and $U(\vec{r}^N)$ is the interaction potential described in the previous section. However, under the conditions where volume may fluctuate (*i.e.* in an NPT ensemble as used here), Newton's equations and the

above Lagrangian are not sufficient to describe these interactions. Instead, Andersen [57] has proposed the extended Lagrangian formulations in which the system is coupled to extra degrees of freedom that regulate pressure and temperature. Writing the positions as scaled quantities relating to the volume of the simulation cell [49],

$$r_i = s_i V^{\frac{1}{3}}, \quad \dot{r}_i = \dot{s}_i V^{\frac{1}{3}},$$

and treating the volume as a dynamical variable, the extended Lagrangian may be written as [43, 49]

$$L = \sum_{i=1}^N m_i \dot{s}_i^2 V^{\frac{2}{3}} - U(\vec{r}^N) + \frac{1}{2} M \dot{V}^2 - P_0 V \quad (3.3.2)$$

for particles in a volume V which may undergo isotropic fluctuations. In this equation M is equivalent to the mass of a piston which is used to regulate the system pressure [58]. From the Lagrangian we then obtain,

$$\ddot{s}_j = \frac{F_j}{m_j V^{\frac{1}{3}}} - \frac{2 \dot{V}}{3 V} \dot{s} \quad (3.3.3)$$

and

$$M \ddot{V} - \left(\sum_{i=1}^N \frac{1}{3V} m_i \dot{s}_i^2 V^{\frac{2}{3}} - \frac{\partial U(r^N)}{\partial V} - P_0 \right) \quad (3.3.4)$$

for the dynamical equations of motions for the system. Substituting,

$$\begin{aligned} \frac{\partial U(r^N)}{\partial V} &= \sum_{k=1}^N \frac{\partial U(r_1, r_2, \dots)}{\partial r_k} \frac{\partial r_k}{\partial V} \\ &= - \sum_k \frac{1}{3V} F_k s_k V^{\frac{1}{3}} \end{aligned} \quad (3.3.5)$$

we obtain

$$M \ddot{V} - \left(\sum_i \frac{1}{3V} \{m_i \dot{s}_i^2 V^{\frac{2}{3}} + F_k s_k V^{\frac{1}{3}}\} - P_0 \right). \quad (3.3.6)$$

Finally, recognizing the first term as the instantaneous pressure one can write [58],

$$\begin{aligned}
 M\ddot{V} &= (P_{int} - P_0) \\
 &= -\frac{B}{V_0}(V - V_0)
 \end{aligned}
 \tag{3.3.7}$$

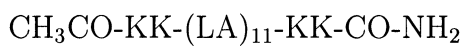
where B is bulk modulus and V_0 is the simulation cell equilibrium volume. The last equation of motion is analogous to a piston of mass M acting under the influence of a pressure gradient where the difference between external and internal pressure drives the volume fluctuations of the system. Andersen [57] extended this approach to allow anisotropic fluctuations of the system cell volume. Andersen proved that the solution to these equations produced trajectories in the isobaric-isoenthalpic ensemble (NPH; constant number, constant pressure, constant enthalpy) [58]. Nosé and Klein extended the work of Andersen to the case of non-cubic simulation cells and derived a new Lagrangian for the extended system [59]. The extended system method for propagating the MD system may be combined with a suitable temperature coupling scheme to produce the isothermal-isobaric ensemble (NPT; constant number, constant pressure, constant temperature)[57, 60]. These dynamical equations provide the most realistic description of the lipid-peptide simulation carried out in this work. The equations of motion are integrated using an extended verlet algorithm. This algorithm and an indepth discussion of the extended equations of motion have been presented by Frenkel [43].

Chapter 4

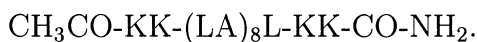
Experimental Setup and Details

4.1 Sample Preparation

Sequences of the peptides used in the first part of this study were



and



The two peptides used in the second part of this study were



and



where the lowercase A represents the position of the deuterated methyl group and the italicized characters represent the GPA motif. All peptides were synthesized at the Peptide Synthesis Laboratory at Queen's University (Kingston, ON). These peptides were labeled at selected sites using methyl deuterated alanines supplied by

Dr. C. W. M. Grant. The positions of deuterated alanine methyl groups in the specific peptide sequences used in the first study are identified in Table 4.1. Those samples were prepared in Dr. C. W. M. Grant's laboratory (Dept. of Biochemistry, University of Western Ontario) by Simon Sharpe. Peptides containing the GPA motif were incorporated into bilayers locally in Dr. K. Keough's laboratory (Dept. of Biochemistry, Memorial University) with the assistance of Mrs. June Stewart. For both parts of this work 1-palmitoyl-2-oleoyl-3-sn-phosphatidylcholine (POPC) was obtained from Avanti Polar Lipids (Birmingham, AL) and was used without further purification.

The protocol for preparation of samples used in the first part of this study is described below. Since the peptides are very hydrophobic and stick quite readily to glassware, an organic solvent composed of 90% formic acid/ acetic acid/ chloroform/ trifluoroethanol (1:1:2:1 ratio by volume) was used to dissolve the dry peptide and the appropriate amount of POPC lipid, to produce mixtures composed of 0.5 and 6 mol % peptide for each of the two peptides. Samples were allowed to sit at least 30 min until they appeared to be dissolved. The solvent was then removed under slight vacuum at 55 °C on a rotary evaporator, leaving thin films on the bottom of round flasks. These samples were then vacuum desiccated for 18 hours at 23 °C under high vacuum. The samples were then hydrated with 30 mM HEPES buffer, 20 mM NaCl, and 5 mM EDTA which had a pH between 7.1 to 7.3. All solutions and buffers were made using deuterium depleted water. The samples were then lyophilized for several hours in order to remove any residual solvent. This step was repeated several times and the pH was then adjusted to 6.5.

Peptide Sample	Peptide Sequence
LA17-1	CH ₃ CO-KK-LALALALALaLALALAL-KK-CO-NH ₂
LA22-1	CH ₃ CO-KK-LALALALALALaLALALALALA-KK-CO-NH ₂
LA22-2	CH ₃ CO-KK-LALALALALALaLaLALALALA-KK-CO-NH ₂
LA22-7	CH ₃ CO-KK-LALALaLaLaLaLaLaLaLaLALA-KK-CO-NH ₂

Table 4.1: Peptide sequence and deuterium label positions in LA peptides used in this study. The number appended to the LA peptide sample prefix indicates the number of hydrophobic residues in the amino acid sequence. The lowercase A's represent the position of alanine deuterated methyl groups. The number following the "-" indicates the number of deuterated alanines.

In the second part of this study samples composed of alanine deuterated transmembrane helices with GPA transmembrane motifs were prepared using the protocol described above. However, the amount of peptide and the appropriate amount of POPC were chosen to produce mixtures composed of 4 mol % peptide for each of the peptides with GPA motifs.

4.2 ^2H NMR Spectrometer Setup and Experimental Details

The experimental work was carried out on a solid state ^2H NMR spectrometer constructed in-house using a superconducting magnet with a field strength of 9.4 T (Magnex Scientific, Concord, CA) which corresponds to a ^2H resonance frequency of 61.4 MHz. The spectrometer utilizes heterodyne detection [29] and phase shifting at 10 MHz.

The operation of the spectrometer is illustrated in the spectrometer block diagram presented in Figure 4.1. The PTS 160 frequency synthesizer provides two base signals: one at 10 MHz and the other at 71.4 MHz which serve several purposes. The 10 MHz signal is supplied to the quadrature detector and to a pulse generator. The 71.4 MHz signal is supplied to a mixer in the receiver and to mixers in the single sideband generator.

The pulse generator has the capability of generating pulses with four set phases (*i.e.* 0° , 90° , 180° , and 270°) and the duration of the pulses or times between successive pulses are controlled by a homebuilt pulse programmer. Pulse sequence timings are generated on a pentium class computer running Windows NT. Software for this spectrometer setup was written in Visual Basic 6.0 and is used for generation of pulse

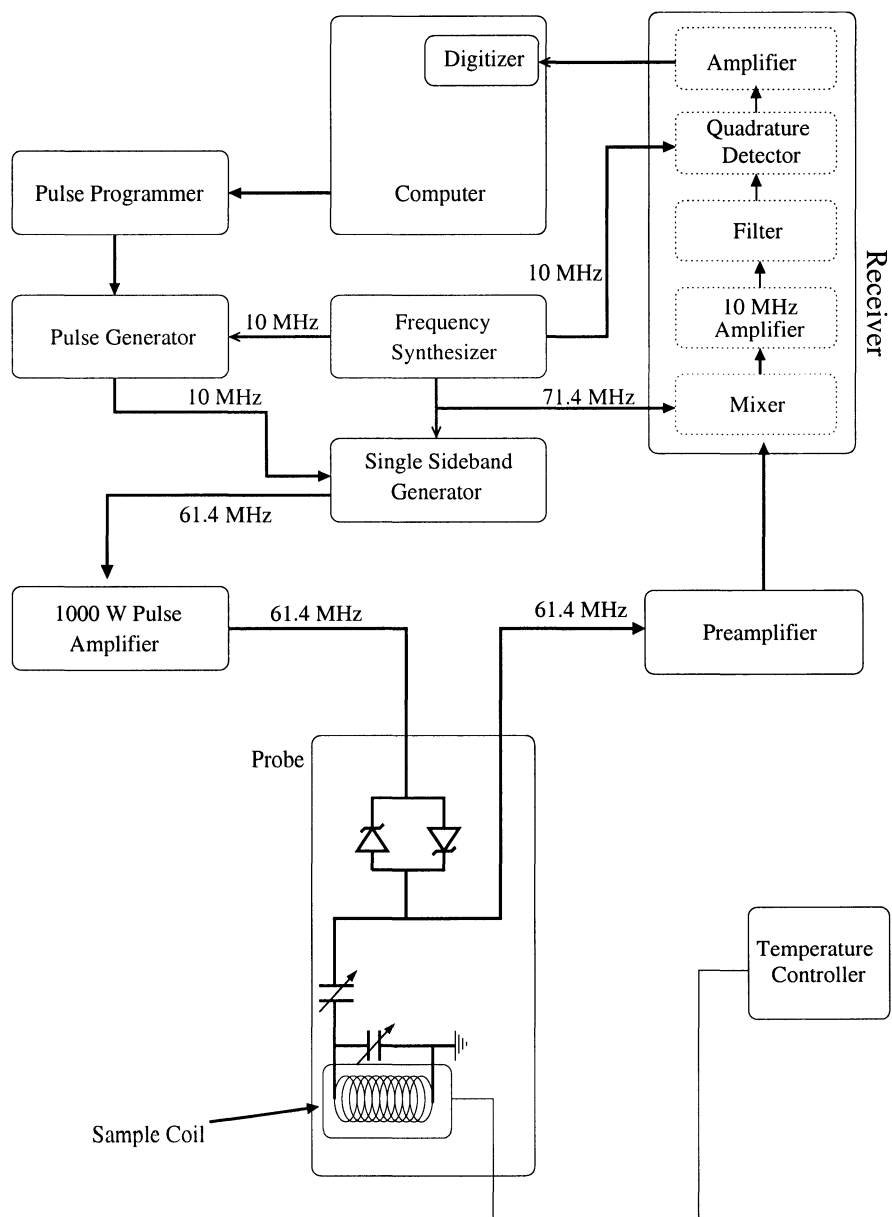


Figure 4.1: Block diagram of the ^2H NMR spectrometer.

sequence timings, data acquisition and analysis.

The pulse timings are uploaded to the pulse programmer and the phased 10 MHz pulse output from the pulse generator is then fed into the single sideband generator where it is mixed with the 71.4 MHz signal to produce the 61.4 MHz ^2H magnetic resonance frequency. This signal is then amplified by an ENI LPI-10 1000 W pulse amplifier (ENI, Rochester, NY) and transmitted to the resonant NMR probe circuit.

The inductor in the probe circuit transmits RF radiation to the sample enclosed by the inductor/coil and also detects the weak NMR signal resulting from perturbation of the spin system. In the peptide systems investigated here, the ^2H NMR signal has a Larmor frequency of 61.4 MHz and has a spectral width of 1 to 20 kHz. The NMR signal from the probe is amplified by a MiteQ AL-1440 preamplifier (Hauppauge, NY). It is then mixed with a 71.4 MHz signal from the frequency synthesizer resulting in a 10 MHz signal modulated by the FID. The signal is further amplified and then passes through a filter.

The NMR signal is then fed through the quadrature detector which is illustrated in Figure 4.2. Inside the quadrature detector the 10 MHz signal from the frequency synthesizer is split into two signals with phases of 0° and 90° . The 10 MHz signal from the mixer is split into two signals and mixed with the 0° and 90° signals from the phase splitter. The real channel and imaginary channel signals are then amplified and measured using a Datel 416pci digitizer board in the computer through Visual Basic Software written specifically for this spectrometer setup.

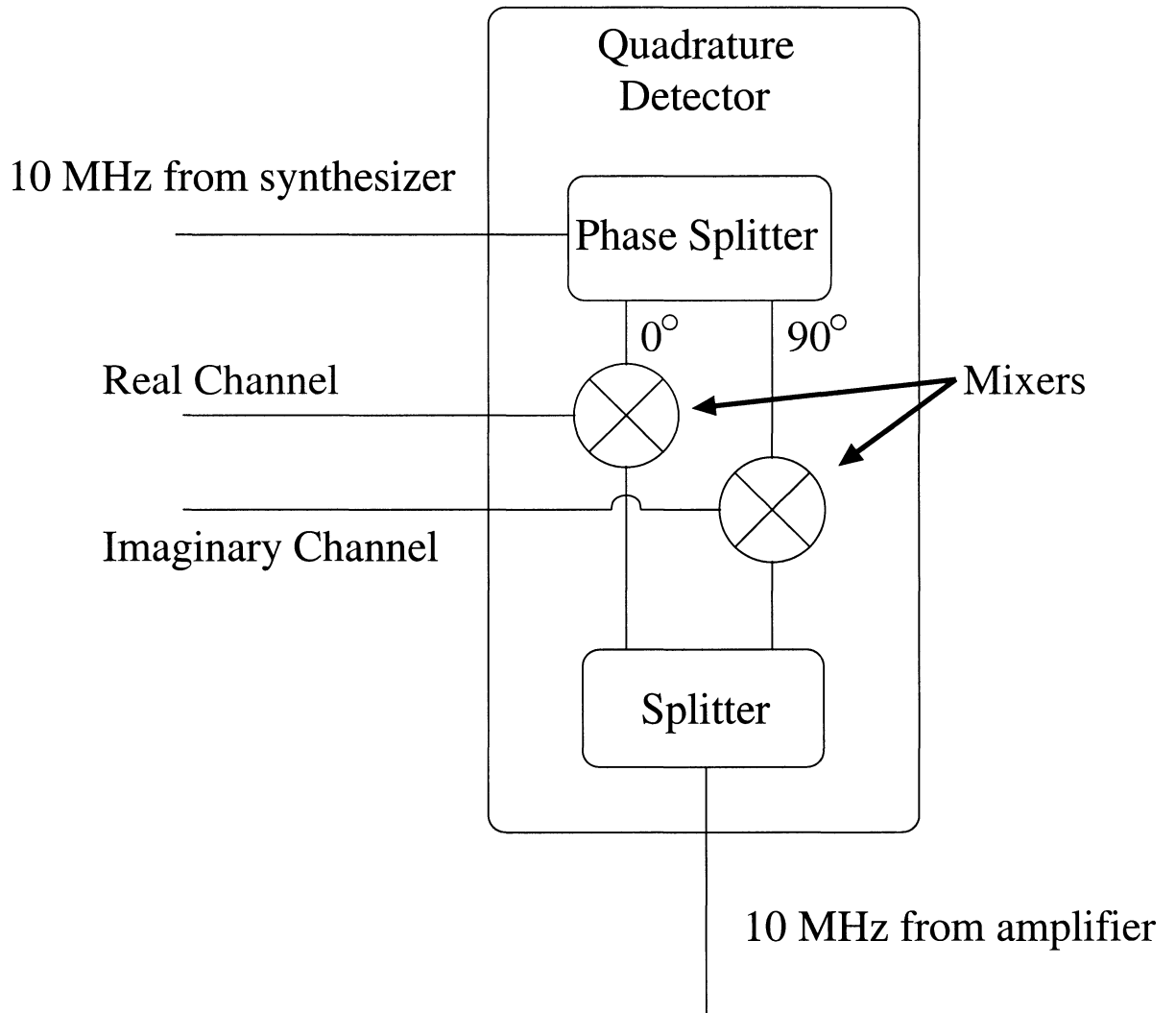


Figure 4.2: Block diagram of the quadrature detector.

4.3 ^2H NMR Spectroscopy

In this study the quadrupolar echo sequence discussed in section 2.4 was employed [30] for acquisition of NMR spectra and quadrupole echo decay measurements. Phase cycling was employed for all measurements.

Several NMR sample coils were used for the measurements in order to accommodate the varying sizes of sample containers. The $\pi/2$ pulse lengths were typically 2.5 μs to 3 μs for the 5 mm RF coil and 6.5 μs to 7 μs for the 10 mm coil. For acquisition of spectra the separation between $\pi/2$ pulses was set to 35 μs and 250,000 to 600,000 transients were collected depending on the sample size. During echo decay measurements the $\pi/2$ pulse separation varied from 35 μs to 100 μs and 100,000 transients were accumulated at each pulse separation. For all measurements, a dwell time of 1 μs was used. The FID data were subsequently analyzed to yield an effective dwell time of 4 μs , corresponding to a spectral width of 250 kHz. Additionally, repetition times from 0.3 s to 0.8 s were used between acquisition of individual transients in order to allow complete longitudinal relaxation of nuclear magnetization.

The experiments described above were carried out at a series of temperatures between 25 °C and 60 °C. The probe sample coil was enclosed in a copper oven by which the temperature was controlled through a home-built microprocessor-based temperature controller. This temperature controller uses an ADAC (Woburn, MA) DIRECT CONNECT™ 5508TC thermocouple and millivolt data acquisition card to control temperature through software written by S. Gammon using the C programming language. Each sample was initially warmed to a target temperature after which a single spectrum and several quadrupole echo decay measurements for varying pulse separations were acquired. The sample was then cooled and the same measurements were

performed down to 25 °C. Experiments (spectra and quadrupole echo) were started approximately 1 hour after temperature stabilized from either warming or cooling to the target temperature to ensure equilibration of the sample.

The ^2H NMR probe used in this study was designed and built by Dr. M. R. Morrow especially for the 9.4T Magnex superconducting magnet. The probe circuit is illustrated in Figure 4.1. The probe circuit contains an inductor (sample coil) and two variable capacitors which are used to match the frequency of the probe circuit to the deuteron resonance frequency. Since the NMR signal is very weak, a parallel set of crossed diodes are in place to eliminate noise from the high power RF amplifier described in Section 4.1.

Chapter 5

^2H NMR Studies of Transmembrane Polypeptides: Polyalanine-leucine

5.1 Introduction

The quadrupolar interaction of a deuteron attached to a biological molecule is orientation dependent and thus very useful as a probe of structure and motion in anisotropic, partially ordered environments like biological membranes. The ^2H NMR spectrum is sensitive to motions and structural changes which occur over a fairly large time scale (*i.e.* 10^{-9} - 10^{-3} s) and relaxation measurements provide some insight into molecular dynamics. The spectrum resulting from the perturbation of the deuterium Zeeman levels by the quadrupolar interaction reflects molecular dynamics and structural information. The quadrupolar splitting of the prominent 90° edges in the Pake doublet spectrum obtained from the ^2H NMR experiments on methyl group deuterated polypeptides is given by

$$\Delta\nu_Q = \frac{1}{4} \frac{e^2 Q q}{h} \left(\frac{3 \cos^2 \theta - 1}{2} \right) \left\langle \frac{3 \cos^2 \beta - 1}{2} \right\rangle \quad (5.1.1)$$

for molecules that are undergoing rapid rotation about an axis oriented at angle θ with respect to the applied magnetic field. In this equation β is the angle between the axis of rotational symmetry and methyl group bond axis. The average is over the changes in the orientation of the methyl group symmetry axis with respect to the molecular rotational axis of symmetry.

Figure 5.1 illustrates four amino acids and their respective side-chains. The larger side chains for peptide segments are free to undergo large amplitude fluctuations such as 180° phenyl ring flips for the side-chain of tyrosine [61]. Motion of deuterated side chains complicates spectral interpretation so minimal side chain motion is preferable for an investigation of polypeptide structure, orientation, and dynamics. Deuterated alanine methyl groups have proven to be useful probes for investigating transmembrane polypeptides in bilayer environments since the methyl group axis orientation with respect to the helix axis is heavily restricted (due to the rigidity of the carbon-carbon bond attached to the alanine peptide) and thus directly reflects helix backbone structure and dynamics [6, 7, 18, 62].

Previous ^2H NMR studies of the transmembrane domain of deuterated alanine methyl groups on epidermal growth factor receptor (EGFR) transmembrane segments carried out by Morrow *et al.* [6] indicate that these segments undergo rapid axially symmetric rotation on a time scale shorter than the NMR experiment (*i.e.* $< 10^{-5}$ s). In those experiments the transmembrane domains behaved mainly as monomers but spectral broadening with decreasing temperature suggested some side-to-side association of transmembrane segments. Quadrupolar splittings obtained by Jones *et al.* [7] demonstrated that the EGFR transmembrane segment is likely tilted and undergoing rapid rotation about the bilayer normal with no rotation about the helix

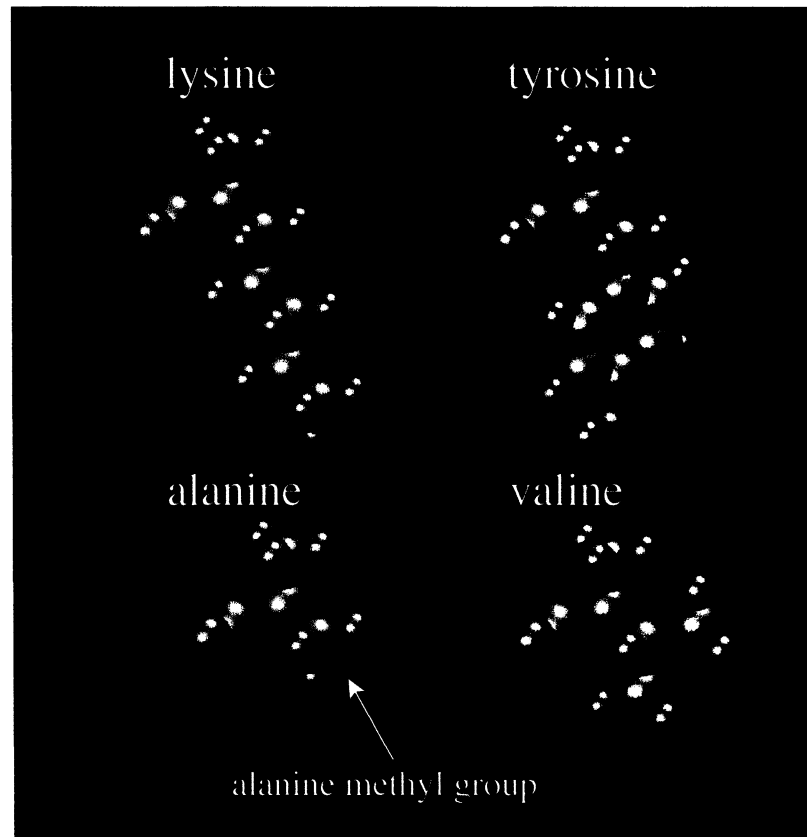


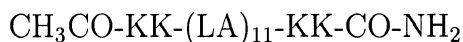
Figure 5.1: Four amino acid residues including lysine, tyrosine, alanine, and valine. Peptide side chains can undergo large amplitude fluctuations within the fluid bilayer interior. However, the alanine methyl group can only undergo rapid rotation about the bond attached to the peptide backbone. Red represents hydrogen, green represents carbon, blue represents nitrogen, and purple represents oxygen.

axis. An interesting question which arises here is whether rapid rotation about the bilayer normal is inherent to specific natural transmembrane segments or is a general property of transmembrane polypeptides.

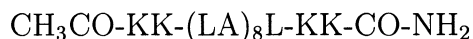
In order to investigate some of the properties of the transmembrane domain of natural proteins, we have studied model peptides composed of LA subunits. These peptides are simpler than the transmembrane segments of natural proteins. The uniform sequences used here may remove or modify specific peptide-peptide and peptide-lipid interactions so we can further clarify the dynamics of polypeptides in bilayers and gain insight into the behaviour of transmembrane segments of natural proteins.

5.2 Polyalanine-leucine

The KALP polypeptides investigated in this part of the study are more symmetric than transmembrane segments of natural proteins like EGFR which often have interaction motifs that are thought to promote protein association. The sequence of alternating alanines and leucines may remove specific interactions between side chains of transmembrane segments. Since ^2H NMR spectra are sensitive to molecular orientation and motions, these experiments can provide information about the peptide dynamical properties, the interactions between polypeptides and interactions with bilayer membranes. The peptide sequences used in the first part of this study are



and



which both give rise to α -helical geometry [19, 20]. These simple peptides have a uniform hydrophobic region composed of LA subunits and are terminated by charged

lysine residues. The peptides have different hydrophobic lengths which are based on the number of amino acid residues with non-polar side chains. In this case, the peptides have hydrophobic lengths of 22 and 17 residues respectively. Since the peptides are composed of repeat LA subunits, the sequences are therefore referred to as LA22 and LA17. Each of these peptides has been deuterated at a single position within the peptide sequence. The peptide samples investigated here and the positions of the methyl group label for each peptide are presented in Table 5.1. Peptide sequences used in a related study of the same peptides have also been included in Table 5.1. In that study, the peptides had several labeled methyl groups (see Table 5.1). Comparison of observed spectra from that study with current observations enable us to assign quadrupolar splittings obtained from the NMR experiments to a particular methyl group label. Each polypeptide was investigated at concentrations of 6 mol % and 0.5 mol %. Spectra and quadrupolar echo decay measurements were acquired at 4 different temperatures for the samples with a peptide concentration of 6 mol%. Echo decay measurements were not carried out on samples with a peptide concentration of 0.5 mol % because of signal-to-noise considerations. The initial goal of this study is to see if a uniform helix displays any rotation about the helix axis and to see if peptide-peptide interactions for uniform helices affect peptide dynamics.

5.3 Results

Selected spectra obtained for these polypeptides with a single deuterated methyl group are shown in Figures 5.2 through 5.5. At higher temperatures the observed spectra are Pake doublets for both LA22-1 and LA17-1 peptides. The Pake doublet spectrum reflects rapid axially symmetric motion of the peptides. As noted in Chapter

Peptide Name	Peptide Sequence
LA17-1	CH ₃ CO-KK-LALALALALaLALALAL-KK-CO-NH ₂
LA22-1	CH ₃ CO-KK-LALALALALALaLALALALALA-KK-CO-NH ₂
LA22-2	CH ₃ CO-KK-LALALALALALaLaLALALALA-KK-CO-NH ₂
LA22-7	CH ₃ CO-KK-LALALaLaLaLaLaLaLaLALA-KK-CO-NH ₂

Table 5.1: Peptide sequence and deuterium label positions in LA peptides used in this study and a collaborative study. The number appended to the LA peptide sample prefix indicates the number of hydrophobic residues in the amino acid sequence. The lowercase A's represent the position of alanine deuterated methyl groups. The number following the "-" indicates the number of deuterated alanines. Single labeled peptides were investigated in this work while peptides with multiple labels were investigated in previous work.

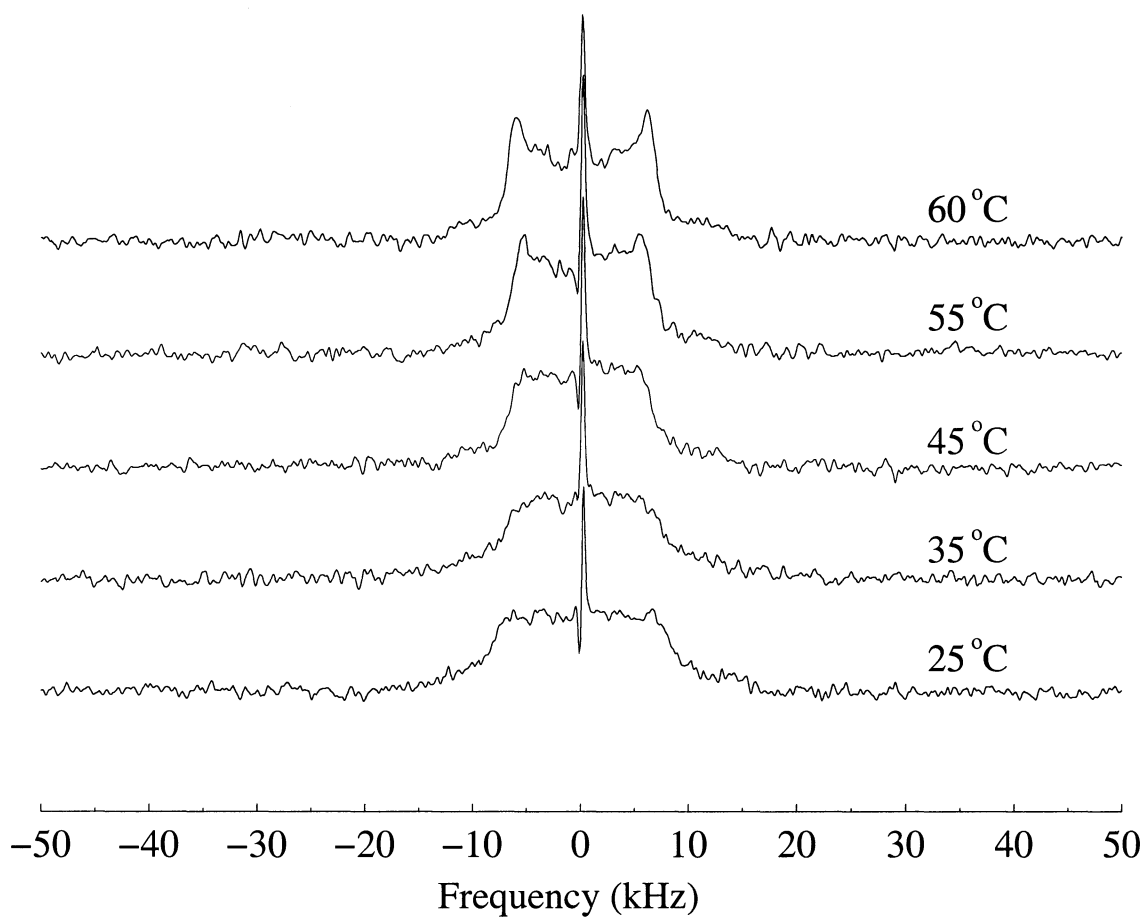


Figure 5.2: ^2H NMR spectra corresponding to a concentration of 6 mol % alanine deuterated $\text{CH}_3\text{CO-KK-(LA)}_{11}\text{-KK-CO-NH}_2$ (LA22-1) dispersed in POPC bilayers at varying temperatures. The spectrum at 60 °C indicate that the transmembrane segment is undergoing rapid axially symmetric motion. At lower temperatures spectral broadening resulting from hindered rotation is suggestive of peptide association. The position of the deuterated methyl group is indicated in Table 5.1.

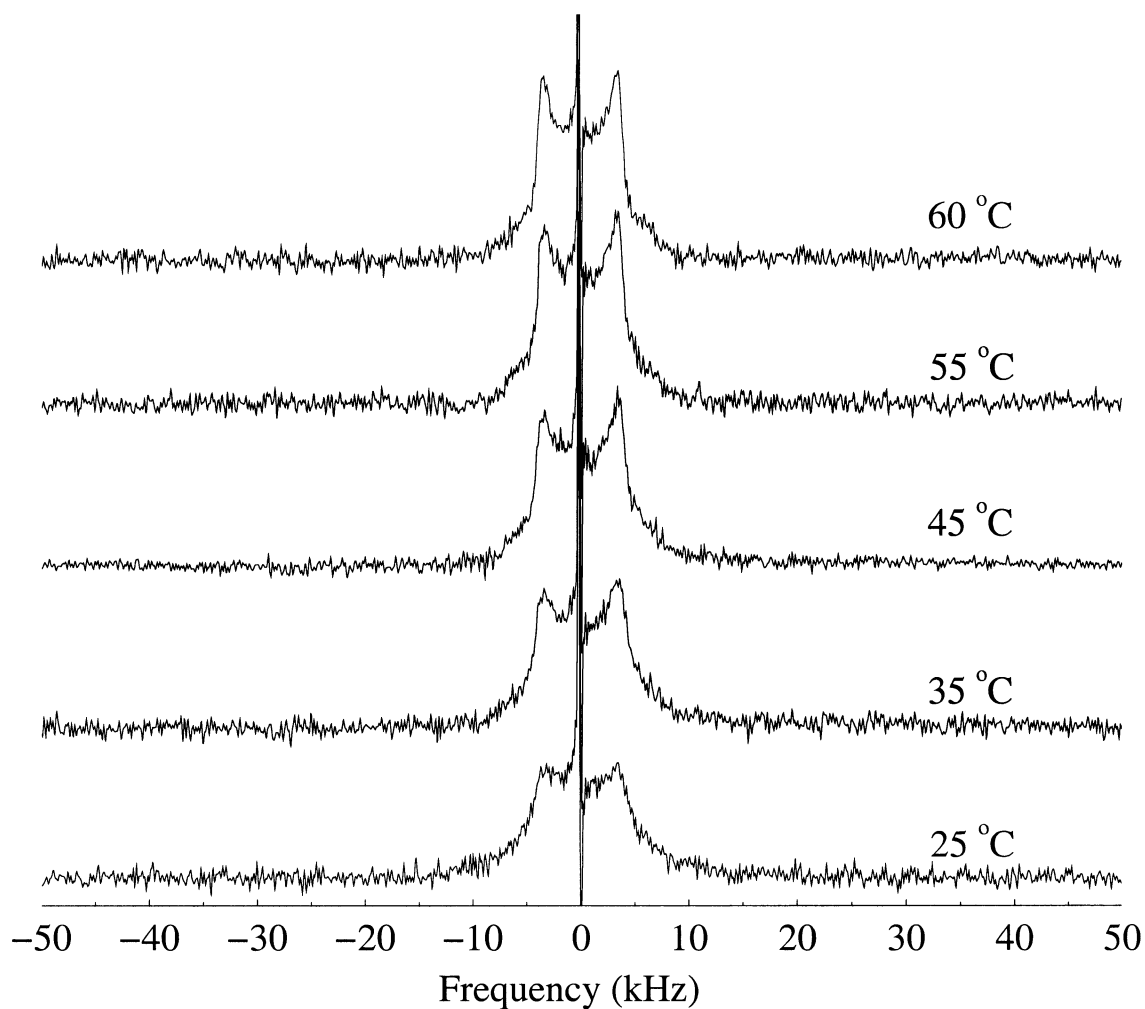


Figure 5.3: ^2H NMR spectra correspond to a concentration of 6 mol % alanine deuterated $\text{CH}_3\text{CO-KK-(LA)}_8\text{L-KK-CO-NH}_2$ (LA17-1) at varying temperatures. The spectrum at 60 °C indicates that the transmembrane segment is undergoing rapid axially symmetric motion. At lower temperatures spectral broadening resulting from hindered rotation suggests peptide association. The position of the deuterated methyl group is indicated in Table 5.1.

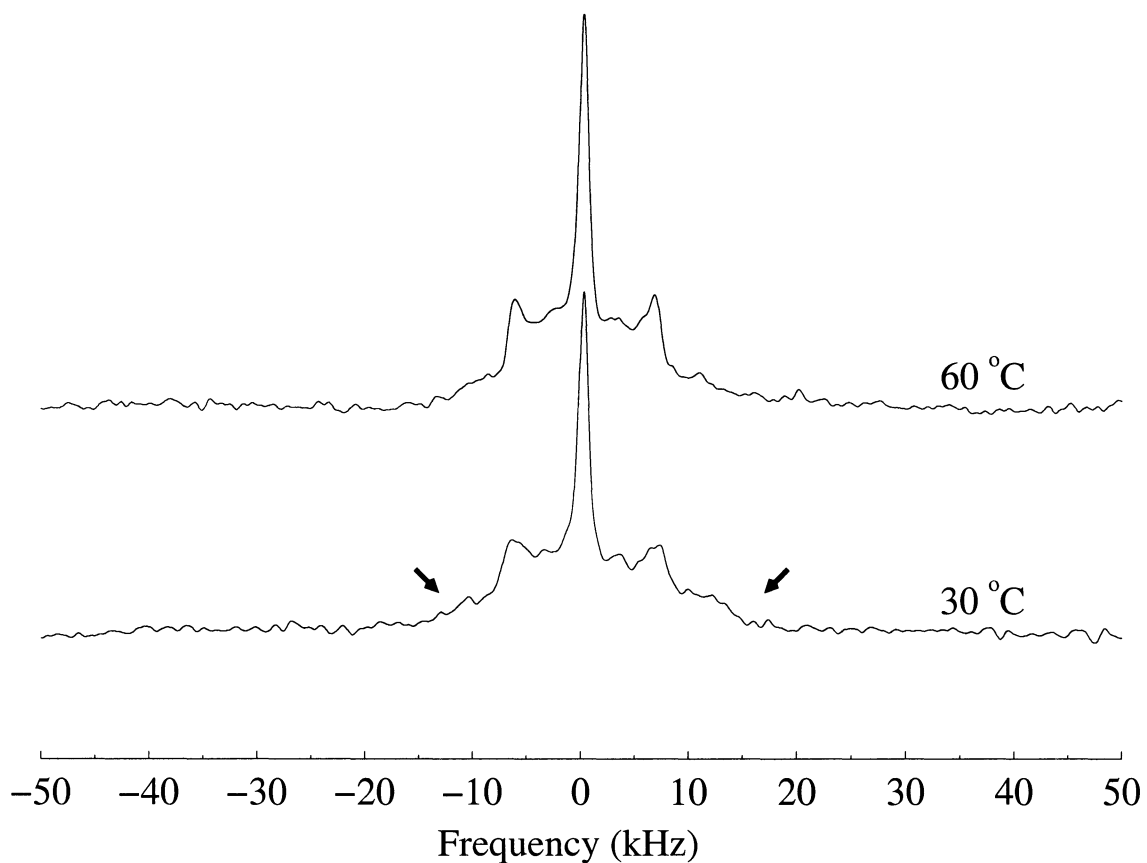


Figure 5.4: ^2H NMR spectra corresponding to a concentration of 0.5 mol % alanine deuterated $\text{CH}_3\text{CO-KK-(LA)}_{11}\text{-KK-CO-NH}_2$ (LA22-1) at 60 °C and 30 °C in POPC bilayers. The spectrum at 60 °C indicates that the transmembrane segment is undergoing rapid axially symmetric motion. At lower temperatures spectral broadening resulting from asymmetric motion is suggestive of peptide association. A low amplitude feature is apparent in the spectra and the splitting indicated by arrows. The position of the deuterated methyl group is indicated in Table 5.1.

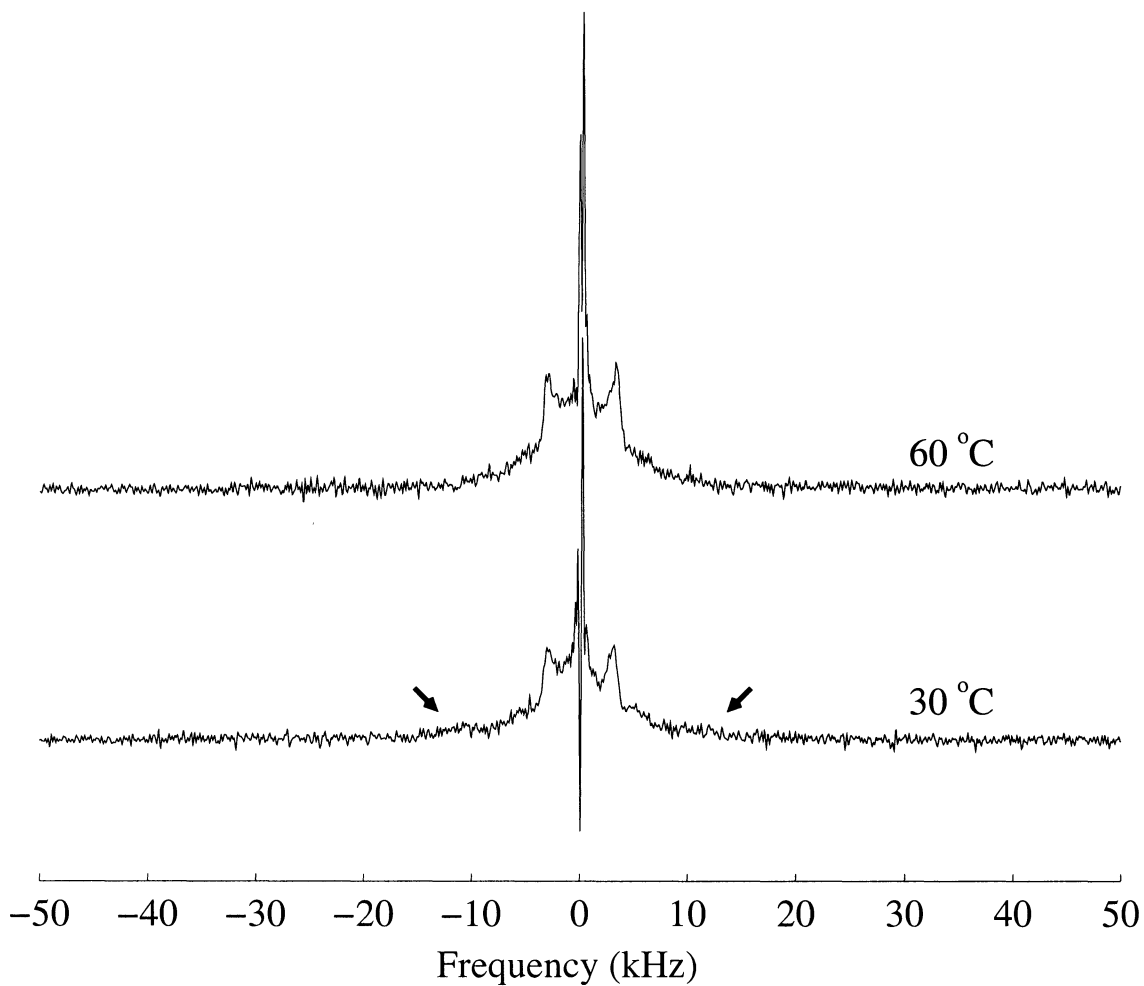


Figure 5.5: ^2H NMR spectra correspond to a concentration of 0.5 mol % alanine deuterated $\text{CH}_3\text{CO-KK-(LA)}_8\text{L-KK-CO-NH}_2$ (LA17-1) at 60 °C and 30 °C in POPC bilayers. The spectrum at 60 °C indicates that the transmembrane segment is undergoing rapid axially symmetric motion. At lower temperatures spectral broadening resulting from asymmetric motion is suggestive of peptide association. A low amplitude feature is apparent in the spectra and the splitting indicated by arrows. The position of the deuterated methyl group is indicated in Table 5.1.

2, the quadrupolar splitting of a rapidly rotating deuterated alanine methyl group on an immobile polypeptide is

$$\Delta\nu_Q = \frac{1}{4} \frac{e^2 Q q}{h} \left(\frac{3 \cos^2 \beta - 1}{2} \right) \quad (5.3.1)$$

where β is the angle between the applied magnetic field and the methyl group rotation axis. Assuming the quadrupolar coupling constant is 167.5 kHz and taking $\beta = 90^\circ$, Equation 5.3.1 gives a splitting of 41.85 kHz for the prominent edges of the Pake doublet for alanine methyl deuterons on immobilized peptides. The observed 90° splittings from Figures 5.2 through 5.5 are significantly less than this estimate so it is apparent that the observed spectra do not result from static polypeptides. Additionally, since the spectra are indicative of rapid axially symmetric motion, the time scale of the motion contributing to narrowing of the spectrum must be less than the characteristic timescale for the NMR experiment (ie 10^{-6} s - 10^{-5} s). It is interesting to note that the quadrupolar splittings of the Pake doublet 90° edges for each peptide are different. This observation suggests that the average orientation of the methyl group rotation axis with respect to the molecular rotation axis is different for the two peptides. The central line in each of the spectra is probably due to natural abundance deuterium in the water contained between the lipid bilayers. This feature could also be due to lateral diffusion of the peptides around small lipid vesicles. Some of the spectra appear to be non-symmetric about the central resonance. This is probably due to a frequency dependent phase shift artifact resulting from an imperfect spectrometer.

The Pake doublet, which is indicative of axially symmetric motion, becomes less well defined at lower temperatures and therefore reflects hindered rotation. Although the Pake feature disappears for LA22-1 peptides (at a concentration of 6 mol %) at

lower temperatures, it is still somewhat apparent for spectra obtained from LA17-1 peptides at a concentration of 6 mol %. The change in the shape of the spectra with decreasing temperature is more pronounced for longer LA22-1 peptides which suggests that peptide length may be an important factor in determining the dynamics of peptides in membranes. In any case, the spectra obviously indicate that decreasing temperature leads to a distinct change in peptide dynamics for both peptides.

It is important to note that the temperature dependence of peptide dynamics also appears to be sensitive to peptide concentration in bilayers. Comparing the spectra for peptide concentrations of 6 mol % (Figures 5.2 and 5.3) and 0.5 mol % (Figures 5.4 and 5.5) it can be seen that there is a distinct difference in the spectral features. At a peptide concentration of 6 mol %, spectra for LA22-1 peptides become broadened with decreasing temperature and therefore indicate that peptide reorientation is hindered. However, at a concentration of 0.5 mol % the observed spectra for the LA22-1 peptide are indicative of rapid axially symmetric motion even at 30 °C though there appears to be some spectral broadening. Similarly, at a concentration of 6 mol %, spectra for LA17-1 peptides exhibit a greater degree of broadening than for 0.5 mol % LA17-1 peptides at a given temperature. The observed spectra for the LA17-1 peptide (at a concentration of 0.5 mol %) are indicative of rapid axially symmetric motion even at 30 °C though there appears to be some changes in spectral features compared to 60 °C. It is also apparent that the Pake doublet spectra for LA17-1 peptides at 0.5 mol % concentration are better resolved than for LA22-1 peptides at 0.5 mol %. This illustrates the sensitivity of peptide dynamics to both peptide length and concentration. The peptides presented here are undergoing rapid rotational diffusion about the bilayer normal, the rate of which is expected to decrease with decreasing

temperature. As the rate of rotational diffusion decreases, the spectra are expected to broaden and become less sharp. However, we note that at 0.5 mol % the peptides exhibit Pake doublet spectra even at 30 °C. Although some of the observed broadening may be due to the decreasing rate of rotational diffusion as temperature is decreased, this alone would not account for the changes observed in the spectra at 6 mol %. This suggests that the observed broadening results from interference between peptides which are more crowded at higher concentrations.

The spectra obtained for LA17-1 and LA22-1 peptides at a concentration of 0.5 mol % both exhibit a broad, low amplitude feature with a splitting less than 25 kHz. This feature is more apparent in spectra obtained for LA17-1 peptides and is highlighted with arrows in Figures 5.4 and 5.5. The feature is somewhat apparent in LA22-1 spectra at 0.5 mol % but is probably buried under the 0° edges of the spectrum. The width of the feature is less than the 41.85 kHz splitting expected for deuterated methyl groups on immobile peptides. Therefore, this broad feature does not result from deuterated methyl groups on static polypeptides. The width of the feature does indicate that there must be some averaging of the quadrupolar interaction but the rotation of the peptides is significantly hindered. The magnitude of the splitting compared to the splitting of the 90° edges suggests that the orientation of the peptide with respect to the rotational symmetry axis is also modified.

Molecular motions modulate the amplitude of the quadrupolar echo and therefore echo decay measurements reflect peptide dynamics. Based on the measured echo decay times, the correlation time for peptide reorientation can be calculated according to the treatment of Pauls *et al.* [42] using

$$\frac{1}{T_2^{qe}} = \Delta M_2 \tau_c. \quad (5.3.2)$$

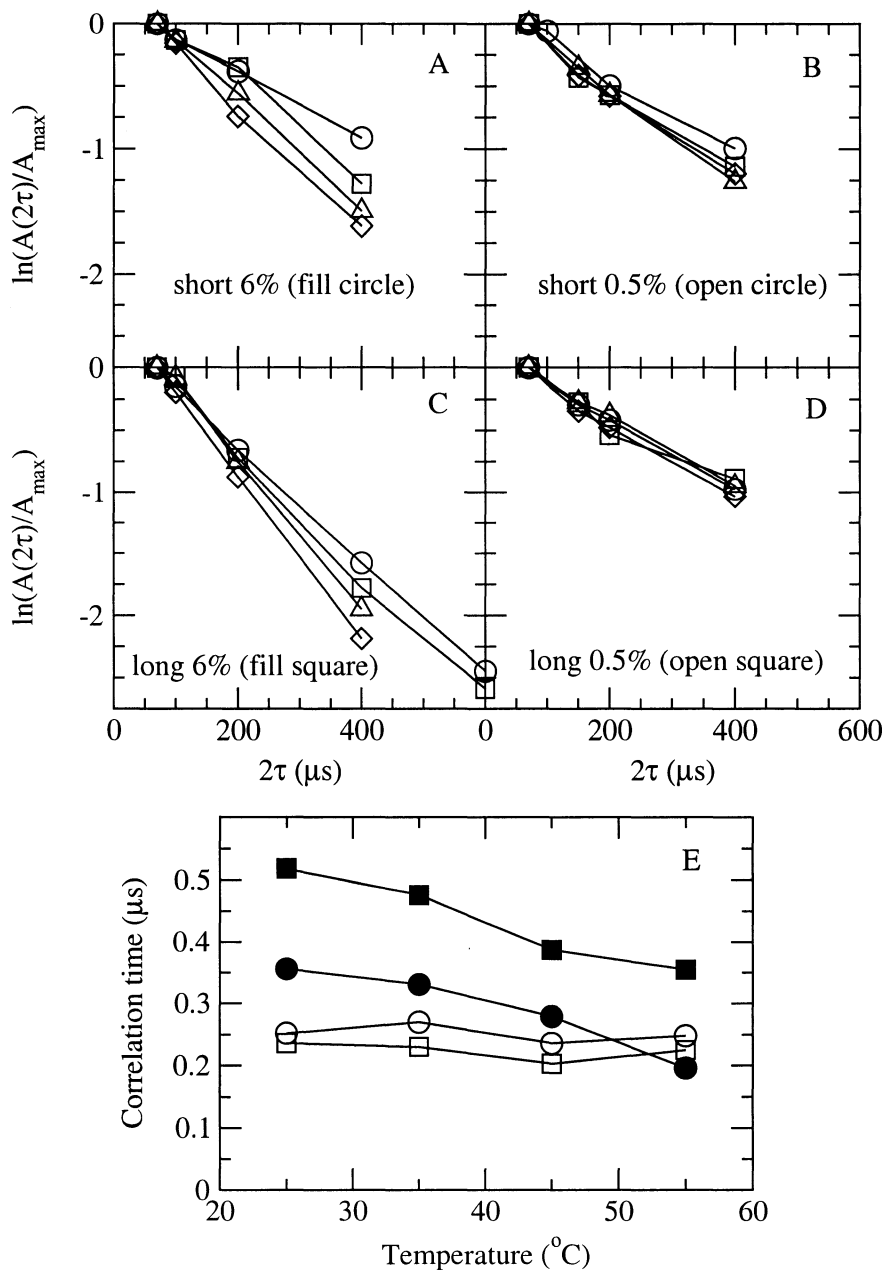


Figure 5.6: Quadrupolar echo decay times and calculated correlation times for short and long polypeptides at varying concentrations. Echo decay curves for peptides at varying concentrations are illustrated in A, B, C, and D for temperatures 25 °C (\diamond), 35 °C (\triangle), 45 °C (\square), and 55 °C (\circ). The text within each plot indicates the symbol used for plotting the correlation time graph. Correlation times plotted against temperature are presented in E for LA22 peptides at 6 mol % (\blacksquare) and 0.5 mol % (\square) and LA17 peptides at 6 mol % (\bullet) and 0.5 mol % (\circ)

and is valid if $\tau_c \ll 1/\sqrt{\Delta M_2}$. The calculation assumes that echo decay is due to reorientation of a rigid molecule about a single rotation axis. Further details of this calculation were presented in section 2.6. Figure 5.6 presents echo decays and correlation times calculated on the basis of splittings obtained from experimental spectra for both peptides at concentrations of 6 mol % and 0.5 mol %. We see from figure 5.6 that the echo decays for 6 mol % peptide concentration change with decreasing temperature which indicates that motions which modulate the echo amplitude must be affected by decreasing temperature. It is interesting to note that the echo decay measurements for the 0.5 mol % concentration of peptides change little with temperature. At 6 mol % the correlation times for reorientation are consistently longer for the longer LA22-1 peptides than for the LA17-1 peptides at the same concentration. At this concentration the correlation times for both peptides increase with decreasing temperature. At 0.5 mol % the correlation times for both peptides are approximately the same and remain relatively constant with decreasing temperature. The correlation times are within the range $2 - 5 \times 10^{-7}$ s which satisfies the above assumption since the minimum correlation time that could lead to motional narrowing is $\tau_m \approx 5 \times 10^{-4}$ s (*i.e.* $\tau_m = 1/\sqrt{\Delta M_2}$).

5.4 Discussion

The observed spectra are Pake doublets for both LA22-1 and LA17-1 peptides at concentrations of 6 mol % and 0.5 mol % at high temperatures (Figures 5.2 through 5.5). The Pake doublet spectrum reflects rapid axially symmetric motion of the peptides. The quadrupolar splitting expected for rapidly rotating deuterated alanine methyl groups on immobile polypeptides is 41.85 kHz. The observed 90° splittings

from Figures 5.2 through 5.5 are significantly less than this estimate so it is apparent that the observed spectra do not result from immobilized peptides. Additionally, since the spectra are indicative of rapid axially symmetric motion, the time scale of the motion contributing to narrowing of the spectrum must be less than the characteristic timescale for the NMR experiment (ie 10^{-6} s – 10^{-5} s).

The orientation of the methyl group bond axis is $\beta_{||} \approx 56^\circ$ with respect to the helix axis (see Figure 5.7) which is very close to the magic angle [7, 13]. If fast rotation about the helix was leading to the observed Pake doublet, then the splittings would be significantly less than in the observed spectra. If the peptide is straight and uniform, as is suggested by previous studies of α -helical peptides [19, 20], the observed inequivalence of the alanine methyl groups would imply that rotation about the helix axis is slow or absent. This result is consistent with previous studies of EGFR transmembrane segments which also show that there is no rotation about the helix axis [7]. Even if there is no rotation about the helix axis, the observed splittings do imply axially symmetric rotation about some other axis.

For an ideal α -helix there are approximately 3.6 amino acid residues per turn and a rise of approximately 1.5 Å per residue. Based on these α -helical parameters one could expect a hydrophobic length of about 33 Å for LA22-1 polypeptides. Given that the hydrophobic thickness of unperturbed POPC bilayers is approximately 26 Å, one could expect the helix axis to be tilted in the bilayer. In this case, the peptide may be tilted and reorienting about the bilayer normal. In another experiment the unique groups of splittings obtained for LA22-7 peptides deuterated at seven alanine methyl positions (see Figure 5.8) illustrate that there is an orientational inequivalence of the peptide methyl groups within the membrane interior. For this peptide there

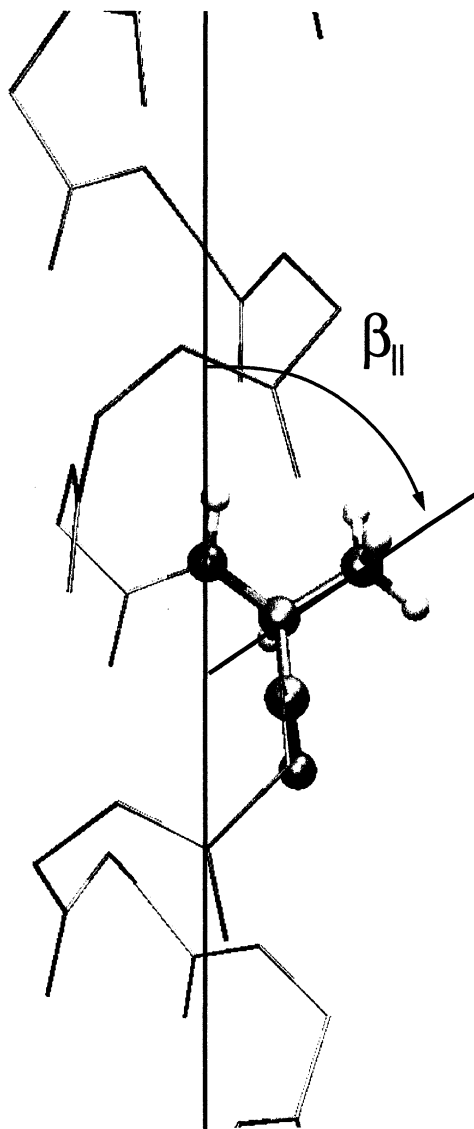


Figure 5.7: The angle $\beta_{||} \approx 56^\circ$ between the alanine methyl group bond axis and the long axis of the polypeptide.

is a group of splittings at 14 kHz, 12 kHz and around 5 kHz. The splittings are not well resolved for LA22-7 peptides but spectra obtained in that same study for LA22-2 peptides at a concentration of 0.5 mol % clearly indicate 2 quadrupolar splittings. The results illustrate that these peptides have a preferred orientation in bilayers. Similar results were obtained by Jones *et al.* [7] for deuterated methyl groups on the EGFR transmembrane domain. Those results suggested that the peptide is tilted and undergoes rapid rotation about the bilayer normal. Through geometrical analysis of the helical peptide and calculation of the deuterated alanine splittings for varying molecular tilt and rotation, Jones *et al.* [7] confirmed that EGFR transmembrane segments have a preferred tilt and azimuthal orientation about the helix axis when dispersed in POPC bilayers.

Killian *et al.* [18] suggest that WALP peptides orient strongly in a transmembrane direction. Quadrupolar splittings for WALP peptides appear to be consistent with tilted helices undergoing fast reorientation about the bilayer normal [10]. Reorientation about the bilayer normal has also been indicated for other transmembrane polypeptides [62–64]. It is important to note that reorientation about the bilayer normal is just one possible explanation for inequivalence of the alanine methyl groups. It is also possible that the inequivalence could arise from rotation of a bent helix or rotation about the axis of a helix which contains significant departures from α -helical geometry. However, previous studies have suggested that LA based peptides conform to α -helical geometry in lipid bilayers [20].

There is a significant difference between the alanine splittings of LA22-1 and LA17-1 at peptide concentrations of 6 mol % and 0.5 mol %. At 6 mol % the splitting for LA22-1 is approximately 14 kHz while the splitting for LA17-1 at 6 mol

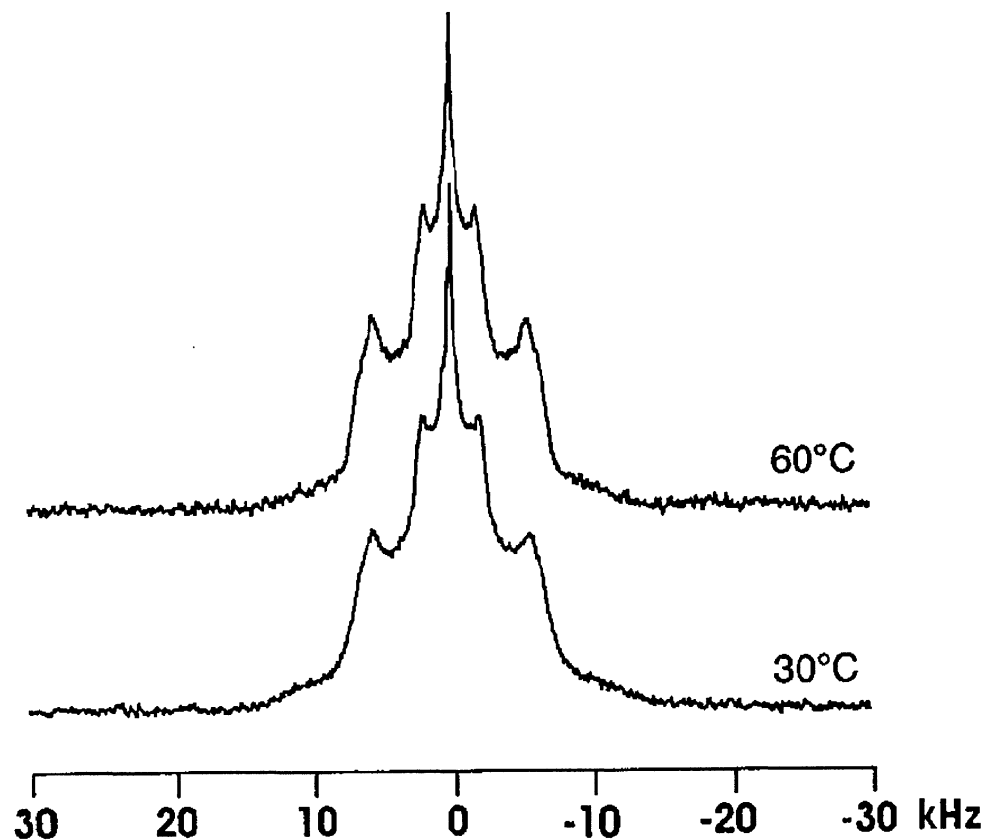


Figure 5.8: ^2H NMR spectra correspond to a concentration of 6 mol % $\text{CH}_3\text{CO-KK-(LA)}_{11}\text{-KK-CO-NH}_2$ at 60°C and 30°C in POPC bilayers and deuterated at 7 alanine methyl group positions within the transmembrane region. The distribution of splittings indicate that there is an orientational inequivalence of the alanine methyl groups. The position of the deuterated methyl group is indicated in Table 5.1.

% is approximately 7 kHz. For an ideal α -helix having 1.5 Å rise per residue we could expect a hydrophobic length of about 25.5 Å which is just long enough to span the fluid bilayer interior. This suggests that the difference between the observed splittings for long and short peptides may reflect the greater degree of tilt experienced for the longer LA22-1 peptide, although differences in orientation about the helix axis will also affect the quadrupolar splitting.

Broadening of the spectra presented in Figures 5.2 and 5.3 at lower temperatures suggest that the correlation time for reorientation about the bilayer normal increases with decreasing temperatures. Though the rate of rotational diffusion is expected to decrease with decreasing temperature and lead to broadening in the observed spectra, the spectra for peptides at 0.5 mol % suggest that the peptides still undergo rapid axially symmetric motion about the bilayer normal at 30 °C. At a concentration of 6 mol % there are only about 7-8 lipids per protein for each leaflet of the bilayer and therefore transmembrane segments probably come into contact with each other frequently. Transient contacts between the polypeptides would likely hinder rapid reorientation about the bilayer normal. These peptide-peptide interactions modulate the quadrupolar interaction over the timescale of the experiment and lead to the broadening in the observed spectra.

In the spectra for LA22-1 and LA17-1 peptide samples at a concentration of 0.5 mol% (Figures 5.4 and 5.5) the Pake doublet is readily apparent. The spectra at both temperatures are thus indicative of axially symmetric motion. It is interesting to note that when the temperature is lowered to 30 °C some broadening occurs. The degree of broadening is substantially less than that observed at high peptide concentrations. At lower concentrations the peptides are less crowded than for high concentrations so

that the peptides will come into contact less frequently than at higher concentrations. Since the contacts are less frequent we would expect less broadening at a given temperature. As was seen at higher concentrations, the broadening that occurs on cooling is greater for LA22-1 peptides than for LA17 peptides. Additionally, at lower temperatures the broadening appears to be more substantial for LA22-1 peptides. The difference between the splittings obtained for LA22-1 and LA17-1 peptides probably reflects the greater degree of tilt of LA22-1 in the lipid bilayer. The splittings and the degree of broadening with decreasing temperatures both seem to be consistent with the idea that longer tilted helices have a greater tendency to interfere than short ones.

The spectra at peptide concentrations of 6 mol % and 0.5 mol % are consistent with tilted and transiently interacting helices. However, the appearance of a broad 25 kHz feature in the spectra for samples of 0.5 mol % peptide at lower temperatures is somewhat puzzling. This feature is highlighted using arrows in Figures 5.4 and 5.5. The feature is not as apparent in spectra at 6 mol % but may be covered by the outer edges of the Pake doublet. The splitting is significantly smaller than the 41 kHz splitting which would be expected for static polypeptides. Therefore the feature must result from polypeptides whose motion is significantly hindered but fast enough to lead to averaging of the quadrupolar interaction over the experiment timescale. These observations are consistent with the existence of a population of peptides associating and rotating as long-lived dimers or oligomers. This assumption appears to be supported by the observation that the feature has a smaller amplitude as temperature is increased. That is, the peptides rotate mainly as monomers at higher temperatures. It is interesting to note that this feature is only observed for

lower concentrations of peptides. The same feature was observed by Sharpe *et al.* [13] in a ^2H NMR experiment at higher field. Though the shape of the NMR spectrum is expected to gradually change with decreasing correlation time, it is not likely that the feature is due to molecules undergoing motion with correlation times on the order of the intermediate timescale. For the intermediate timescale T_2^{qe} is expected to be short and therefore the feature would not be observable. This suggests that the feature results from molecules that are undergoing reorientation with correlation times that satisfy the short correlation time limit.

The presence of slow molecular motions leads to inefficient refocusing of the quadrupolar echo and therefore echo decay time measurements provide some insight into the timescale of the molecular motions contributing to echo decay. Semi-log plots of amplitude normalized quadrupolar echo decays are presented in Figure 5.6 for LA22-1 and LA17-1 peptides at concentrations of 6 mol % and 0.5 mol % over temperatures ranging from 25 °C to 55 °C. Fast axially symmetric motion not only determines the quadrupolar splitting observed in the Pake spectrum but also the reduction, ΔM_2 , in the spectral second moment. The reduction in second spectral moment is dependent on $\langle(3 \cos^2 \beta - 1)/2\rangle$ where β is the angle between the rotational axis of the molecule and the C-D bond. The factor $\langle(3 \cos^2 \beta - 1)/2\rangle$ is also proportional to the quadrupolar splitting. In the short correlation time limit (ie $\Delta M_2 \tau_c^2 \ll 1$), Pauls *et al.* [42] show that the correlation time for reorientation is given by

$$\tau_c = \frac{1}{\Delta M_2 T_2^{qe}}. \quad (5.4.1)$$

Their model assumes rotation of a deuterated polypeptide about a single rotational axis and does not take into account fluctuations in the orientation of methyl group

rotation axis with respect to the peptide long axis due to peptide conformational changes or fluctuations of the bilayer normal direction. Peptide conformational fluctuations are fast on the experiment timescale and contribute mainly to longitudinal or T_1 relaxation. In this model we assume that the observed echo decay is mainly due to the variations in the quadrupolar interaction that result from peptide reorientation about the bilayer normal.

The correlation times estimated from the echo decay measurements and the quadrupolar splittings obtained from the experimental ^2H NMR spectra are presented in Figure 5.6 for LA22-1 and LA17-1 peptides at both peptide concentrations of 6 mol % and 0.5 mol % as a function of temperature. At 6 mol % the correlation times for both long and short peptides decrease with increasing temperature and appear to be dependent on peptide length. At lower peptide concentrations the correlation times remain almost constant with decreasing temperature and exhibit no dependence on the peptide length. These correlation time estimates appear to be consistent with a model where the peptides are tilted in the bilayer and transiently interfere with each other. That is, at low concentrations the peptides reorient freely about the bilayer normal. Hence the spectra at 0.5 mol % exhibit axially symmetric motion over the temperature range considered. However, at a concentration of 6 mol % the peptides are relatively crowded and transiently interfere more often which leads to an increase in the correlation time for peptide reorientation about the bilayer normal. This hindered rotation is observed as broadening in the spectra as temperature is lowered for 6 mol % peptides. As temperature is decreased from 55 °C to 25 °C the spectra for LA22 peptides are more broadened than for LA17 peptides at the same concentration. In addition, the correlation times for reorientation of LA17 peptides are less

than for LA22 peptides at a concentration of 6 mol %. Spectral broadening and the correlation time estimates for peptides at 6 mol % suggest that longer tilted helices interfere more often.

5.5 Calculation of Deuteron Splittings Based on α -helical Geometry

Based on current observations it is apparent that KALP polypeptides undergo fast axially symmetric reorientation about the bilayer normal. Since slow rotation about the helix axis would give rise to a superposition of splittings the observations suggest that rotation about the long helix axis is absent. As previously stated, it seems reasonable to assume that the inequivalence of alanine methyl group quadrupolar splittings results from peptides that have a preferred orientation about the helix axis. The quadrupolar splittings obtained here for peptides with single labels along with the splittings for peptides with multiple labels reported by collaborators can be used to place constraints on peptide orientation. The peptide sequences and positions for deuterated methyl groups are presented in Table 5.1. For convenience we refer to the label positions with respect to the first leucine in the sequence which is denoted leucine 1.

For the work presented here, the quadrupolar splitting for LA22-1 peptides labeled at alanine 12 was approximately 14 kHz and is apparent from Figures 5.2 and 5.4. Based on a previous study of LA peptides carried out in collaboration with Dr. C. Grant's research group, peptides with 2 alanine methyl group labels (LA22-2, labeled at alanine 12 and alanine 14) gave splittings of ~ 14 kHz and ~ 11 kHz. In order to relate the observed splittings to peptide orientation, observed splittings were fit to a

model based on an α -helix rotating about the bilayer normal with a fixed tilt angle and orientation about the helix axis.

The model for the LA22 peptide was first constructed using Molden [65]. We assumed α -helical geometry corresponding to $\phi = -58^\circ$ and $\psi = -47^\circ$ for the backbone dihedral angles. The peptide was initially oriented with the long axis along the z direction by applying the appropriate rotations to align the principal long axis along the z direction. The long axis of the helix was determined through diagonalization of the moment of inertia tensor. The peptide was then rotated about the long axis such that the C_α - C_β methyl group bond for alanine 12 of the LA22 peptide model lay solely within the z and y plane. This gave an initial starting position for the calculation of the alanine quadrupolar splittings for all alanine methyl groups corresponding to LA22 peptides with 7 labeled positions (LA22-7, refer to Table 5.1). The splittings for the alanine methyl groups were then calculated for a range of molecular orientations according to the following steps:

- The peptide was first rotated about the long axis by the desired angle ρ as illustrated in Figure 5.9 (b). The rotation angle varied between 0° and 360° in steps of 0.5° .
- The peptide was then tilted by an angle τ (see Figure 5.9 (d)) through rotation about the x axis from 0° to 25° in steps of 0.25° . At each step the quadrupolar splitting for 7 central alanines were calculated. The peptide was assumed to rotate about the bilayer normal.

To narrow down possible orientations capable of reproducing the experimentally observed quadrupolar splittings, a search algorithm was written in MATLAB. The algorithm was written so that the splitting for alanine 12 was constrained to be 14 ± 1

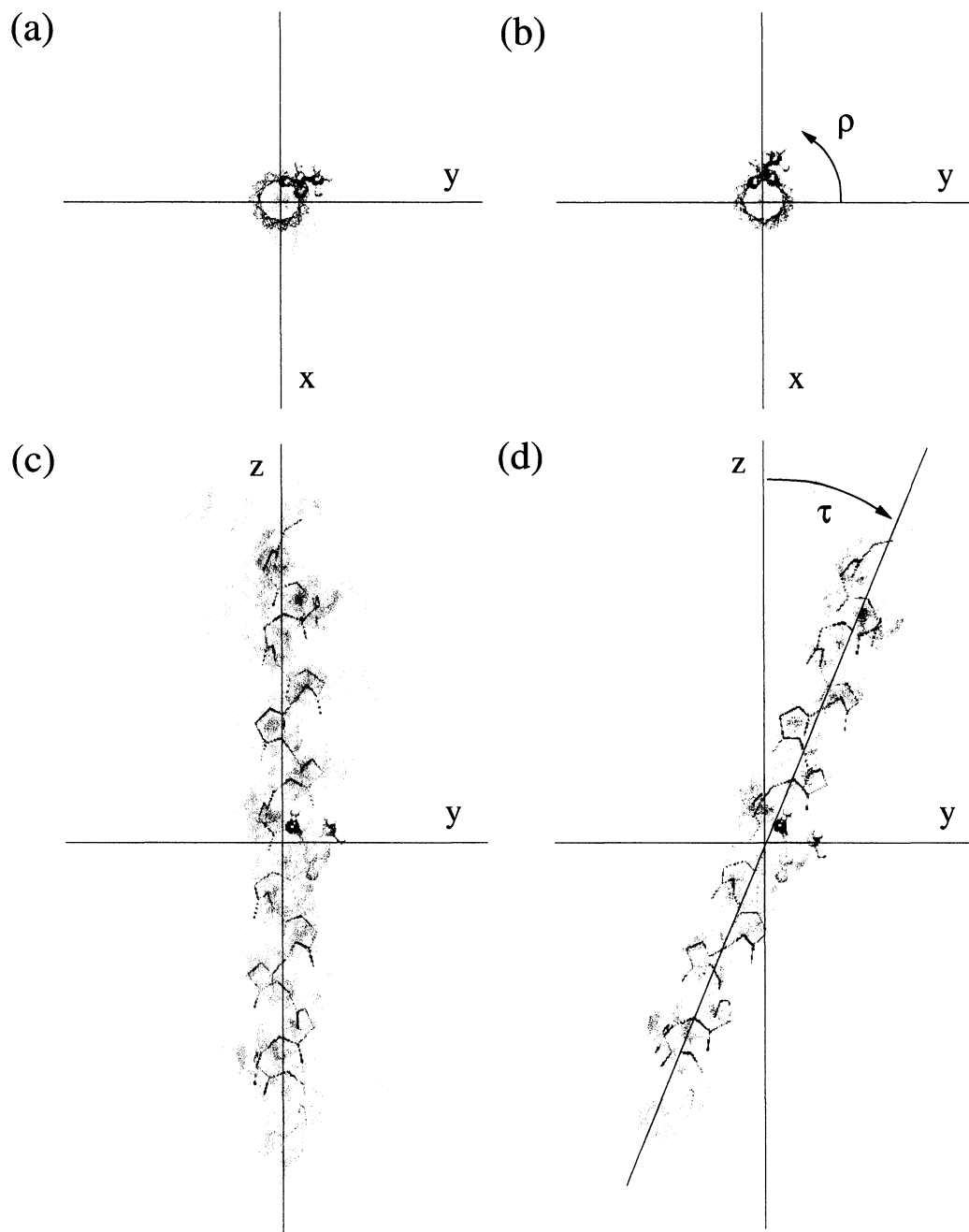


Figure 5.9: An illustration of molecular rotations involved when calculating alanine quadrupolar splittings using the constructed molecular model. The peptide backbone has been represented as lines while the remaining atoms have been represented as a cloud of van der Waals spheres. (a) Initial position: Molecular view from above (b) The peptide is rotated about the z axis by an angle ρ . (c) Molecular view from side. (d) The polypeptide is then rotated away from the z axis by an angle τ after which the splittings are calculated.

kHz and the splitting for the adjacent alanine 14 was constrained to be 12 ± 1 kHz as was observed in the experiments carried out here for single labels and the collaborative study of peptides with multiple labels (LA22-2 and LA22-7). This provided a range of splittings for varying tilt and rotation angles. Successive searching through the calculated splittings revealed that a tilt angle of $\tau = 12^\circ$ and a rotation of $\rho = 4^\circ$ gave a range of splittings which were consistent with the experimental findings for peptides with single and multiple labels *i.e.* (LA22-1, LA22-2 and LA22-7). The calculated quadrupolar splittings are presented in Table 5.2.

According to these results the splittings for the methyl groups deuterated at 7 alanine positions are consistent with a peptide that is tilted in the bilayer and undergoing rapid rotation about the bilayer normal with no rotation about the molecular symmetry axis. It is also apparent that the peptide azimuthal orientation is also an important factor leading to the unique group of splittings which may signify that the peptide sits in the bilayer with a preferred orientation instead of being kinetically trapped in arbitrary orientations due to the interaction of the peptide side chains and the surrounding lipids.

5.6 Summary

These studies have illustrated that these specific model polypeptides adopt a preferred tilt and azimuthal orientation in model membrane environments. In addition there is little to no rotation about the helix axis, a result that is supported by the magnitude of the observed quadrupolar splittings. However, fast axially symmetric rotation does occur about the bilayer normal direction. It is likely that there is some distribution of peptide orientations in the sample. This could be due to differences in bilayer

Alanine residue	Splitting (kHz)
8	5.06
10	13.41
12	11.27
14	14.94
16	11.19
18	13.33
20	4.91

Table 5.2: Splittings calculated for 7 alanine positions within the transmembrane domain at a tilt of $\tau = 12^\circ$ and a rotation angle of $\rho = 4^\circ$.

thickness throughout the sample which directly influences peptide orientation. The distribution of peptide tilt angles may also be due to fluctuations of the peptide long axis in the bilayer. Because the experiment is sensitive to an average over all peptide orientations, the “preferred” one is likely the peak of the distribution of possible orientations.

As temperature is decreased the spectra become broadened which suggests that correlation time for peptide reorientation increases. Though the rate of rotational diffusion is expected to decrease with decreasing temperature, which could lead to the observed changes in the spectra as temperature is decreased, the relatively sharp spectra obtained at 0.5 mol % peptides suggest that broadening may be induced by peptide-peptide interactions. The presence of peptide-peptide interactions seems to be supported by the observation that greater spectral broadening is observed at higher concentrations of long LA22-1 peptides.

It is interesting to note that the degree of broadening in the observed spectra is dependent on peptide length and concentration. This observation can be explained as follows. At greater concentrations there will be a greater tendency for tilted helices to interfere. There will be less interference between shorter helices since the degree of tilt in the bilayer is less than for longer peptides. The temperature dependence of correlation times at high concentrations supports this observation. That is, the correlation time for the motion must decrease in order to account for spectra which exhibit axially symmetric reorientation at higher temperatures.

It is also interesting to note that there appears to be two populations of peptides at low concentrations. The Pake doublet is due to peptides that reorient freely about the bilayer normal but also transiently interfere with other peptides. A certain fraction

of peptides are associating or forming long lived dimers based on the observation of a low amplitude feature in the spectra at a peptide concentration of 0.5 mol %. The correlation time for reorientation about the bilayer normal increases with decreasing temperature and the NMR lineshape is expected to undergo a gradual change when the correlation time reaches the intermediate time scale. The shape of the spectra would be dependent on the motional mechanism. In this intermediate timescale (*i.e.* $\tau_c \approx 1/\sqrt{\Delta M_2}$) a short T_2^{qe} is also expected. There would not likely be any contribution to the spectra from molecules undergoing motions with correlation times on the order of the intermediate time scale since T_2^{qe} is expected to be short in this motional regime. It is likely that the observed feature is due to molecules whose motion is significantly hindered but the time scale of such motions still satisfy the short correlation time limit. Natural abundance deuterons on lipids in the sample could also lead to low amplitude features in the spectra for low peptide concentrations. However, the low natural abundance of deuterons suggests that this feature is due to deuterated peptides instead of natural abundance deuterons on the POPC molecules.

Based on the present observations it appears that the specific polypeptides studied here behave in a manner similar to natural EGFR and therefore the dynamical properties of transmembrane segments of proteins may be similar. These studies suggest that transmembrane polypeptide segments adopt a preferred orientation in bilayers and they transiently interfere with each other even though these peptides do not have any special interaction motifs. Such observations may be important to the dynamics of and interactions between the transmembrane segments of natural proteins with single and multiple transmembrane regions, which in turn may be important to protein function.

Chapter 6

Molecular Dynamics Simulation of a Transmembrane Polypeptide

6.1 Introduction

In the previous chapter, ^2H NMR investigations of peptides with LA subunits were presented. The results seem to indicate that these polypeptides are tilted in the membrane environment and undergo rapid axially symmetric motion about the bilayer normal at higher temperatures. Broadening of the deuteron spectra and the temperature dependence of the calculated correlation times are consistent with transiently interfering helices. The distribution of NMR splittings presented in the previous chapter indicate that peptides not only tilt in the bilayer environment, but also have a preferred azimuthal orientation about the long helix axis.

In order to further understand some of the dynamical properties of KALP polypeptides, MD simulations have been carried out for one of the peptides investigated in the previous chapter. The MD simulations presented here provide complementary information concerning the structure and dynamics of polypeptides on a timescale that is much shorter than the ^2H NMR experiment. The initial goal of this study was to test the assumption of a uniform α -helix used during the geometrical analysis presented

in Section 5.5. In addition we wished to address issues concerning the dynamics of LA peptides in POPC bilayers and relate the MD results to the experimental findings presented in Chapter 5. In a first simulation the peptide long axis was initially aligned with the bilayer normal (z axis). This simulation allowed us to investigate the effect of hydrophobic mismatch on peptide dynamics. From this simulation we may address whether peptide orientation continually fluctuates or if the peptide eventually maintains a preferred orientation in a POPC bilayer. In a second simulation the peptide was initially tilted in the bilayer. The initial peptide orientation was chosen based on the tilt and azimuthal orientation (about the helix axis) which gave quadrupolar splittings close to the experimental values (Section 5.5). From this simulation we may observe peptide orientational changes about this preferred orientation defined by the ^2H NMR experiments. The way in which the simulated polypeptide departs from this orientation over the course of the simulation provides insight into the interactions that give rise to the adoption of a preferred orientation.

Both simulations reveal the uniform helical nature of these peptides which validates the assumptions made when analyzing the NMR data. During the simulation the peptide monomer is observed to tilt in the bilayer and it appears that reorientation about the peptide long axis is constrained.

6.2 Methods

6.2.1 Initial System Preparation

An L_α -phase POPC membrane structure was obtained from previously reported molecular dynamics results for runs at constant number, pressure, area and temperature (NPAT)[47, 66]. The bilayer was composed of 72 POPC lipids (36 in each

monolayer) and simulated at low hydration (approx. 13.5 waters per lipid). The system contained about 970 water molecules in total and the simulation cell dimensions were $48 \text{ \AA} \times 48 \text{ \AA} \times 51.58 \text{ \AA}$. In order to simulate a system at full hydration, patches of TIP3 water [67] were placed directly above and below the bilayer. The water layer thickness required for hydration was approximately 13 \AA . A spacing of 3 \AA was placed between the existing water and the patches to ensure no bad contacts between the patches of water molecules and the existing layer. An X-plor format psf file [68] of the system was built using the psfgen construction tool included with NAMMD2 MD simulation package [46]. An all-atom model was employed in accordance with the CHARMM 27 topology and parameter files [51, 69]. The final system contained 37.5 waters/lipid headgroup corresponding to a water concentration of 52 % water by weight. At this level of hydration the bilayer would be well into the liquid crystalline phase at the expected target temperature (328 K) and ambient pressure.

Simulations were carried out on an IBM RS/6000 SP1, a SGI Onyx 3400 and a Compaq Alphaserver SC40. The NAMMD2 [46] package was used for simulations while MD trajectory progress, visualization, and analysis were carried out using VMD [70] on a pentium class computer running Linux 2.4 and an SGI Onyx 3400. The system was initially simulated at 1 atm using the Nosé-Hoover Langevin piston method [58] and the system cell was allowed to fluctuate in all dimensions. This method is an extension of the Nosé-Hoover equations in which oscillations of the piston mass are dampened so that the system reaches equilibrium quickly [58]. A splitting function with a cutoff of 12 \AA was used for separation of long and short range electrostatic interactions. A cutoff of 12 \AA was also employed for calculating van der Waals interactions and a switching function was used to relax the van der Waals potential

to zero over a distance of 2 Å. Periodic boundary conditions were employed in all cell dimensions and the Particle Mesh Ewald (PME) method [56] was used for full evaluation of electrostatic interactions. Typically 8 processors were used during MD simulations. The SHAKE algorithm [53] was used to constrain all bonds between hydrogens and heavy atoms with a tolerance of 10^{-5} Å. The physical gaps between the original and added water layers disappeared after 50 ps of simulation. The system was then cooled and then was subjected to 13000 steps of conjugate gradient minimization with a tolerance of 0.0005.

The equilibration process was then initiated at 1 atm using the Nosé-Hoover Langevin piston method at a temperature of 328 °K. The simulation ran for a total of 600 ps after which a variety of system properties were measured to ensure that the system was equilibrated. Finite size effects are expected to be small in this simulation despite the small system size and the use of periodic boundary conditions since system cutoffs have been chosen to lay within the system cell. In this way atoms do not interact with atom “images” due to periodic boundaries, but instead only interact with atoms inside the system cell.

6.2.2 Polypeptide Construction

The polypeptide chosen for the simulations, $\text{CH}_3\text{CO-KK-(LA)}_{11}\text{-KK-CO-NH}_2$, is expected to be α -helical in the membrane environment and its initial conformation was chosen based on previous experiments of LA based polypeptides. Observations reported by Zhang *et al.* [19, 20] confirm α -helical geometry for a twelve subunit LA segment embedded in a bilayer membrane. The helical peptide used in the simulation was constructed using MOLGEN [65]. All side chain dihedral angles were chosen from the backbone dependent rotamer library for proteins [71]. After construction,

the polypeptide was subjected to 3500 steps of conjugate gradient energy minimization. Minimization of the protein conformational energy was completed in four stages similar to those described by Belohorcov *et al.* [72]:

1. In the first 500 steps, dihedrals were restrained using a restraint potential with energy constant of 50 kcal/mol. The C_α positions of the alanine residues and the C_α and C_β positions of the leucine and lysine residues were initially held fixed.
2. In the next 500 steps, dihedrals were restrained using a restraint potential with energy constant of 25 kcal/mol. The C_α positions of the alanine residues and the C_α and C_β positions of the leucine and lysine residues were harmonically restrained with a force constant of $25 \text{ kcal mol}^{-1} \text{ \AA}^{-2}$.
3. In the next 500 steps, dihedrals were restrained using a restraint potential with energy constant of 5 kcal/mol. The C_α positions of the alanine residues and the C_α and C_β positions of the leucine and lysine residues were harmonically restrained with a force constant of $5 \text{ kcal mol}^{-1} \text{ \AA}^{-2}$.
4. Over the final 2000 steps of the protein minimization procedure, there were no restraints on side chain dihedrals nor harmonic restraints on atomic positions.

These measures were used to ensure that the peptide remained α -helical during energy minimization. The polypeptide was then aligned with its long axis oriented along the z direction by diagonalization of the moment of inertia tensor followed by application of appropriate coordinate transformations.

6.2.3 Lipid-Peptide System Construction and Preparation

Following equilibration, 4 lipid molecules were removed from the upper and lower leaflets of the bilayer. The system was then coupled to a weak repulsive cylindrical potential which forced lipids outward to allow the bilayer to accommodate the polypeptide. Two lipid-peptide simulations were subsequently constructed from the prepared lipid bilayer. The first simulated system was constructed with the polypeptide long helix axis oriented along the z direction (bilayer normal). Although this initial configuration is expected to lead to a longer equilibration time than for a starting configuration where the peptide is tilted at some angle, setting the peptide at this initial orientation allows for characterization of helix tilt due to hydrophobic mismatch. This simulation could provide us with information about peptide dynamics when a certain degree of hydrophobic mismatch is present. Choosing an initial orientation for the peptide with the long axis oriented in the z direction could reveal if the peptide would eventually maintain a preferred tilt and azimuthal orientation in a POPC bilayer as was observed from the ^2H NMR study presented in Chapter 5. The second simulated system was constructed with the peptide initially oriented according to the tilt and orientation about the helix axis which gave the best agreement with the quadrupolar splittings presented in Chapter 5 (see Section 5.5). From this simulation we can observe changes in peptide orientation about this initial orientation which was defined based on the ^2H NMR experiments. The simulation parameters for both systems were as described above.

The PME technique requires that the periodic cell charge be zero. To counteract the 4 charged lysine side chains, Cl^- ions were added to the system by randomly removing 2 water molecules from the upper and lower water layers [73]. The helix

was initially constrained while the cylindrical potential was relaxed.

During equilibration the lipid-peptide system was simulated at 328 K and 1 atm pressure using the Nosé-Hoover Langevin piston method. Simulations may also be carried out at constant surface tension if one is concerned with properties of the membrane relevant to longer length scales. Such properties include bilayer undulations and peristaltic motions [74]. Since this study is not concerned with these long length scale properties, an NPT ensemble is appropriate for this investigation. Bond lengths between pairs containing hydrogen were constrained using the SHAKE algorithm. Typically 8-16 processors were used for the calculations. The total time for the simulation with the peptide initially placed along the z axis was 8.5 ns including equilibration and dynamics. The duration of the simulation where the peptide was placed in the bilayer with an initial orientation defined by NMR measurement was approximately 10 ns.

6.3 Results and Discussion

6.3.1 Bilayer Equilibration and Dynamics

A good indication of progress toward equilibrium of the bilayer is given by the root mean displacement (RMSD) of molecular coordinates with respect to the starting configuration. This quantity is given by

$$RMSD = \frac{1}{N} \sum_{i=1}^N (\vec{r}_{in} - \vec{r}_{i0})^2 \quad (6.3.1)$$

where the vectors \vec{r}_{in} and \vec{r}_{i0} describe positions of atom i and their difference is the displacement of atom i from its position at the beginning of the simulation. The calculation is carried out by summing the displacements for each time step. In this

case a molecule can effectively move an arbitrarily large distance from the initial molecular coordinates.

The evolution of RMSD over the initial 600 ps bilayer equilibration is shown in Figure 6.1. It increases sharply during the first 100 ps. This initial change in the RMSD reflects the approach to equilibrium for short timescale motions such as angle bending and torsional motions. After 300-400 ps there is very little change in RMSD, indicating that the short timescale motions have reached a stable equilibrium. Subsequent changes in RMSD reflect minor alterations to bond lengths, lipid headgroup and chain dihedrals, lateral displacement of the lipid molecules and fluctuations in simulation cell dimensions. The RMSD will continue to increase slowly and mainly reflects the lateral diffusion of molecules in the bilayer. An equilibration period of about 600 ps is consistent with the suggestion, by Shinoda *et al.* [75], that gauche transition rates for torsional motion of the lipid acyl chains may provide some indication of equilibration time needed in MD simulations of pure lipid bilayers. This time may be as short as 10 ps for carbons in the acyl chains and as long as 400-700 ps for torsions at the base of the lipid headgroup. The parameters describing the POPC bilayer following the equilibration period are consistent with previous simulations of POPC in the liquid crystalline phase [76, 77].

Figure 6.2 illustrates the area per lipid headgroup during the equilibration run. The area/lipid headgroup slowly increases over the 600 ps period as lipids redistribute and the simulation cell fluctuates under the influence of applied external pressure. The average area per lipid headgroup during the equilibration is approximately 63 \AA^2 . This is similar to area per lipid obtained in previous simulations of POPC in the liquid crystalline phase [77]. For comparison, Nagle and Tristram-Nagle [78],

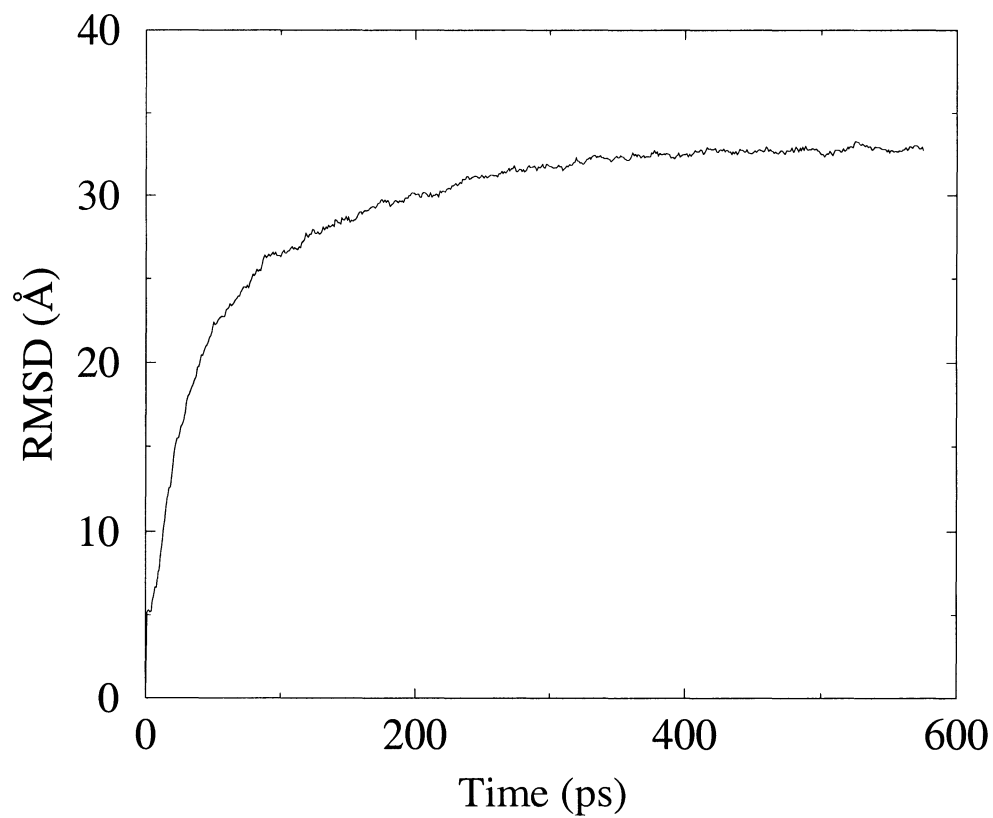


Figure 6.1: Bilayer root mean square displacement (RMSD) during a 600 ps equilibration run. The RMSD rises sharply during the first 100 ps of the equilibration run, indicating large fluctuations in the non-equilibrium state of the system. After 400 ps the RMSD remains almost constant, indicating a near equilibrium configuration.

taking into account the effect of fluctuations, obtain average areas/lipid in the liquid crystalline phase of 64 \AA^2 for DPPC at $50 \text{ }^\circ\text{C}$ and 72.5 \AA^2 for DOPC at $30 \text{ }^\circ\text{C}$.

The state of a bilayer is also reflected by the orientational order parameters of the lipid acyl chain methylene segments. Experimentally, such order parameters can be obtained from ^2H NMR quadrupolar splittings of deuterium labeled segments. The orientational order parameter is then defined as

$$S_{CD} = \left\langle \frac{3 \cos^2 \theta - 1}{2} \right\rangle$$

where θ is the angle between the CD bond and the bilayer normal and the average is over motions of the chain. Lipid acyl chain order parameter profiles which would be obtained from the simulation results by substituting deuterons for oleoyl and palmitoyl hydrogens respectively are presented in Figures 6.3 and 6.4. Results are shown for the bilayer with and without the peptide inserted. Order parameters in the absence of the peptide appear to be in good agreement with results of Seelig and Waespe-Sarcevic [79]. Lipid acyl chain order parameter profiles typically exhibit a sharp decrease toward the chain ends indicating a large degree of mobility near the bilayer center. The experimentally-observed dip in order parameter near the oleoyl double bond was successfully reproduced by the simulations.

The bilayer thickness is also useful for comparison with and validation of simulation results. Figure 6.5 shows that for peptide-free POPC bilayers at $55 \text{ }^\circ\text{C}$, the average distance between phosphates on opposite sides of the bilayer fluctuated slightly about 39.5 \AA over the course of the simulation. For DOPC in the liquid crystalline phase, Weiner and White (1992) found the average separation between phosphates and the bilayer centre to be 20.2 \AA . For lipids with PC headgroups, the peaks in the electron density profile coincide approximately with the average phosphate location.

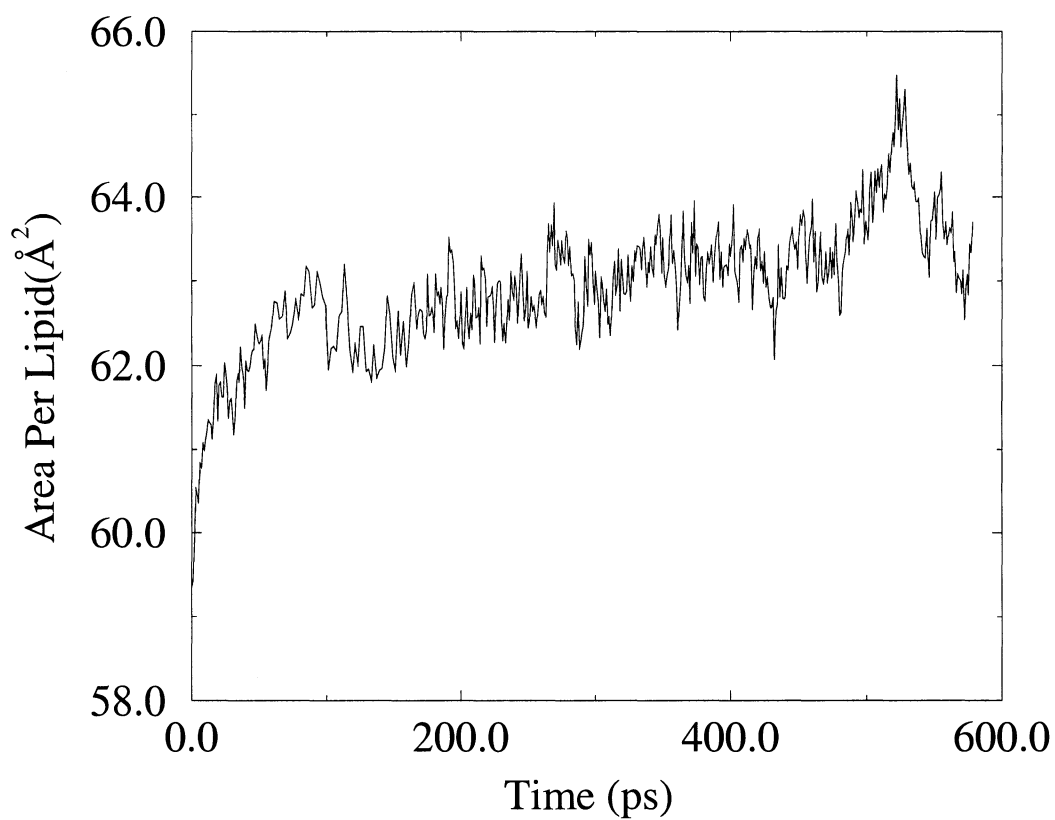


Figure 6.2: Evolution of area per phosphatidylcholine headgroup during the equilibration run. The area per lipid initially increases as the cell dimensions fluctuate due to the influence of applied external pressure. After 200 ps the headgroup area fluctuates slightly about 63 Å²

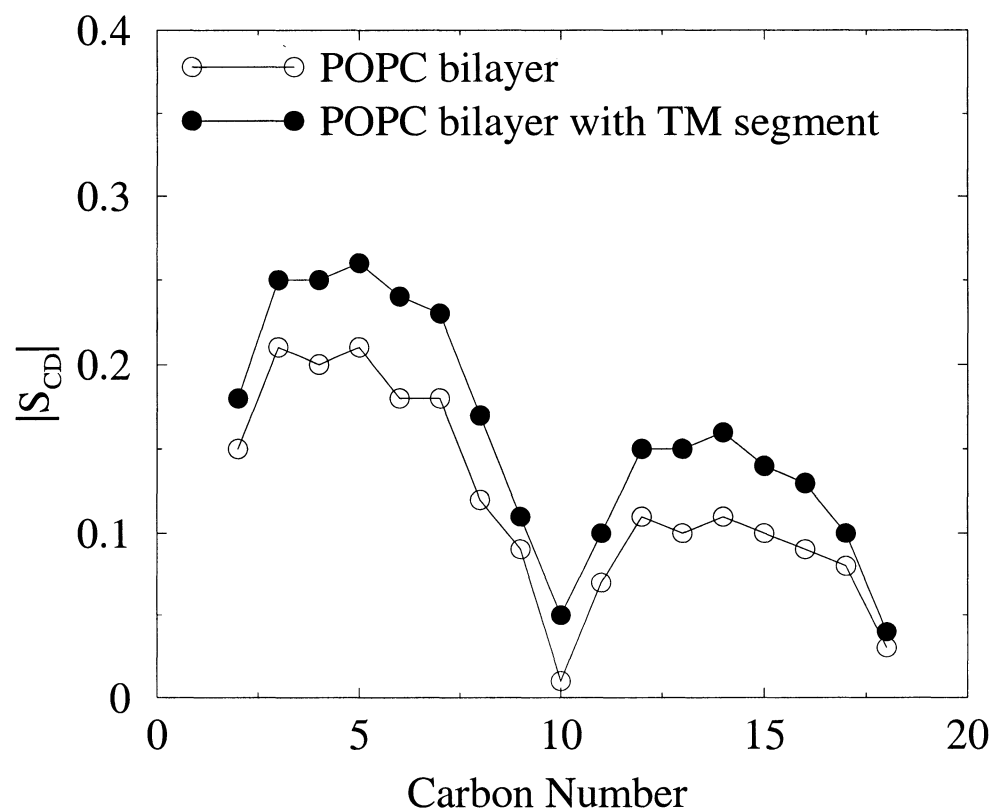


Figure 6.3: Unsaturated chain deuterium order parameter profile for POPC with and without the transmembrane peptide present. The dip about the center of the profile reflects the position of the double bond in the oleoyl acyl chain. The decrease in order parameter towards the chain end is indicative of the degree of mobility of the acyl chains further within the bilayer interior.

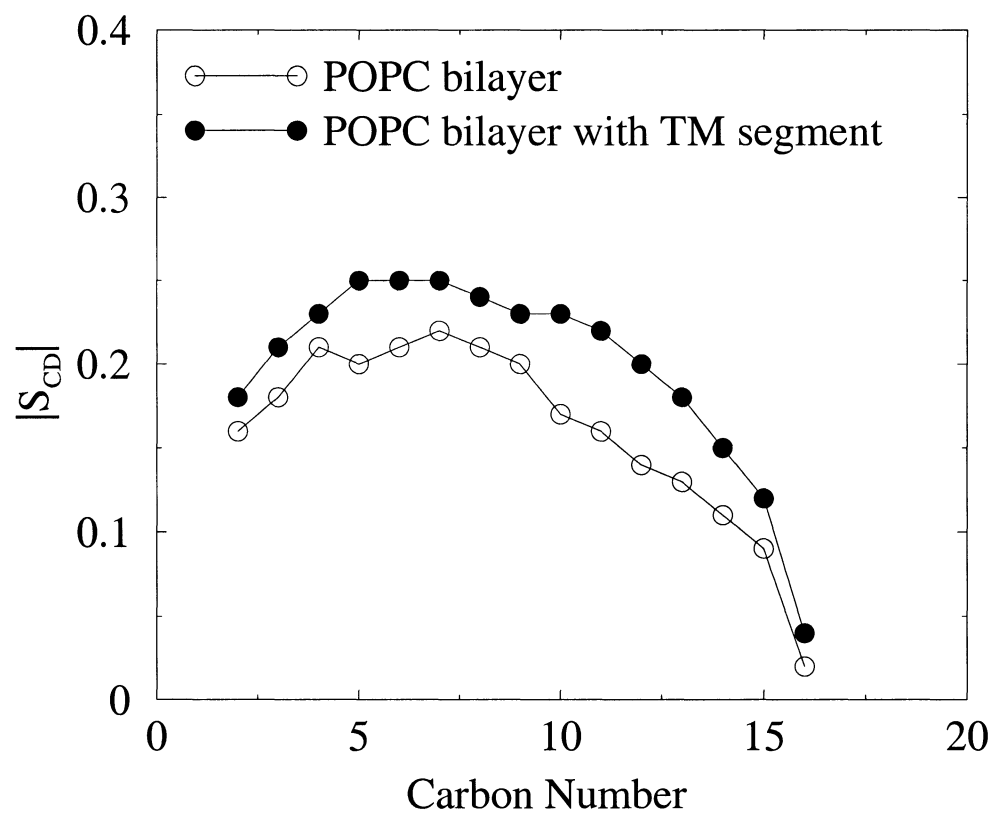


Figure 6.4: Saturated chain deuterium order parameter profile for POPC with and without the transmembrane peptide present.

Nagle and Tristram-Nagle [78] report headgroup peak-peak distances in liquid crystalline phase of 38.3 Å for DPPC at 50 °C and 36.9 Å for DOPC at 30 °C. These comparisons suggest that the simulation generates a reasonable bilayer thickness for peptide-free POPC bilayers in the liquid crystalline phase.

For the simulation where the peptide was initially aligned along the z axis, addition of the transmembrane peptide segment induces a small change in bilayer order. Figures 6.3 and 6.4 show that the orientational order parameters of both POPC chains increase slightly in the presence of the polypeptide. This is consistent with the results of previous experimental and simulation studies of bilayers containing helical polypeptides [21, 72]. Figure 6.5 shows that bilayer thickness increases slightly over the course of the simulation. This observation may be a transient response to the addition of the peptide or indicative of a peptide-induced enhancement of bilayer thickness with fluctuations on a timescale longer than the simulation duration. The duration of the simulation is not sufficient to make a precise conclusion about the cause of fluctuations in bilayer thickness. Similar results were obtained for the simulation with the peptide initially tilted in the bilayer.

Overall, comparison of simulated bilayer properties with experimental observations and the results of previous simulations provides some confidence that the environment of the polypeptide is appropriately modeled.

6.3.2 Protein Structure and Dynamics

If interactions among transmembrane polypeptide segments are relevant to transmembrane receptor function, then the initiation of such events will likely be sensitive to the way in which the transmembrane segments of diffusing proteins encounter each other. This behaviour will reflect the orientation and dynamics of such segments on isolated

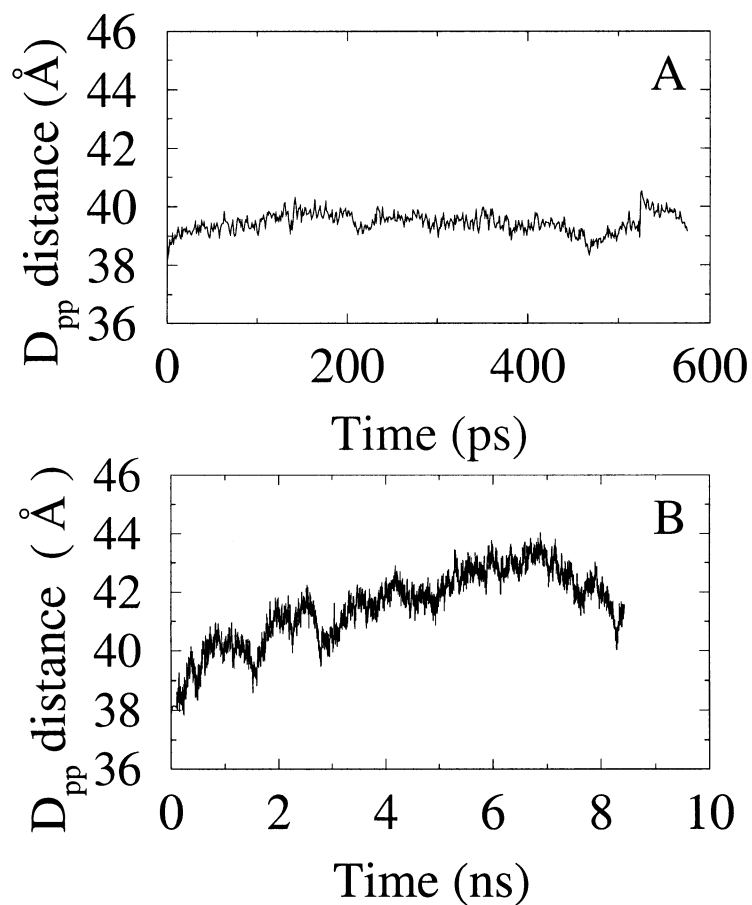


Figure 6.5: (A) Separation between average positions of phosphorus atoms on opposing sides of the bilayer during the 600 ps equilibration run. Initially the phosphorus-phosphorus transmembrane separation increases sharply, after which it fluctuates about 39.5 \AA . (B) Phosphorus-phosphorus transmembrane separation versus time after addition of the transmembrane segment for the simulation where the peptide is initially oriented along the z axis.

proteins in the membrane. If the interaction is non-specific, the relationship between the tilt of isolated protein transmembrane segments and the preferred crossing angle between interacting segments may be relevant. If the interaction involves a more specific interaction between particular motif sequences on the interacting transmembrane segments, then the extent to which orientation or motions make such sequences accessible to one another may also be significant. We are thus interested in the tilt of the peptide, the possibility that the peptide adopts a preferred orientation about its helix axis and, if there is a preferred orientation, the amplitude of motions that might allow the peptide to sample a range of orientations about the preferred one. These issues have been addressed using information extracted from the time series of isolated α -helical peptide coordinates generated by the simulation.

Transmembrane Segment Structure

Figure 6.6 shows the average peptide dihedral angles over the course of the simulation where the peptide is initially oriented along the z axis in the form of a Ramachandran plot. Figure 6.7 illustrates the ϕ and ψ dihedral angles, averaged over the course of the molecular dynamics trajectory, as a function of residue position, excluding the terminal lysines, along the helix backbone of the transmembrane segment. The overall average dihedral angles for the peptide during this simulation are $\phi = -42.17^\circ$ and $\psi = -63.58^\circ$ which is within the α -helical range. The Ramachandran plot is slightly scattered indicating some local deformations to the α -helix backbone. Similar results were obtained for the second simulation. In fact, the average dihedral angles for the peptide in the second simulation (peptide initially oriented according to NMR measurement) were calculated to be $\phi = -43.45^\circ$ and $\psi = -63.14^\circ$ which is also within the α -helical range. Overall, the helix in each simulation is stable over the

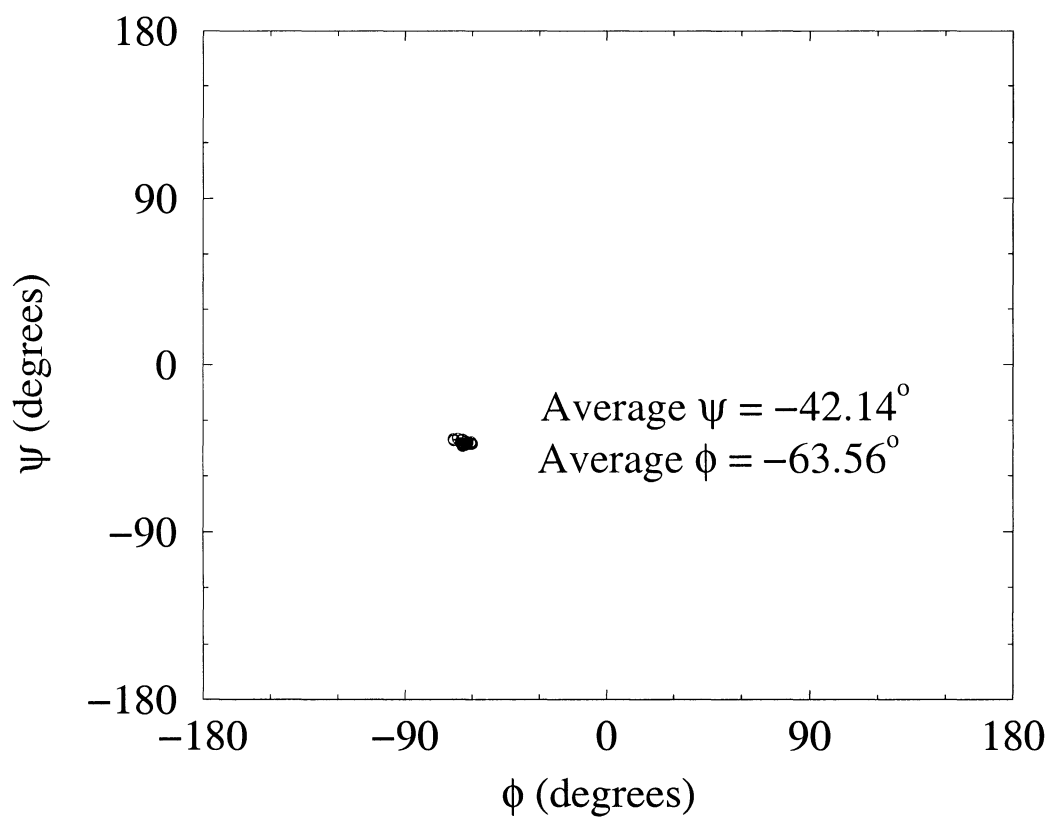


Figure 6.6: Ramachandran plot of the ϕ and ψ dihedral angles for the polypeptide during the simulation were the peptide was initially aligned along the z axis.

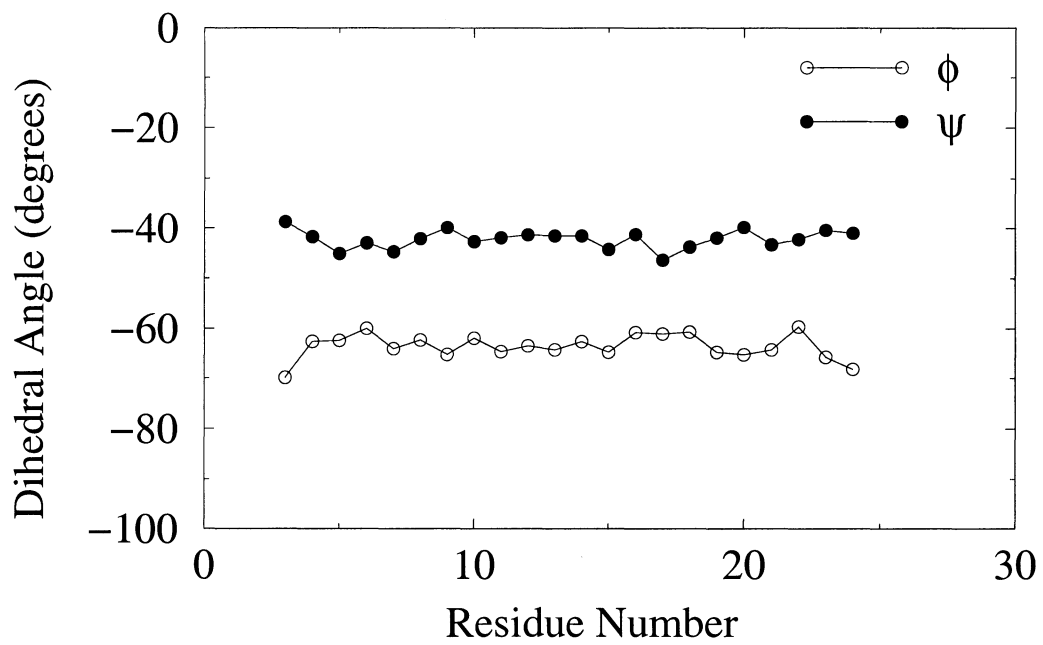


Figure 6.7: Dihedral angles along the helix backbone of the polypeptide for the simulation were the peptide was initially aligned along the z axis.

course of the MD trajectories and no significant unraveling occurs toward the ends of the helix backbone. The peptide structural data presented here are consistent with FTIR results reported by Zhang *et al.* [19] which indicate that proteins composed of twelve LA subunits retain α -helical conformation when incorporated in bilayers of phosphatidylcholines with varying chain lengths.

Transmembrane Segment Dynamics

Figures 6.8 and 6.9 show the evolution of the helix long axis orientation with respect to the bilayer normal during both simulations. During the first simulation the peptide long axis is initially restrained along the z axis and the peptide restraints are lifted at approximately 100 ps on this graph. After this the helix begins to tilt in order to accommodate the hydrophobic length of the transmembrane segment which is greater than the hydrophobic thickness of the bilayer interior. After an initial period of rapid reorientation, the tilt of the helix axis continues to fluctuate slowly over the next 8.5 ns. For the next simulation, where the peptide was initially tilted in the bilayer, the peptide restraints are lifted at approximately 1.5 ns. This is apparent from Figure 6.9 which illustrates that the peptide tilt is approximately 14° during this interval. As discussed previously, this value for the initial helix tilt was chosen based the average orientation obtained from ^2H NMR experiments on the same peptide. After 1.5 ns the helix further tilts into the bilayer but fluctuations in helix tilt appear to be slower than for the peptide during the previous simulation. In fact, for the second simulation peptide tilt remains relatively constant over durations of at least 1.5 ns. This may indicate that the initial orientation of the peptide is relatively more stable than the simulation where the peptide is initially aligned along the z axis.

Figures 6.8 and 6.9 also show the angles between the alanine methyl axes and

the bilayer normal for alanines at positions 12 and 14 along the polypeptide for both simulations. For an ideal α -helix having 3.6 residues per turn, one would expect the projections of two C-CH₃ bond axes (on two alanines separated by a single leucine) onto a plane perpendicular to the helix axis to be separated by approximately 160°. This angle can be obtained for a pair of alanines from the simulation data by rotating the methyl axes into the principal axis system of the moment of inertia tensor for the helical peptide and then projecting each C-CH₃ bond direction onto the plane perpendicular to the peptide z axis. Over the course of the first simulation (peptide initially aligned along z axis), the average separation of the projections of the alanine-12 and alanine-14 methyl axes is approximately 159°. The correlation between the orientations of the two alanine methyl axes with respect to the bilayer normal shown in Figures 6.8 and 6.9 for both simulations reflects this fixed geometric relationship between the two alanine sidegroups. Figure 6.8 also suggests some correlation between the helix axis orientation and the orientation of each methyl axis with respect to the bilayer normal. For the second simulation (peptide initially tilted in the bilayer), slow variations in the orientations of the two alanine methyl axes with respect to the bilayer normal also accompany slow fluctuations in helix tilt. For the first simulation (peptide initially aligned along z axis), it appears that an increase in angular displacement of the helix axis leads to an increase in angular displacement of the C-CH₃ bond axis for the alanine at position 12 on the polypeptide. Depending on the direction of helix tilt and the initial orientation of the alanine C-CH₃ bond, this behaviour might be expected even if there were no rotation about the helix axis. Interestingly, the C-CH₃ bond on the next alanine, at position 14, displays orientational fluctuations in the opposite direction. An increase in angular displacement of the helix axis from

the bilayer normal leads to a decrease in angular displacement of the C-CH₃ bond axis from the bilayer normal for the alanine at position 14 of the polypeptide. This difference in response to changes in helix tilt reflects a rotation about the helix long axis that is found to accompany changes in helix axis orientation with respect to the bilayer normal. Reversibility of this effect is demonstrated by the observation that as the helix tilts back toward the bilayer normal, the helix rotates about its long axis in the opposite direction. In the simulation where the peptide is initially tilted in the bilayer, it appears that changes in rotation about the helix axis also accompanies variations in helix tilt but the variations appear to be more gradual over the simulation timescale when compared with the simulation where the peptide is initially aligned along the z axis.

The methyl axis orientations plotted in panels B and C of Figures 6.8 and 6.9 reflect differences between the long and short timescale motions of the helix about its long axis. At short times, relative to the time resolution of the simulation, the helix orientation about its long axis fluctuates with an amplitude of 5°-8°. These fluctuations are on same timescale as that of the helix axis tilt. This observation suggests that for a given tilt of the helix axis, there is a preferred average orientation of the helix about that axis. Fluctuations about that preferred amplitude are rapid but constrained in amplitude.

The preferred orientation about the peptide long axis may be more apparent in Figure 6.10 which illustrates the helix tilt and corresponding helix axis azimuthal orientation for both simulations. The azimuthal orientation of the helix axis was measured in several steps. First by taking the cross product of vectors along the z axis and the helix long axis provided a resultant vector which could be used as a

reference. Next, a vector along the methyl group axis of alanine 14 was projected onto a plane perpendicular to the helix long axis. The dot product of this vector with the reference vector was used to define the azimuthal orientation. It is clear from Figure 6.10 (peptide initially oriented along z axis) that as the peptide tilts there is a corresponding rotation about the helix axis. It is interesting to note that the rotation about helix axis is constrained. That is, the peptide could possibly rotate 360° but instead undergoes small angular fluctuations on short timescales. This supports ^2H NMR observations which indicate that LA peptides adopt a preferred tilt and azimuthal orientation when incorporated in lipid bilayers [7, 13, 18]. However, for the next simulation (peptide initially tilted in the bilayer) the azimuthal orientation of the peptide changes only slightly over the course of the simulation. This may be largely in part due to the initial orientation of the lysine side-chains which may be in a more well defined position at the bilayer surface since the peptide orientation was chosen based on the NMR experiments. The lysine charged end residues may play an important role in determining peptide orientation in bilayers [17] by constraining rotation about the helix axis. Though rotation about the helix axis appears to be constrained, peptide tilt appears to vary substantially over the course of the simulation and may be due to the flexibility of the lysine sidechains. This is a particularly interesting result since small fluctuations about the helix axis and in helix tilt could modulate the contact between the transmembrane segments of natural proteins involved in physiological processes such as signal transduction.

6.3.3 Comparison with ^2H NMR Experiments

Structural and orientational information obtained from the MD simulations can be used to generate ^2H NMR quadrupolar splittings for alanine methyl groups. By

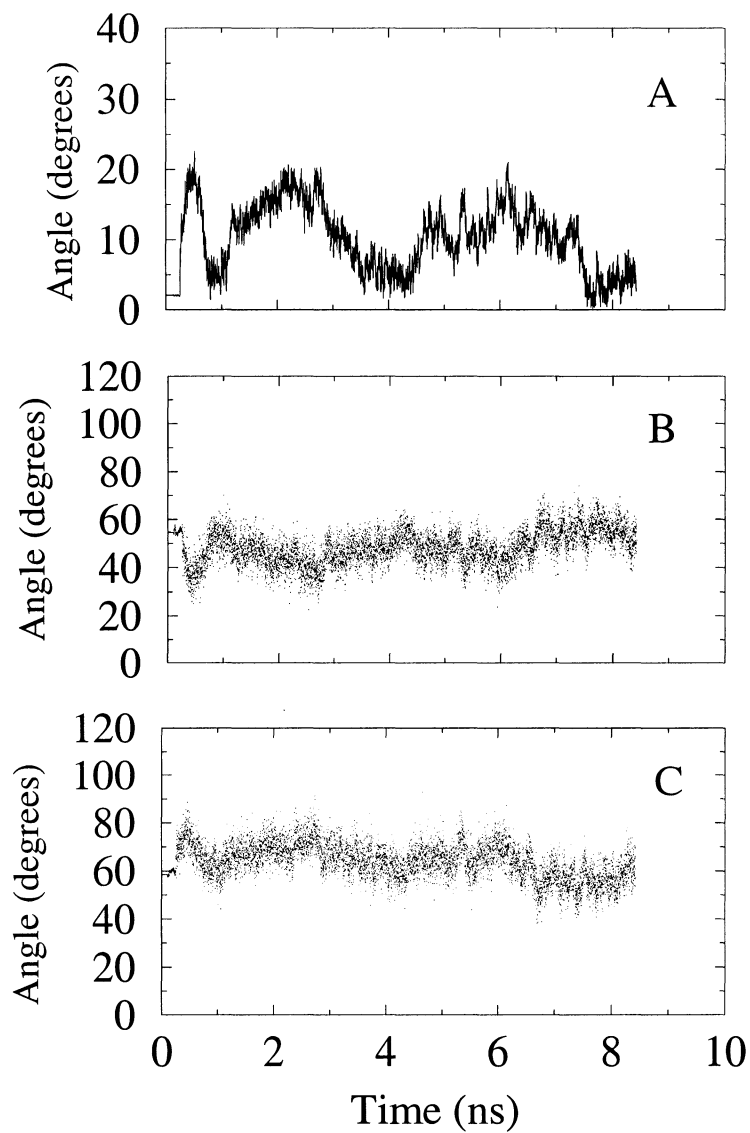


Figure 6.8: Various angular orientations for the polypeptide calculated during the simulation. (A) peptide tilt, (B), (C) projection of the C_{α} - C_{β} methyl group bonds for alanine number 12 and 14 respectively during the simulation where the peptide was initially oriented along the z axis. Initially the peptide was constrained for approximately 300 ps. This is apparent from the graph above.

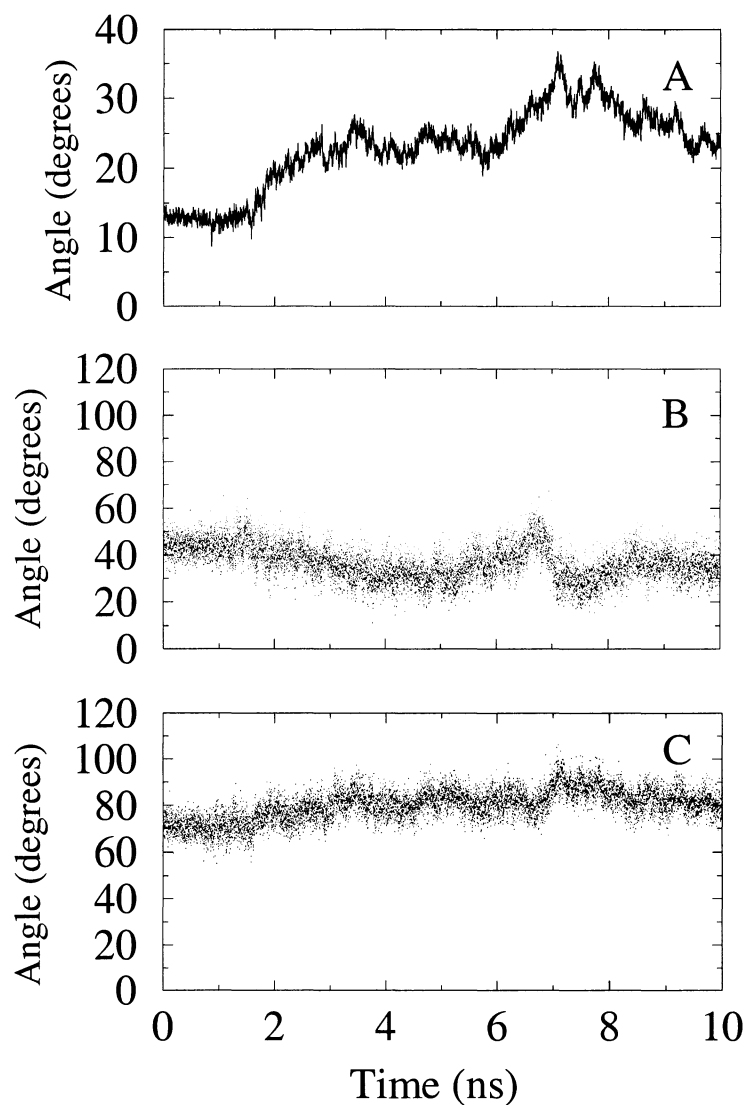


Figure 6.9: Various angular orientations for the polypeptide calculated during the simulation. (A) peptide tilt, (B), (C) projection of the C_{α} - C_{β} methyl group bonds for alanine number 12 and 14 respectively during the simulation where the peptide was initially tilted in the bilayer. Initially the peptide was constrained for approximately 300 ps. The various angular orientations during this time are not include in the plots.

making certain assumptions about reorientation of the whole peptide over the longer timescales (10^{-5} s), characteristic of the quadrupolar echo experiment, we can compare calculated splittings to spectra that have been observed experimentally for seven deuterated alanine methyl groups on this peptide [13]. Assuming axially symmetric C-D bonds, the ^2H NMR spectrum for a deuteron on a static, rigid molecule is a doublet with prominent edges separated by

$$\Delta\nu_Q = \frac{3}{2} \frac{e^2 Q q}{h} \left(\frac{3 \cos^2 \theta - 1}{2} \right) \quad (6.3.2)$$

where θ is the angle between the CD bond and the applied magnetic field. If the molecule undergoes axially symmetric reorientation with a correlation time that is short with respect to the 10^{-5} s timescale characteristic of the ^2H NMR experiment, the splitting is reduced by an additional factor of $\left\langle \frac{3 \cos^2 \beta - 1}{2} \right\rangle$. In this case β is the angle between the CD bond and the rotational axis of the molecule and the average is over any motions of the molecule to which the deuteron is attached. In this case, the angle θ is then redefined as the angle between the applied magnetic field and the axis about which the molecule reorients. For the deuterated methyl groups on labeled alanine residues, fast rotation of the methyl group about the symmetry axis of the $\text{C}_\alpha\text{-C}_\beta$ bond introduces an additional factor of $\frac{1}{3}$. Then β can then be redefined as the angle between the methyl group symmetry axis and the axis about which the molecule is reorienting. As illustrated in the previous chapter, the spectrum for labeled alanine methyl groups on peptides incorporated into multilamellar vesicle bilayers is a superposition of doublets corresponding to a spherical distribution. For peptides which undergo rapid axially symmetric motion, the spectrum has prominent edges (90° edges) corresponding to molecules reorienting about axes perpendicular to the applied field. The prominent 90° edges for a methyl-deuterated alanine on a

transmembrane polypeptide segment are separated by

$$\Delta\nu_Q = \frac{1}{4} \frac{e^2 Qq}{h} \left\langle \frac{3 \cos^2 \beta - 1}{2} \right\rangle \quad (6.3.3)$$

where β is now the angle between the alanine methyl group symmetry axis and the axis about which the peptide is reorienting. The simulation presented here provides a picture of peptide reorientation on a timescale which is much shorter than the NMR experiment. Quadrupole echo decay measurements presented in the previous chapter suggest that the quadrupole splittings for labeled-alanine deuterons on transmembrane peptides also reflect additional averaging of the quadrupole interaction by reorientation of the peptide about a symmetry axis with a correlation time about 25 times longer than the duration of the simulation presented here.

To compare the results of this simulation with observed quadrupolar splittings for the transmembrane polypeptides with repeated LA subunits [13], we have calculated alanine deuteron quadrupole splittings for two axes about which axially symmetric peptide reorientation may presumably occur. One of these is the symmetry axis of the helix itself. We refer to this model as *circum*-helix. In this case, β in Equation 6.3.3 represents the angle between the C-CH₃ bond axis and the long axis of the transmembrane segment and the average is over the simulation trajectory. It may also be the case that the peptide helix axis is tilted and is undergoing rapid reorientation about the bilayer normal and the reorientation of the peptide about the helix axis remains in the neighbourhood of values found during the simulation. We refer to this model as *circum*-normal. In this case β is the angle between the bilayer normal and the C-CH₃ bond axis.

Tables 6.1 and 6.2 present the calculated ²H NMR quadrupolar splittings obtained for seven alanine residues by averaging over the simulation trajectories (separately

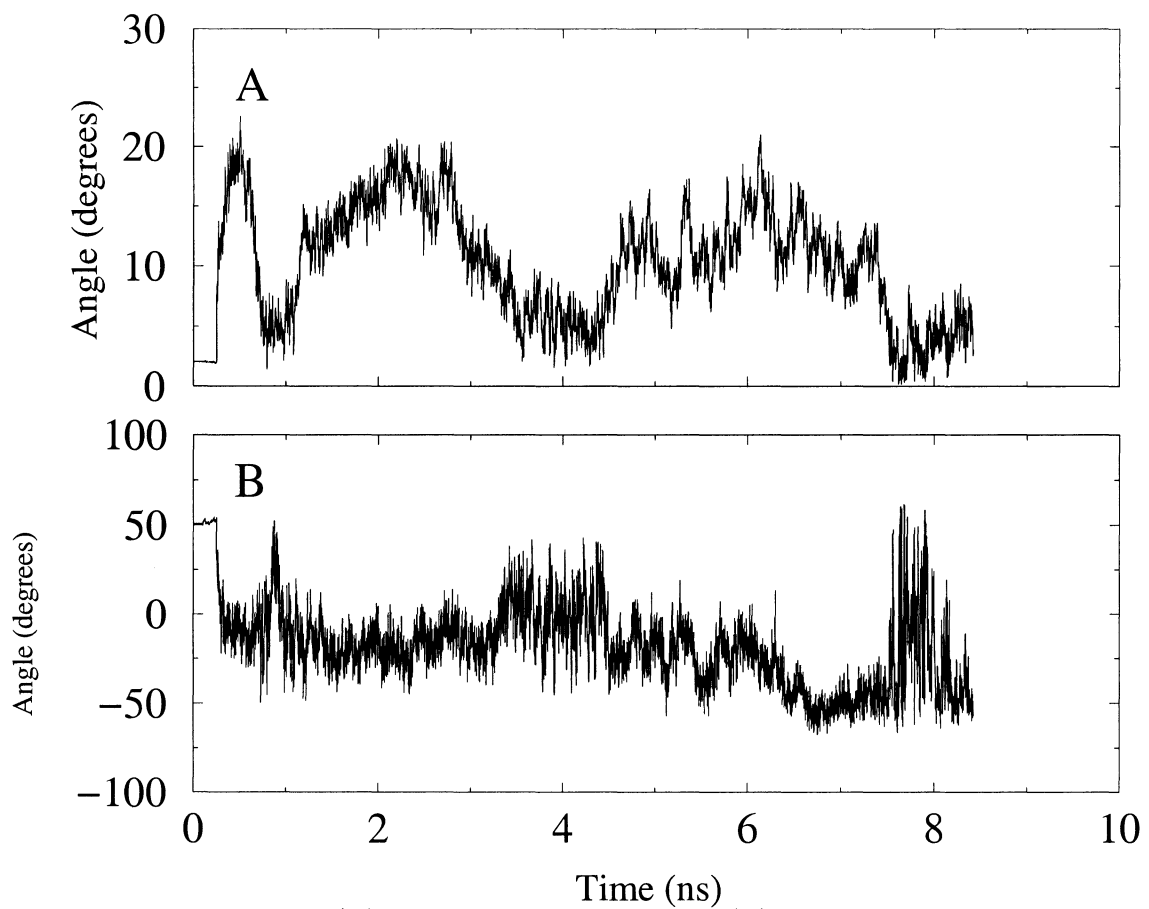


Figure 6.10: Peptide tilt (A) and azimuthal orientation (B) during the simulation with the peptide initially aligned along the z axis.

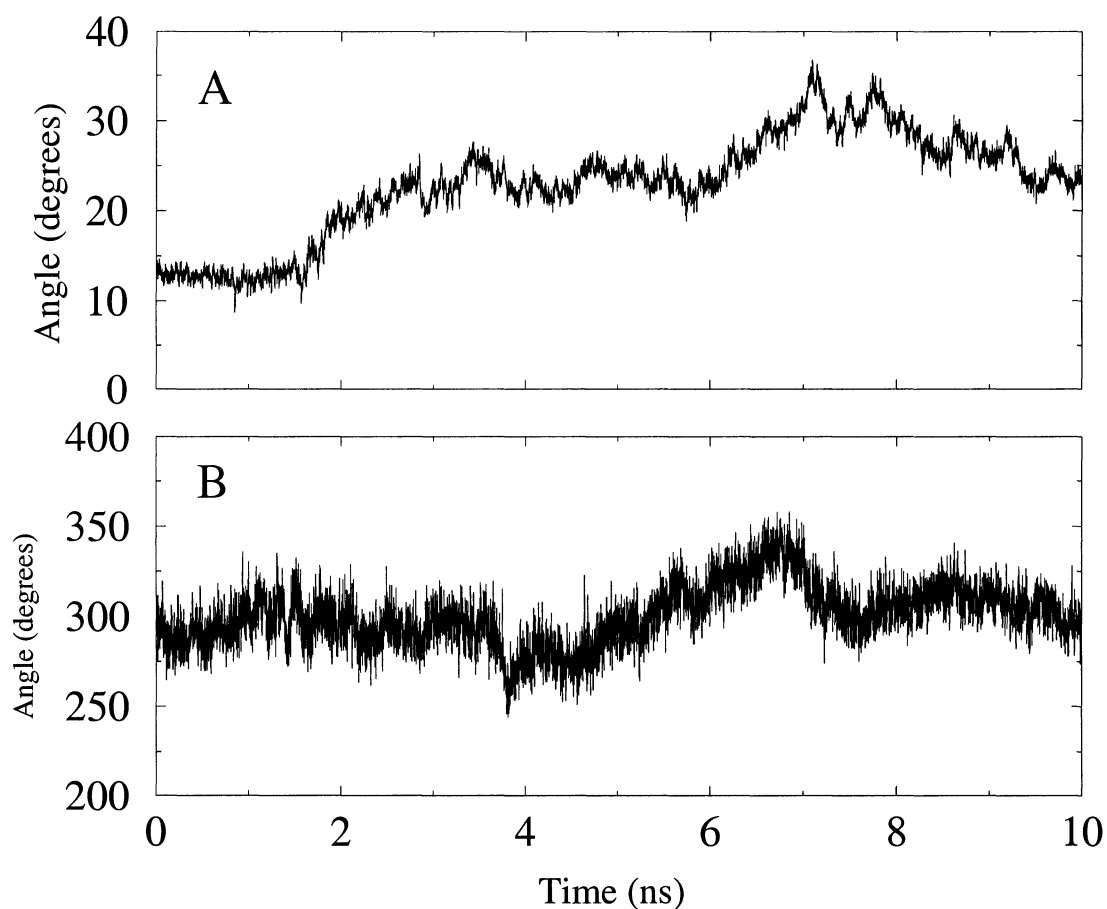


Figure 6.11: Peptide tilt (A) and azimuthal orientation (B) during the simulation with the peptide initially tilted in the bilayer.

for both simulations) and interpreting the results in terms of each of the two models described above for longer-time-scale axial peptide reorientation. The experimentally determined splittings for methyl deuterons on these alanine residues are found to fall into two ranges: 4-5 kHz and 11-14 kHz with the splittings for residues 14 and 16 being 14 kHz and 11 kHz respectively [13]. The experimental observations illustrate the inequivalence of quadrupole splittings for different positions along the peptide backbone. Additionally, the overall size of the observed splittings are more consistent with the *circum*-normal model. While the calculated splittings display inequivalence for both models of peptide reorientation, the results obtained by assuming reorientation about the helix axis (*circum*-helix model) cover a significantly smaller range and are, on average, smaller. For an ideal α -helix, the orientation of the C-CH₃ bond axis with respect to the molecular long axis is expected to be approximately 56°. This is very close to the magic angle (54.7°) so that averaging of the quadrupole interaction by rapid reorientation about the helix axis will result in quadrupolar splittings being close to zero. The angle between the C-CH₃ bond axis and the peptide long axis calculated for each alanine residue varies between 54° and 59° in the simulation. The spread in splittings calculated for these positions assuming reorientation about the helix axis (*circum*-helix model) reflects fluctuations about ideal α -helical geometry. Some inequivalence is apparent from the calculations. However, the *circum*-helix model does not provide the range and consistently larger splittings observed in the experimental spectra. The results for both simulations indicate that although deviations from α -helical geometry lead to a distribution in splittings, these alone may not be sufficient to lead to the splittings observed in the experiment.

For both simulations, the splittings obtained by assuming rotation of the tilted

helix about the bilayer normal (the *circum*-normal model) are larger, on average, than those obtained by assuming rotation about the helix axis. However, when the peptide is initially oriented along the z axis, the calculated splittings for the *circum*-normal model are, on average, smaller than the experimentally observed splittings. When the peptide is initially tilted in the bilayer, the calculated splittings for the *circum*-normal model are typically larger than the experimentally observed splittings. The larger splittings obtained for the *circum*-normal model during the second simulation (peptide initially tilted in the bilayer) reflect the greater tilt of the peptide long axis from the bilayer normal as is apparent from Figure 6.9. Figure 6.12 illustrates the instantaneous splitting calculated for alanine 12 and 14 (simulation with peptide initially oriented along z axis) assuming rotation of a tilted peptide about the bilayer normal. It is apparent that the instantaneous splitting is very sensitive to peptide orientation during the simulation and therefore leads to a large distribution of calculated splittings. This is reflected in the calculated standard deviations for the splittings presented in Tables 6.1 and 6.2.

The splittings obtained for both simulations capture aspects of the alanine methyl group inequivalence observed experimentally but do not correctly reproduce the distribution of observed splittings. The maximum alanine deuteron splitting obtainable by assuming rotation of the tilted helix about the bilayer normal for the peptide is constrained by the peptide tilt [13]. Another possibility for smaller splittings obtained in the first simulation (peptide initially oriented along z axis) is that the simulation has not been long enough to permit structural alterations, such as partial relaxation of the helix near the bilayer surface, which might simultaneously allow the lysines to interact with the bilayer surface while making possible a larger helix tilt angle and

possibly a different orientation of the peptide about the helix axis. This particular effect has been referred to by several authors as “snorkelling” [22]. Figures 6.13 and 6.14 illustrate the z positions of the lysine C_α carbons (atoms are along the helix backbone) and the nitrogen atoms attached to the ends of the lysine side-chains for both simulations. These figures also illustrate the time variation of the average z position of the phosphorus atoms in the upper and lower bilayer leaflets. We see from Figure 6.13 that the z positions of the lysine C_α carbons are usually within the bilayer interior during each simulation which is consistent with the helix backbone maintaining a position within the bilayer hydrophobic interior. Some evidence for “snorkelling” is apparent when the previous plot is compared against Figure 6.14 which illustrates that the lysine side-chain nitrogens maintain a position in the bilayer which closely tracks the average phosphorus position. Table 6.3 presents the relative position of the lysine side-chain nitrogens with respect to the lysine C_α carbons for the upper and lower leaflets of the bilayer. Based on these calculations it seems that the position of the lysine terminal nitrogen typically extends beyond the z position of the C_α carbons. We should keep in mind that time variation of z position of the phosphorus atoms is an average over atoms and therefore does not show local deformation of the bilayer due to the presence of the peptide. Though the lysine nitrogen positions appear to extend beyond the bilayer phosphorus boundary in some instances, the ends of the lysine side chains probably interact directly with local lipid phosphate groups.

While the larger splittings obtained for the *circum*-normal model (rapid rotation about the bilayer normal) do not entirely reproduce the observed splittings, the values obtained from the *circum*-helix model represent the upper limit obtainable by assuming rapid rotation of the simulated peptide about the helix axis and are thus clearly

Residue Number	$ \Delta\nu_Q $ (kHz) <i>circum-helix</i>	$ \Delta\nu_Q $ (kHz) <i>circum-normal</i>
8	2.69±5.74	5.98±6.68
10	1.75±5.28	9.16±5.54
12	0.61±5.09	6.94 ±7.45
14	3.42±4.74	8.34±6.30
16	0.51±4.72	3.30±7.39
18	3.35±5.11	4.15±7.46
20	0.16 ±5.12	2.79±6.85

Table 6.1: Absolute value of the calculated ^2H NMR splittings for the polypeptide in the simulation with the peptide initially aligned along the z axis. Splittings are calculated for two possible orientational models. The *circum-helix* model assumes that the peptide rotates rapidly about the long helix axis while the *circum-normal* model assumes rapid rotation of a rigid peptide about the bilayer normal. The uncertainty associated with each calculated value is the standard deviation of the splitting during the simulation.

Residue Number	$ \Delta\nu_Q $ (kHz) <i>circum-helix</i>	$ \Delta\nu_Q $ (kHz) <i>circum-normal</i>
8	2.19±6.15	6.67±8.19
10	5.38±4.72	15.94±3.75
12	1.16±5.01	18.86±7.52
14	3.74±4.33	18.22±2.80
16	0.29±4.51	22.88±7.11
18	2.35±4.36	17.39±3.57
20	1.36±5.15	14.86±9.48

Table 6.2: Absolute value of the calculated ^2H NMR splittings for the polypeptide in the simulation with the peptide initially tilted in the bilayer. Splittings are calculated for two possible orientational models. The *circum-helix* model assumes that the peptide rotates rapidly about the long helix axis while the *circum-normal* model assumes rapid rotation of a rigid peptide about the bilayer normal. The uncertainty associated with each calculated value is the standard deviation of the splitting during the simulation.

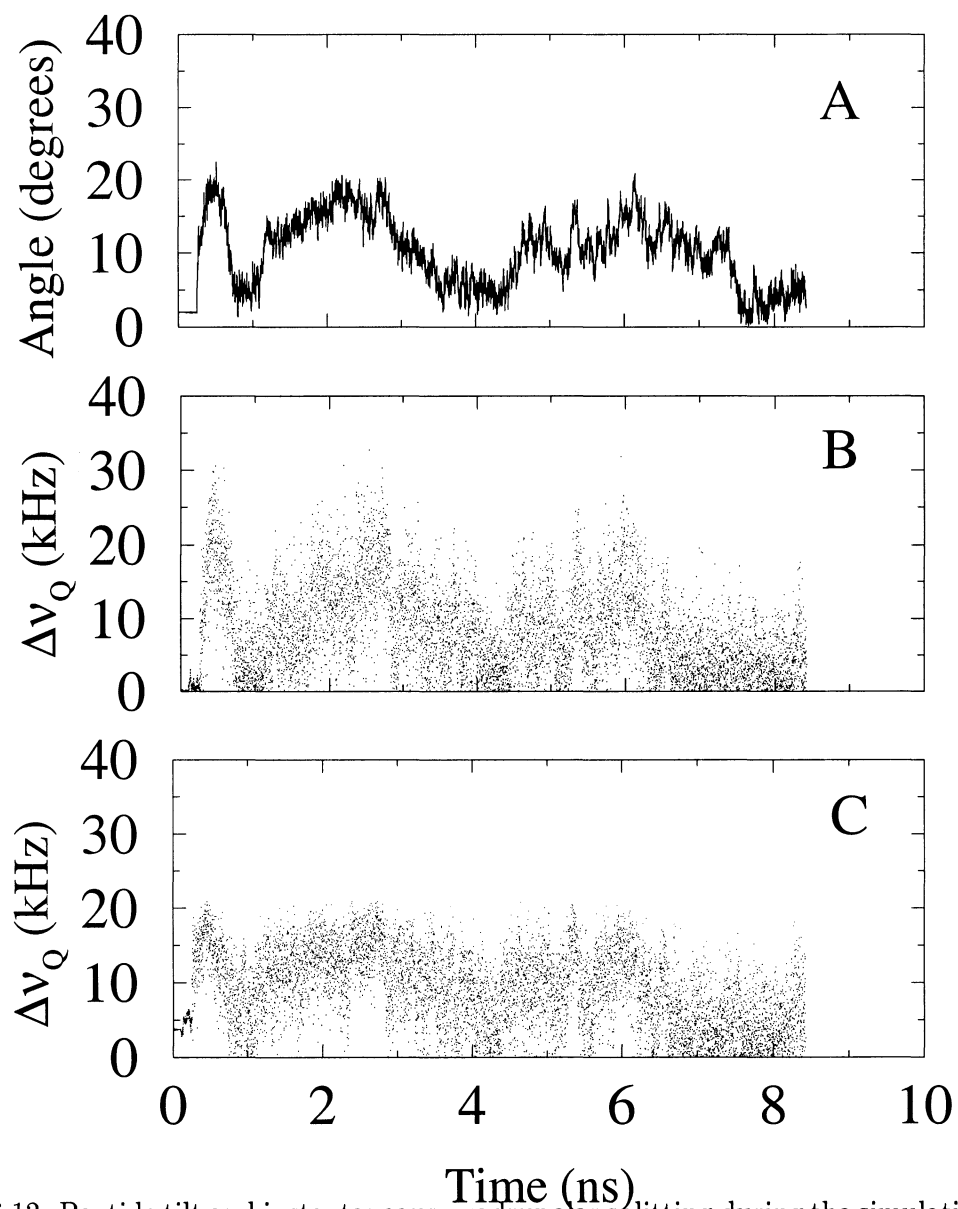


Figure 6.12: Peptide tilt and instantaneous quadrupolar splitting during the simulation with the peptide initially aligned along the z axis. The panels illustrate (A) peptide tilt, while (B) and (C) illustrate the instantaneous quadrupolar splittings for methyl groups attached to alanine number 12 and 14 respectively.

inconsistent with observation. This supports the concept that the peptide adopts a preferred orientation in the bilayer [7, 13]. While the timescales of the simulations are limited, the simulation results also suggest that the preferred orientation is likely to persist over the longer timescales characteristic of the deuterium NMR experiments and of the rotational correlation time inferred from quadrupole echo decay measurements. Figure 6.8 shows that fluctuations in the average angles between the residue 12 and residue 14 alanine methyl axes and the bilayer normal are correlated with fluctuations in the tilt angle of the helix and thus possibly driven by changes in helix tilt. However, studies of WALP and KALP peptides indicate that the orientation of such peptides in bilayers is also determined by the arrangement of flanking end residues around the helix axis. The orientation of the peptide may then be due to the interaction of the charged lysine end residues with the negatively charged lipid phosphate groups which anchor the peptide to the bilayer. The average value of the helix tilt is also expected to be constrained by the need to accommodate the span of hydrophobic helix residues within the bilayer interior.

Receptor function has been suggested to involve ligand-induced association of receptor proteins (Yarden and Schlessinger, 1987), and interactions between the transmembrane segments of such proteins may involve contact between portions of the helix surface having particular amino acid sequences or motifs [62, 80, 81]. The specific effect of the valine-to-glutamic-acid mutation on structure and association of the neu/ErbB-2 transmembrane domain has been the subject of molecular dynamics studies with the peptide in vacuum [82–85] and in a bilayer environment [86]. The present results, based on 8.5 ns of simulation trajectory for a transmembrane polypeptide with repeated LA subunits, complement deuterium NMR observations

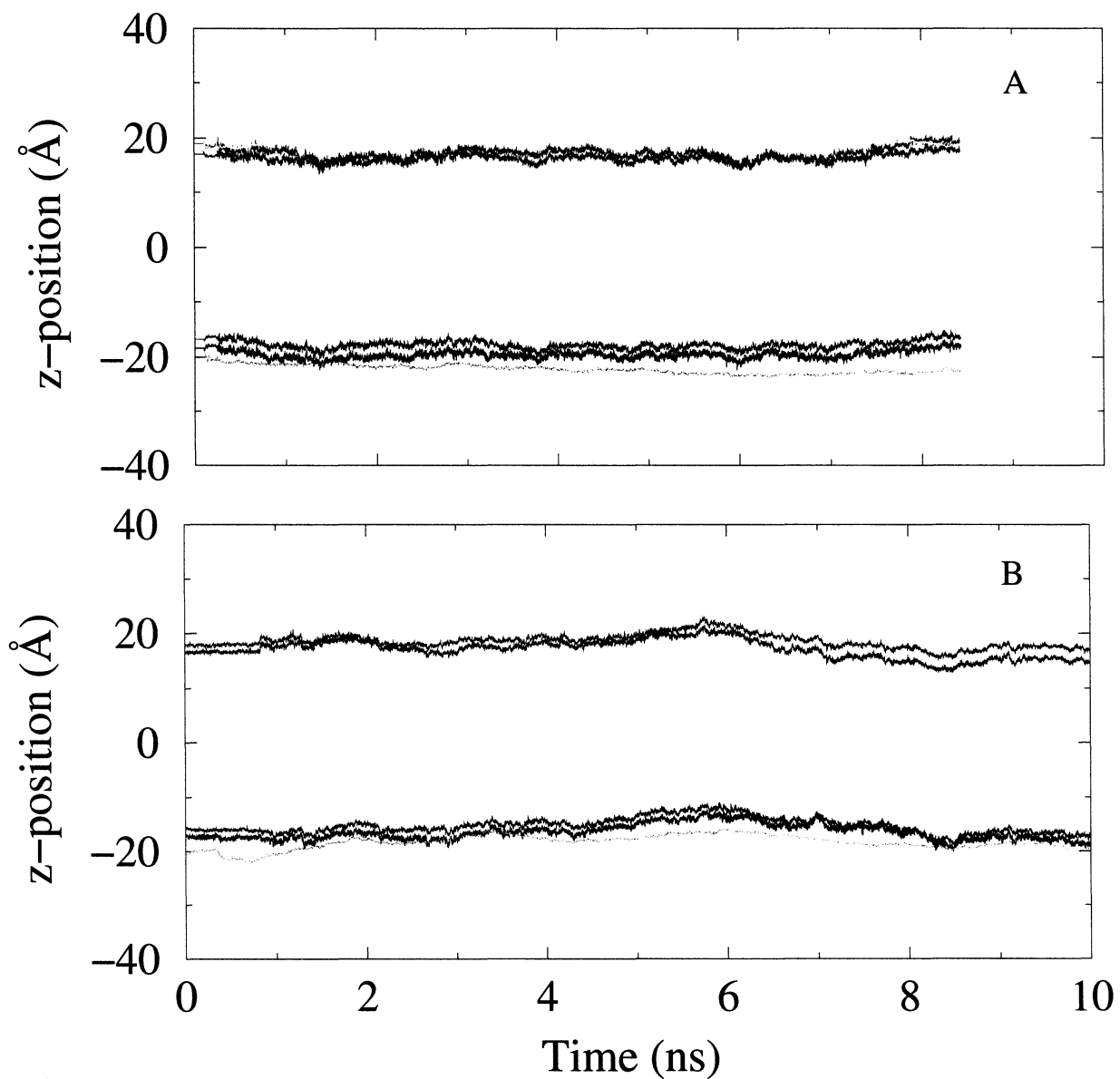


Figure 6.13: Z position of the lysine C_{α} carbon atoms and the average z position of the lipid phosphorus atoms during the simulation with the peptide initially aligned along the z axis (A) and the simulation with the peptide initially tilted in the bilayer (B). Atomic z positions of lysine C_{α} carbon atoms in upper bilayer leaflet are represented by blue and green lines while lysine C_{α} carbon atoms in the lower bilayer leaflet are represented by red and black lines. The average z position of the lipid phosphorus atoms in the upper and lower bilayer leaflets are represented by yellow and brown lines respectively

of related peptides [13]. Together the results indicate that this peptide is tilted in a bilayer environment and adopts a preferred average orientation for specific residue side groups with respect to the bilayer normal. The persistence of such an orientation in the apparent absence of specific interactions within the hydrophobic bilayer interior may indicate a sensitivity of peptide axial orientation to interactions near the bilayer surface. This may be relevant to the functioning of some receptor tyrosine kinases if tilting of transmembrane domains is present. If interactions between peptides are stabilized by interactions between specific motifs or regions of the helix surfaces, the accessibility of those surface regions on tilted peptides may depend on the orientation adopted by those segments and might thus be modulated by interactions which change the average azimuthal orientation about the helix long axis.

6.4 Summary

The results presented here illustrate the uniform helical nature of a transmembrane polypeptide studied in the previous chapter. During the simulations the peptide remains α -helical which validates one of the assumptions during the NMR analysis.

The simulations revealed some of the dynamical characteristics of polypeptides on a short timescale. Both simulations showed that rotation about the helix axis was constrained over the course of the simulation but can undergo small amplitude angular fluctuations on short time-scales. This particular result is consistent with the NMR data which suggests that peptides do not rotate about the long helix axis. Though helix azimuthal angle appears to vary slightly during the simulations, the helix tilt appears to vary substantially. This may be due to the charged lysines which interact electrostatically with the polar bilayer surface. The lysines effectively

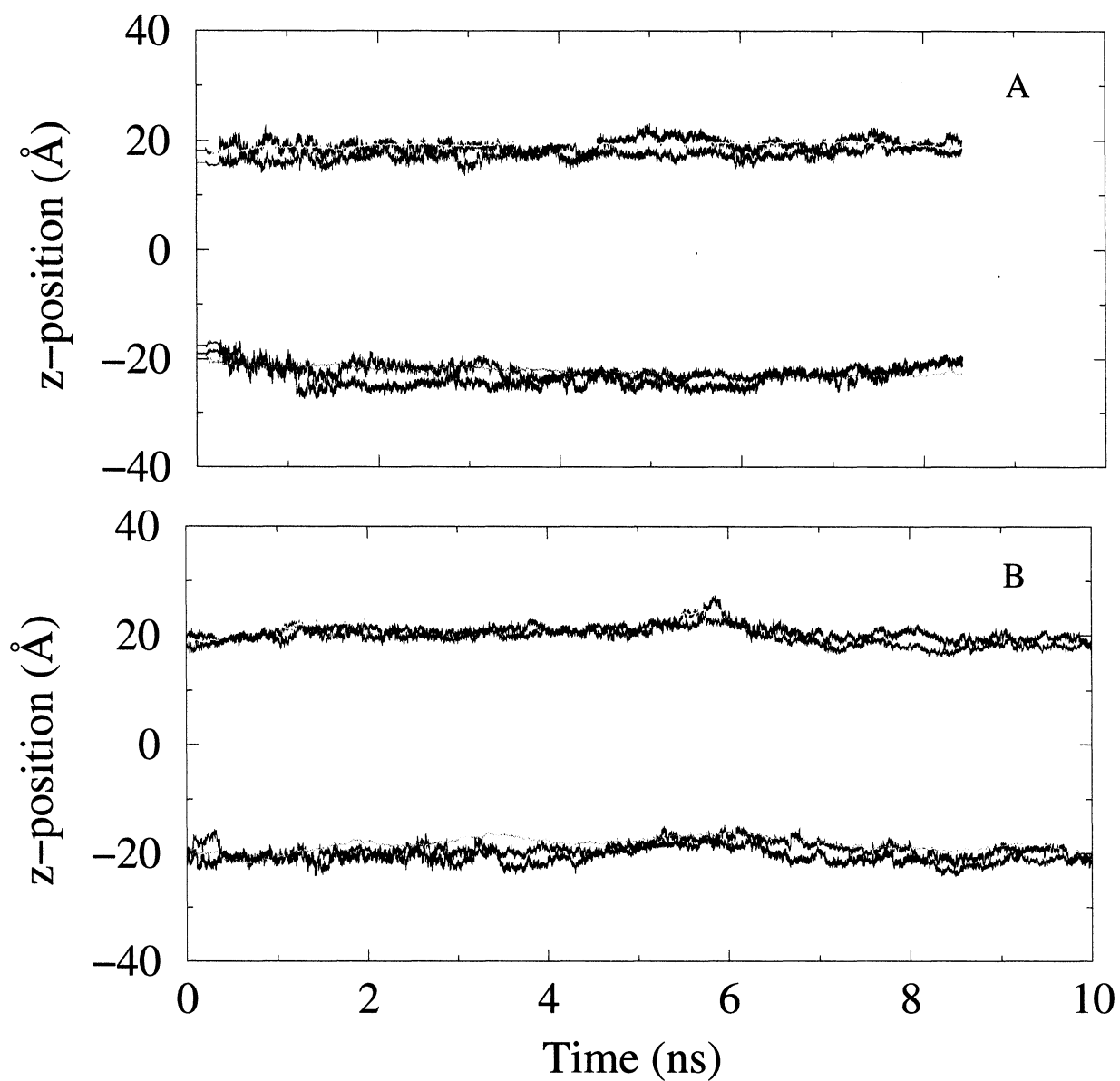


Figure 6.14: Z position of the lysine nitrogen atoms and the average z position of the lipid phosphorus atoms during the simulation with the peptide initially aligned along the z axis (A) and the simulation with the peptide initially tilted in the bilayer (B). Atomic z positions of lysine nitrogens in upper bilayer leaflet are represented blue and green lines while lysine nitrogens in the lower bilayer leaflet are represented by red and black lines. The average z position of the lipid phosphorus atoms in the upper and lower bilayer leaflets are represented by yellow and brown lines respectively.

Residue	Peptide initially along z axis	Peptide initially tilted in bilayer
lysine 1	$-4.00 \pm 1.51 \text{ \AA}$	$-3.89 \pm 1.39 \text{ \AA}$
lysine 2	$-4.15 \pm 1.01 \text{ \AA}$	$-4.24 \pm 0.93 \text{ \AA}$
lysine 25	$1.19 \pm 1.06 \text{ \AA}$	$2.80 \pm 0.74 \text{ \AA}$
lysine 26	$1.86 \pm 1.61 \text{ \AA}$	$1.98 \pm 0.91 \text{ \AA}$

Table 6.3: Z positions of the lysine side-chain nitrogens with respect to the lysine C_α carbon positions. These results indicate that the ends of the lysine side-chains extend beyond the position of the lysine C_α carbons which provides evidence for “snorkelling” of the lysine side-chains.

lock the helix in a fixed azimuthal orientation but allow small fluctuations about the helix axis. Though the lysine sidechains prevent rotation about the helix axis, extension of the lysine sidechains may allow the peptide to accommodate a greater average tilt in the bilayer. This could account for such large angular fluctuations observed in helix tilt and the larger quadrupolar splittings obtained for the second simulation.

The results provide a more detailed view of the short-time-scale dynamics of transmembrane segments in a model membrane environment. The dynamic information obtained from the simulation provides insight into a mechanism that may play a primary role in modulating peptide-peptide interactions which, in turn, may lead to stable dimer structures for a variety of structural motifs. The behaviour revealed could potentially modulate helix-helix interactions and mediate knobs-into-holes (or ridges-into-grooves) packing mode of residues in the interfacial region of stable dimer structures. The existence of a preferred azimuthal orientation about the peptide long axis, in the presence of a non-zero helix tilt, may encourage interfacial alignment of monomers which may lead to stable dimerization. The simulations presented here provide an interesting starting point for further investigations of helix-helix interactions among a variety of structural motifs.

Chapter 7

^2H NMR Studies of Transmembrane Polypeptides: Polyalanine-leucine with Interaction Motifs

7.1 Introduction

Peptide-peptide interactions play a major role in the function of membrane proteins with single and multiple transmembrane regions [87]. The interactions can be specific and depend on special amino acid sequences known as motifs. Through statistical analysis Senes *et al.* [88] have shown that glycine residues in the sequence GxxxG occur frequently in the data base of known protein structures with transmembrane helices. One particular variant of this sequence is found in natural glycoporphin A (GPA). Studies carried out by Bormann and Marchesi [89] showed that this glycoporphin A motif was responsible for the formation of dimers. This observation has implications in many cellular processes where protein association plays a role.

The studies of Lemmon *et al.* [25,90] demonstrated that the dimerization of GPA transmembrane domains is mediated by seven residues. The sequence of 7 residues

thought to be responsible for helix-helix interactions in GPA dimers is LIxxGVxxGVxxT, where the x represents an amino acid [81,91]. The packing of residues within this interfacial region of glycoporphin A has been investigated using ^{13}C NMR by Smith *et al.* [87]. Those studies confirm close packing of glycine and valine residues in the dimer interface which form a “knobs and holes” packing arrangement. In fact, the results indicate that the distances between C_α carbons on glycines of glycoporphin A dimers are approximately 4.1 Å and 4.3 Å which places the helices in close contact. Further NMR measurements carried out by Smith *et al.* [92] on ^{13}C labeled dimeric GPA show that the threonine sidechain, which has a highly polar hydroxyl group, has a conformation which places it in direct hydrogen bonding contact with the opposite helix. Specific mutations within the sequence of this motif are observed to suppress dimer formation and therefore illustrate the importance of specific interactions between transmembrane segments of proteins [93].

Specific interactions between helices and interactions with the surrounding membrane may affect dimer formation and hence protein function. Extensive MD simulations of GPA in phosphatidylcholine bilayers with varying chain lengths and degrees of acyl chain saturation have been carried out by Petrache *et al.* [94]. The results of these simulation studies show that the helix environment interaction energy favors the formation of GPA dimers when dispersed in unsaturated lipid. The structure of GPA peptide remains α -helical through the simulations but fluctuations in molecular structure about the average molecular conformation are modulated by bilayer properties [94]. An interesting issue is the extent to which peptide-peptide and lipid-peptide interactions are modulated by particular transmembrane motifs. If these interactions affect peptide dynamics then the range of motions that allow particular motifs to

interact with each other may be significant to the function of membrane spanning proteins.

7.2 Polyalanine-leucine containing GPA interaction motifs

Chapter 5 presented a NMR study of KALP peptides in bilayer membranes. The observations suggested that KALP peptides undergo rapid reorientation about the bilayer normal and there was some interaction between peptides. The observations also suggested that rotation about the bilayer normal and peptide association may be general properties of transmembrane peptides and are not specific to transmembrane segments of natural proteins like EGFR.

As stated earlier, peptide association is often dependent on particular sequences of amino acids or motifs. If the dynamics of KALP-derived peptides can be affected by the presence of such motifs, then the motif orientation and the range of molecular motion about some average orientation may be an important factor in determining the extent to which peptides interact.

This chapter presents a ^2H NMR investigation of model peptides which contain a natural glycoporphin A motif. Sequences of the polypeptides used in this study are



and



where the italicized characters indicate the seven residues of the GPA motif and the lower case A indicates the position of the deuterated alanine methyl group in the

peptide sequence. We note that both polypeptides have the same number of amino acids and the alanine methyl group is deuterated at the same position for each peptide. However, the GPA motif on the first polypeptide has been shifted by one amino acid residue when compared to the second peptide. Since the terminal residues are the same for each peptide, we expect the interactions of the lysine sidechains with the membrane surface will be similar for each peptide. By shifting the motif position within the sequence we can investigate the effect of motif orientation on specific peptide-peptide interactions. The orientation of the motif in the amino acid sequence may lead to significantly different interactions between peptides which has implications in understanding specific interactions between natural protein transmembrane segments.

7.3 Results

The samples investigated here are illustrated in Table 7.1 and correspond to a concentration of 4 mol % peptides dispersed in POPC bilayers and have been prepared according to the protocol presented in Chapter 4. Both spectra and echo decay measurements were carried out for each sample within a temperature range from 25 °C to 55 °C.

Selected spectra obtained for GPA22-1 and GPA22-2 peptides at a concentration of 4 mol % are presented in Figure 7.1 and Figure 7.2 respectively. At 55 °C the spectrum for GPA22-1 is a Pake doublet with a quadrupolar splitting of ~ 8.4 kHz. The Pake feature (~ 6.8 kHz) is somewhat apparent from GPA22-2 peptides at 55 °C but is not as pronounced as in the GPA22-1 spectra. As discussed in Chapter 5, deuterated methyl groups on static polypeptides are expected to give a quadrupolar

Peptide Sample	Amino Acid Sequence
GPA22-1	CH ₃ CO-KKLALLILAGVLAGVLaLALAKK-CO-NH ₂
GPA22-2	CH ₃ CO-KKLALALILAGVLAGVLaLALAKK-CO-NH ₂

Table 7.1: Samples used in this ²H NMR investigation. Experiments on a 4 mol % peptides were carried out at varying temperatures. The lowercase A represents the position of the deuterated alanine methyl group along the peptide sequence.

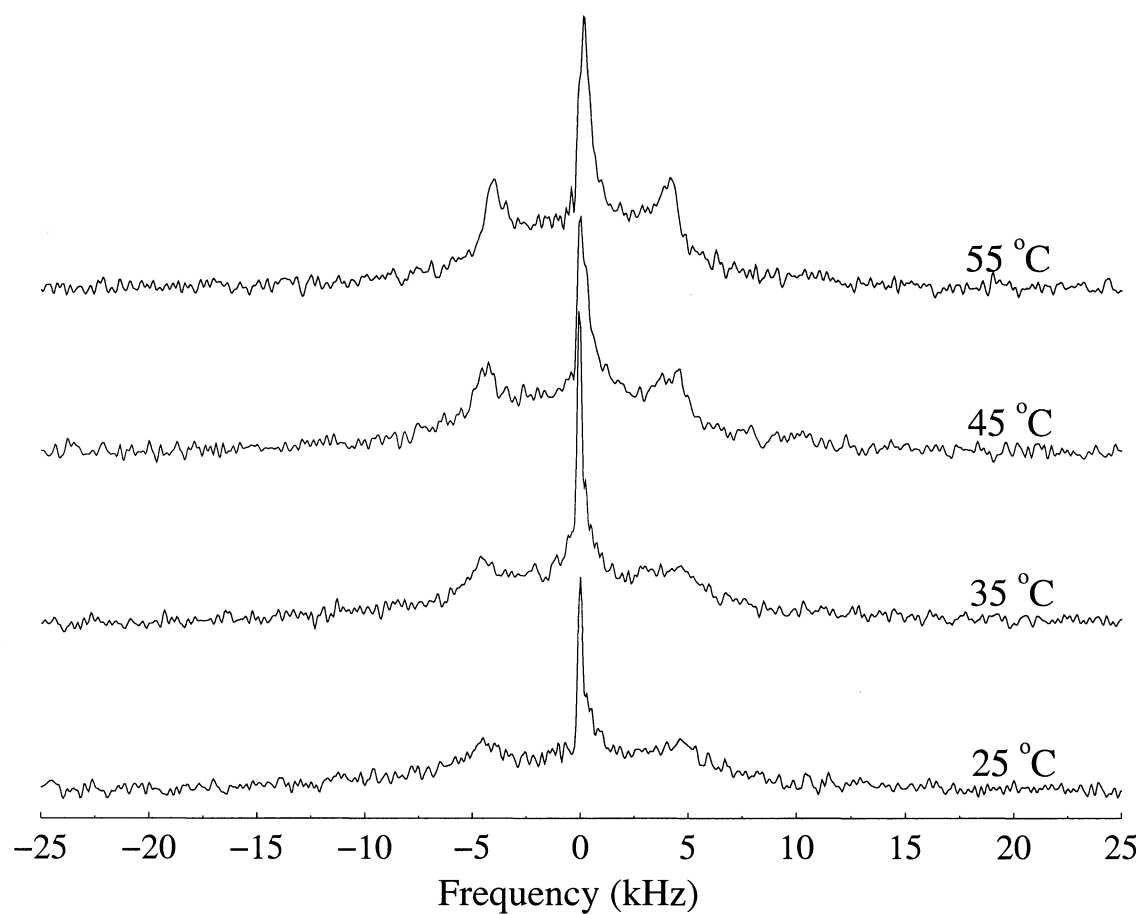


Figure 7.1: ^2H NMR spectra of GPA22-1 peptides at a concentration of 4 mol % for varying temperatures. The spectrum at 55 °C is a Pake doublet which indicates that the transmembrane segment is undergoing rapid axially symmetric motion. At lower temperatures spectral broadening suggests that peptide-peptide interactions hinder rapid peptide reorientation.

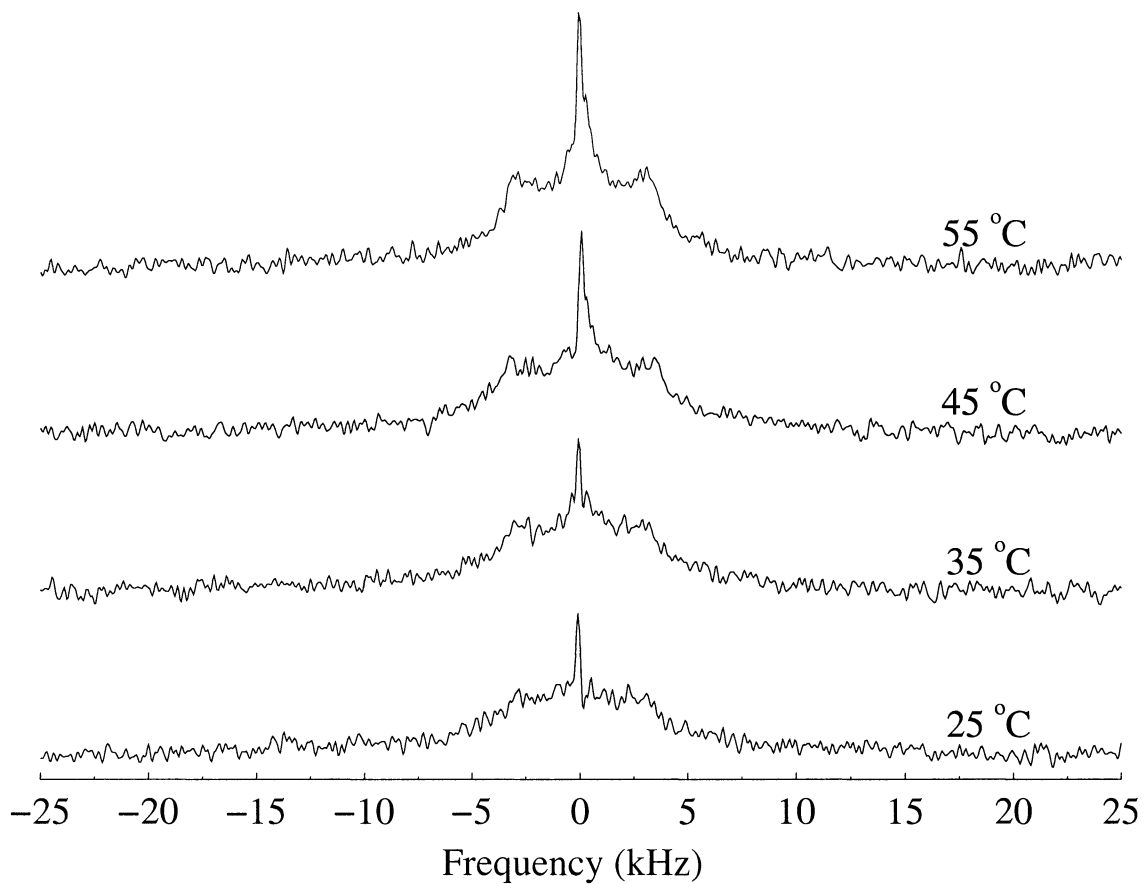


Figure 7.2: ^2H NMR spectra of GPA22-2 peptides at a concentration 4 mol % for varying temperatures. The spectrum at 55 °C is a Pake doublet which indicates that the transmembrane segment is undergoing rapid axially symmetric motion. At lower temperatures spectral broadening suggests that peptide-peptide interactions hinder rapid peptide reorientation.

splitting of about 41.85 kHz based on a quadrupolar coupling constant of 167.5 kHz. Similar to LA17 and LA22 peptides presented in Chapter 5, the splittings presented here are also significantly smaller than the estimate for rotating methyl groups on static peptides. In this case, the correlation time for rapid rotation must be shorter than the characteristic NMR timescale (10^{-6} s - 10^{-5} s).

The change in spectral shape at temperatures below 55 °C for each GPA22 peptide reflects the onset of hindered rotation for some part of the peptide population. It is important to note that the evidence for hindered rotation appears to be more pronounced for GPA22-2 peptides. While the 90° edges of the spectra for GPA22-1 peptides are observable down to 25 °C the same feature is not observable for GPA22-2 peptides at lower temperatures.

Figure 7.3 present log plots of quadrupolar echo decay measurements on GPA22 peptides. Molecular motion modulates the quadrupolar echo amplitude and therefore echo decay reflects the dynamics of peptides in bilayers. There appears to be a difference in the spread of the echo decays with decreasing temperature for each peptide. This spread may be more apparent in Figure 7.4 which presents the measured echo decay times, T_2^{qe} . While T_2^{qe} decreases substantially for GPA22-1 peptides as temperature is lowered, the echo decay time for GPA22-2 peptides remains relatively constant.

As discussed in Chapter 5, the correlation time for reorientation can be estimated using the analysis of Pauls *et al.* [42] assuming exponential echo decay. There is some departure from exponential echo decay which is mainly due to low signal to noise in the acquired quadrupolar echoes especially for longer pulse separations. Incorrect

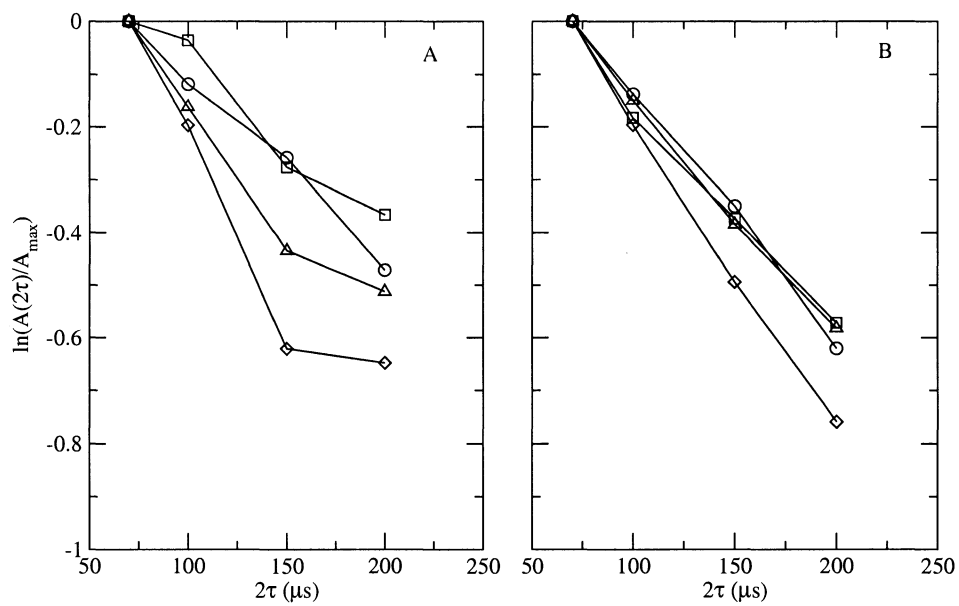


Figure 7.3: Quadrupolar echo decay curves for GPA22-1 (A) or GPA22-2 (B) peptides at a concentration of 4 mol % for temperatures 25 °C (◇), 35 °C (△), 45 °C (□), and 55 °C (○)

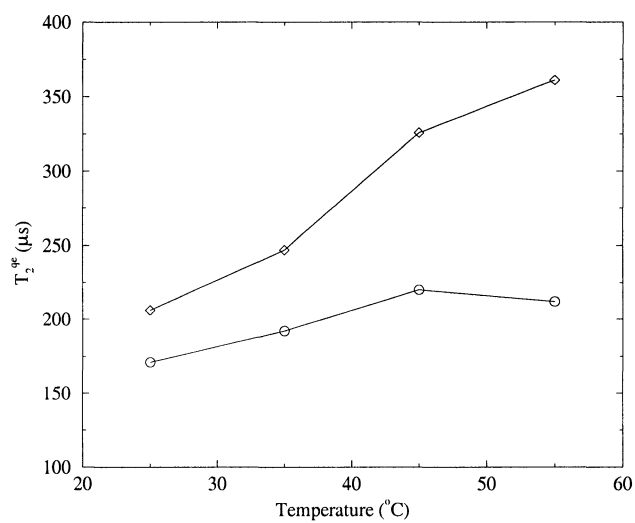


Figure 7.4: Quadrupolar echo decay times (T_2^{qe}) for GPA22-1 (\diamond) and GPA22-2 (\circ) peptides at a concentration of 4 mol % for varying temperatures

calibration of 90° pulses used in the quadrupole echo sequence may also be an influencing factor that would affect echo amplitude. Assuming exponential echo decay the calculated correlation times are presented in Figure 7.5. The correlation times for both peptides are $\sim 10^{-7}$ s. However, the time for reorientation of GPA22-2 peptides is shorter than for GPA22-1 peptides at all temperatures. The change in correlation time for decreasing temperature appears to be more significant for GPA22-1 peptides.

7.4 Discussion

At higher temperatures the spectra for GPA22 peptides are Pake doublets (Figure 7.1 and Figure 7.2) indicating that the peptides in each sample must be undergoing rapid axially symmetric motion. The Pake feature (~ 6.8 kHz) is somewhat apparent from GPA22-2 peptides at 55°C but hindered rotation of the peptides have a significant affect on the shape of the spectra obtained for GPA22-2 peptides.

As discussed in Chapter 5, a 90° splitting of about 41.85 kHz is expected for deuterated methyl groups on static peptides. However, the splittings presented here are significantly smaller than the estimate for rapidly rotating methyl groups on static peptides. This means that reorientation of these peptides must be fast enough to lead to additional averaging of the quadrupolar interaction and hence a reduction of the quadrupolar splitting from the 41.85 kHz splitting expected for static peptides. As previously described in Chapter 5 for LA peptides, the quadrupolar splittings for GPA22-1 and GPA22-2 obtained here are also significantly larger than the splittings estimated for peptides that undergo fast rotation about the helix axis.

It is important to note the difference between the hydrophobic bilayer thickness for POPC (26 Å) and the hydrophobic length of the GPA22 peptides (33 Å). Due

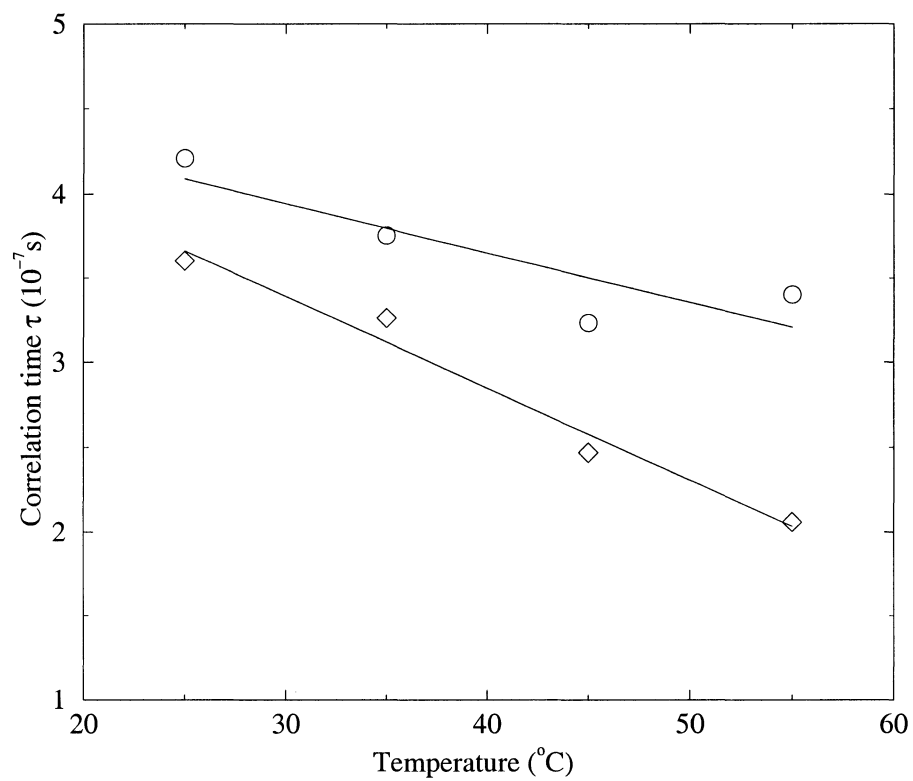


Figure 7.5: Correlation times for GPA22-1 (\diamond) and GPA22-2 (\circ) peptides at a concentration of 4 mol % in POPC bilayers

to the degree of hydrophobic mismatch the peptides probably maintain a tilted orientation in the bilayer since this will minimize exposure of hydrophobic amino acid sidechains to the polar membrane-water interface. Previous studies of the epidermal growth factor transmembrane segment [7] and artificial peptides [10, 13] also indicate that peptide segments undergo rapid rotation about the bilayer normal. This observation is also true for LA17 and LA22 peptides presented in Chapter 5. Based on the magnitude of splittings obtained from the NMR measurements, the degree of hydrophobic mismatch, and the results of previous studies it seems reasonable to conclude that GPA22 peptides tilt in the bilayer and rapidly reorient about the bilayer normal. It is interesting to note the difference between quadrupolar splittings for GPA22-1 and GPA22-2 peptides. Since each of the GPA22 peptides are deuterated at the same sequence position then the difference in deuteron splittings suggests that peptide orientation is sensitive to the position of the GPA motif. Carrying out an analysis similar to that described by Jones *et al.* [7] on EGFR transmembrane segments suggests that the difference in quadrupolar splittings obtained for each of the GPA22 peptides could result from an orientational difference of approximately 10° about the helix axis.

As temperature is lowered from 55°C to 25°C changes in the spectra (for both GPA22-1 and GPA22-2 peptides) indicate that motions of the peptides change as temperature is decreased. However, the 90° edges of the Pake doublet feature are still somewhat apparent even at 25°C . For GPA22-2 evidence of departure from fast, axially symmetric reorientation is apparent in the spectra at all temperatures.

These observations suggest that GPA22 peptides are monomeric at higher temperatures while broadening in the spectra at lower temperatures supports transient

peptide-peptide interactions. The spectra for GPA22-2 peptide appear to be broadened at all temperatures which suggests that interactions between GPA22-2 peptides must be different from interactions between GPA22-1 peptides. This may arise due to the difference in orientation of the GPA motifs in the peptide sequence. If the orientation of the motif affects the dynamics of peptides through peptide-peptide interactions then the orientation of the motif interface may be important to the association of natural proteins having transmembrane helices.

The appearance of a low-amplitude, 25 kHz feature in spectra obtained for LA17 and LA22 peptides was indicative of a population of highly immobilized peptide. Such features have also been observed in ^2H NMR studies of transmembrane segments of naturally occurring protein transmembrane segments. This observation suggested that protein transmembrane segments associated to form dimers. Although broadening is apparent with decreasing temperature, observations reported here in this chapter do not show evidence for persistent peptide dimer formation with this artificial peptide even though a GPA interaction motif is present. It may be the case that the orientation of the GPA motif hinders helix-helix interactions and therefore a monomeric population remains more energetically favorable.

Since echo decay is dependent on slow molecular motions, the echo decay experiment can be used to obtain information about reorientational processes which occur over the experiment timescale. For each sample, the measured T_2^{qe} decreases with decreasing temperature (see Figure 7.4). The echo decay time for GPA22-1 peptides at 55 °C was calculated to be 361 μs which decreases to 200 μs at 25 °C. The measured echo decay time for GPA22-2 at 55 °C is approximately 212 μs while at 25 °C it decreases to 171 μs . We note that over the temperature range from 55 °C to

25 °C echo decay times decrease more for GPA22-1 peptides. When the echo decay measurements are compared against the acquired spectra, it is apparent that the decrease of echo decay times with decreasing temperature may be related to the increase in broadening for the acquired spectra. For instance, the GPA22-1 peptide spectra are characteristic of axially symmetric motion at 55 °C and become broadened as temperature is lowered. A significant change in T_2^{qe} also accompanies the change in the spectral shape which suggests that interactions leading to spectral changes are also responsible for the observed change in echo decay. In contrast, the spectrum for GPA22-2 at 55 °C does not exhibit a sharp Pake doublet but instead has rounded edges resulting from broadening. This indicates that rotation of the peptides must be hindered during the timescale of the NMR experiment. As temperature is lowered the spectral shape changes slightly but the extent of broadening is not as pronounced as for GPA22-1 peptides. Accompanying this slight change in spectral shape is a small change in the quadrupolar echo relaxation time.

As discussed in Chapter 2 and Chapter 5, molecular reorientation leads to an apparent second moment, ΔM_2 , which in the short correlation time limit ($\Delta M_2 \tau_c^2 \ll 1$) can be used to obtain the correlation time for the reorientational process leading to echo decay. Following the analysis of Pauls *et al.* [42] the correlation times were calculated and are presented in Figure 5.6. The correlation times calculated for each peptide decrease with increasing temperature. This observation is similar to the results obtained for LA17 and LA22 peptides in Chapter 5. The correlation times for GPA22-2 are consistently longer than those calculated for GPA22-1 peptides. These observations support a model where the peptides are tilted in the bilayer and transiently interfere with each other. The consistently longer correlation times, the

shorter echo decay times and the spectral broadening results suggest that peptide-peptide interactions may be more frequent for GPA22-2 or the duration of contact between helices is longer than for GPA22-1 peptides. The observed temperature dependence of the correlation times is also consistent with the observed changes in the observed spectra. That is, as the correlation time for reorientation increases (with decreasing temperature), the spectra become more broadened.

7.5 Summary

Quadrupolar splittings obtained in this study were different for each GPA22 peptide. This observation suggests that peptide orientation is sensitive to the position of the GPA interaction motif and therefore peptide orientation may be dependent on specific interactions that depend on peptide sequence. It is interesting to note that the degree of broadening in the observed spectra is also dependent on the motif position and illustrates that positioning of the GPA motif changes peptide dynamics. The observed relaxation times also suggest that shifting the orientation of the GPA motif leads to a change in peptide motions.

Broadening of the observed spectra with decreasing temperature suggests departure from rapid axially symmetric reorientation and therefore supports the presence of peptide-peptide interactions that result in hindered rotation of the peptides. Additionally, the estimated correlation times support a model where the peptides transiently interfere with each other. In fact, the correlation times and spectral broadening both suggest that peptide-peptide interactions may be more frequent for GPA22-2 peptides.

Though natural GPA molecules are known to form strong dimers, the observations

presented here do not show evidence for persistent peptide dimerization for artificial peptides with GPA motifs. Natural dimers are often observed to have a crossing angle which is simply the angle between the two helices. The crossing angle between transmembrane peptides in GPA dimers has been predicted to be 35° [92]. This crossing angle places the GLY and VAL residues on opposite helices in close contact. Though close contact may still be possible, alignment of the peptide dimerization motifs may be hindered due to positioning of the motif within the sequence. The crossing angle may also be affected by the length of the transmembrane segments which constrain the peptides in an orientation that could hinder dimer formation.

Chapter 8

Conclusions

^2H NMR and MD simulation have been used to study the structure, dynamics and aggregation characteristics of artificial membrane spanning polypeptides. Since ^2H NMR spectra are sensitive to molecular orientation, the technique was used to place limits on the orientation of polypeptides in lipid bilayer environments. In addition to orientational information, ^2H NMR spectra also provide information concerning the dynamics of methyl group deuterated polypeptides. While NMR is used to investigate peptide orientation and dynamics, MD simulation was employed to investigate peptide dynamics on a time-scale which is much shorter than the NMR experiment.

^2H NMR and molecular modeling studies presented in Chapter 5 on artificial KALP peptides confirm that the model peptides studied here adopt a preferred tilt and azimuthal orientation in model membrane environments. At higher temperatures the spectra indicate that peptides are undergoing rapid axially symmetric motion about the bilayer normal with a correlation time $\sim 10^{-7}\text{s}$. Additionally, broadening of the spectra with decreasing temperatures suggests the presence of transient peptide-peptide interactions. Comparison with earlier studies on EGFR suggest that these characteristics may be general properties of transmembrane peptides.

MD simulations presented in Chapter 6 illustrate the uniform helical nature of a transmembrane polypeptide studied in Chapter 5. The results provide a detailed view of the dynamics of transmembrane segments on a time-scale that is much shorter (10^{-9} s) than the NMR experiment. The results show that hydrophobic mismatch leads to peptide tilt which is consistent with the observations presented in Chapter 5. In the presence of peptide tilt, there is some indication that the peptide has a preferred orientation about the helix axis. The information obtained from the simulation provides insight into a possible mechanism that may drive peptide-peptide interactions. The behaviour revealed could potentially modulate helix-helix interactions and mediate the packing mode of dimer structures.

Chapter 7 presented ^2H NMR studies of polypeptides which contain a glycoporphin A motif. The results suggest that the orientation of the glycoporphin motif within the transmembrane region of artificial polypeptides alters the orientation and dynamics of these peptides in model membranes. This result illustrates that the interactions leading to peptide orientation may be specific in nature and can depend on the orientation of the amino acid sequence about the helix axis. The results presented here have not shown evidence for dimer formation in LA peptides with GPA motifs. This is interesting since natural GPA is known to form stable dimers. This suggests that other factors may be important to the dimerization properties of transmembrane peptides. The degree of broadening in the spectra is dependent on the position of the glycoporphin motif which suggests that altering the position of the motif also affects the interactions between transmembrane peptides. This study suggests that specificity of interactions between peptide segments depends not only on the peptide sequence, but also on motif orientation. Such results may further explain the specific interactions

between membrane spanning segments of natural proteins and how the structure of membrane spanning segments is important to protein function.

The results presented in this thesis provide an overview of the behaviour of membrane spanning polypeptides. Though the structure of the artificial KALP polypeptides presented here is uniform, the dynamical behaviour is complicated and depends on many factors such as temperature, concentration and structural motif. Though the motif studies presented here do not show evidence for peptide dimerization, it appears that peptide dynamics is altered by changing the position of the interaction motif. In order to further understand peptide dynamics and helix-helix interactions a ^2H NMR study of alanine deuterated natural glycophorin A could be interesting. Since GPA is known to form strong dimers, we may be able to better characterize ^2H NMR spectral features resulting from a dimer structure. Such studies may provide information about timescale of peptide reorientation and possibly information about the timescale for cellular processes that involve peptide dimerization.

Bibliography

- [1] R. B. Gennis. *Biomembranes: molecular structure and function*. Springer-Verlag, 1989.
- [2] M. D. Houslay and K. K. Stanley. *Dynamics of biological membranes: influence on synthesis, structure and function*. John Wiley & Sons, 1982.
- [3] W. M. Kavanaugh and L.T. Williams. *Signal transduction. Signaling through receptor tyrosine kinases*. Chapman & Hall, 1996.
- [4] P. van der Geer, T. Hunter, and R.A. Lindberg. Receptor protein tyrosine kinases and their signal transduction pathways. *Ann. Rev. Cell Biol.*, 10:251–337, 1994.
- [5] D. H. Jones, A. C. Rigby, K. R. Barber, and C. W. M. Grant. Oligomerization of the EGF receptor transmembrane domain: A ^2H NMR study in lipid membranes. *Biochem.*, 36:12616–12624, 1997.
- [6] M. R. Morrow and C. W. M. Grant. The EGF receptor transmembrane domain: Peptide-peptide interactions in fluid bilayer membranes. *Biophys. J.*, 79:2024–2032, 2000.
- [7] D. H. Jones, K. R. Barber, E. W. VanDerLoo, and C. W. M. Grant. Epidermal growth factor receptor transmembrane domain: ^2H NMR implications for orientation and motion in a bilayer environment. *Biochem.*, 37:16780–16787, 1998.

- [8] A. C. Rigby, K. R. Barber, G. S. Shaw, and C. W. M. Grant. Transmembrane region of the epidermal growth factor receptor: Behavior and interactions via ^2H NMR. *Biochem.*, 35:12591–12601, 1996.
- [9] D. H. Jones, K. R. Barber, and C. W. M. Grant. The EGF receptor transmembrane domain: ^2H NMR study of peptide phosphorylation effects in a bilayer environment. *Biochem.*, 37:7504–7508, 1998.
- [10] P. C. A. van der Wel, E. Strandberg, J. A. Killain, and R. E. Koeppe II. Geometry and intrinsic tilt of a tryptophan anchored transmembrane α -helix determined by ^2H NMR. *Biophys. J.*, 83:1479–1488, 2002.
- [11] E. Strandberg, S. Morein, D. T. S. Rijkers, R. M. J. Liskamp, P. C. A. van der Wel, and J. A. Killian. Lipid dependence of membrane anchoring properties and snorkeling behavior aromatic and charged residues in transmembrane peptides. *Biochem.*, 41:7190–7198, 2002.
- [12] M. R. R. de Planque, E. Goormaghtigh, D. V. Greathouse, R. E. Koeppe II, J. A. W. Kruijtzter, R. M. J. Liskamp, B. de Kruijff, and J. A. Killian. Sensitivity of single membrane spanning α -helical peptides to hydrophobic mismatch with a lipid bilayer: Effects on backbone structure, orientation and extent of membrane incorporation. *Biochem.*, 40:5000–5010, 2001.
- [13] S. Sharpe, K. R. Barber, C. W. M. Grant, D. Goodyear, and M. R. Morrow. Organization of model helical peptides in lipid bilayers: Insight into the behavior of single-span protein transmembrane domains. *Biophys. J.*, 83:345–358, 2002.
- [14] U. Harzer and B. Bechinger. Alignment of lysine-anchored membrane peptides under conditions of hydrophobic mismatch: A CD, ^{15}N and ^{31}P solid state NMR spectroscopy investigation. *Biochem.*, 39:13106–13114, 2000.

- [15] S. Morein, J. A. Killian, and M. M. Sperotto. Characterization of the thermotropic behavior and lateral organization of lipid-peptide mixtures by a combined experimental and theoretical approach: Effects of hydrophobic mismatch and role of flanking residues. *Biophys. J.*, 82:1405–1417, 2002.
- [16] M. R. R. de Planque, J. A. W. Kruijtzter, R. M. J. Liskamp, D. Marsh, D. V. Greathouse, R. E. Koeppe II, B. de Kruijff, and J. A. Killian. Different membrane anchoring positions of tryptophan and lysine in synthetic transmembrane α -helical peptides. *J. Biol. Chem.*, 274:20839–20846, 1999.
- [17] H. I. Petrache, D. M. Zuckerman, J. N. Sachs, J. A. Killian, R. E. Koeppe II, and T. B. Woolf. Hydrophobic matching mechanism investigated by molecular dynamics simulations. *Langmuir*, 18:1340–1351, 2002.
- [18] J. A. Killian, I. Salemink, M. de Planque, G. Lindholm, R. E. Koeppe II, and D. V. Greathouse. Induction of non-bilayer structures in diacylphosphatidylcholine model membranes by transmembrane α -helical peptides: Importance of hydrophobic mismatch and proposed role of tyrtophans. *Biochemistry*, 35:1037–1045, 1996.
- [19] Y-P. Zhang, R. N. A. H. Lewis, R. S. Hodges, and R. N. McElhaney. Peptide models of helical hydrophobic transmembrane segments of membrane proteins. 2. Differential scanning calorimetric and FTIR spectroscopic studies of the interaction of Ac-K₂-(LA)₁₂-K₂-amide with phosphatidylcholine bilayers. *Biochem.*, 34:2362–2371, 1995.
- [20] Y-P. Zhang, R. N. A. H. Lewis, G. D. Henry, B. D. Sykes, R. S. Hodges, and R. N. McElhaney. Peptide models of helical hydrophobic transmembrane segments of membrane proteins. 1. Studies of the confirmation, intrabilayer orientation, and amide hydrogen exchangeability of Ac-K₂-(LA)₁₂-K₂-amide. *Biochem.*, 34:2348–2361, 1995.

- [21] W. K. Subczynski, R. N. A. H. Lewis, R. N. McElhaney, R. S. Hodges, J. S. Hyde, and A. Kusumi. Molecular organization and dynamics of 1-palmitoyl-2-oleoylphosphatidylcholine bilayers containing a transmembrane α -helical peptide. *Biochem.*, 37:3156–3164, 1998.
- [22] J. A. Killian and G. von Heijne. How proteins adapt to a membrane-water interface. *Trends in biochemical sciences*, 25:429–434, 2000.
- [23] T. M. Weiss, P. C. A. van der Wel, J. A. Killian, R. E. Koeppe II, and H. W. Huang. Hydrophobic mismatch between helices and lipid bilayers. *Biophys. J.*, 84:379–385, 2003.
- [24] R. E. Dickerson and I. Geis. *The structure and action of proteins*. W. A. Benjamin, Inc., 1969.
- [25] M. A. Lemmon, J. M. Flanagan, J. F. Hunt, B. D. Adair, B. J. Bormann, C. E. Dempsey, and D. M. Engelman. Glycophorin A dimerization is driven by specific interactions between transmembrane α -helices. *J. Biol. Chem.*, 267:7683–7689, 1992.
- [26] J. McConnell. *The theory of nuclear magnetic relaxation in liquids*. Cambridge University Press, 1987.
- [27] P. T. Callaghan. *Principles of nuclear magnetic resonance microscopy*. Clarendon Press, 1991.
- [28] C. P. Slichter. *Principles of magnetic resonance*. Springer-Verlag, 1990.
- [29] E. Fukushima and S. B. W. Roeder. *Experimental pulse NMR: A nuts and bolts approach*. Addison-Wesley Publishing Co., 1981.
- [30] J. H. Davis. Deuterium nuclear magnetic resonance spectroscopy in partially ordered systems. *J. Comp. Chem.*, 20:1153–1164, 1999.

- [31] H. S. Robertson. *Statistical thermophysics*. Prentice Hall, 1998.
- [32] R. Kimmich. *NMR tomography, diffusometry, relaxometry*. Springer, 1997.
- [33] M. Mehring. *Principles of high resolution NMR in solids*. Springer-Verlag, 1981.
- [34] A. Abragam. *The Principles of Nuclear Magnetism*. Clarendon Press, 1961.
- [35] D. J. Griffiths. *Introduction to Electrodynamics*. Prentice Hall, 1999.
- [36] J. Seelig. Deuterium magnetic resonance: Theory and application to lipid membranes. *Q. Rev. of Biophys.*, 10:353–418, 1977.
- [37] J. H. Davis. The description of membrane lipid conformation, order and dynamics by ^2H -NMR. *Bioch. et Bioph. A*, 737:117–171, 1983.
- [38] C. Schmidt, B. Blümich, and H. W. Spiess. Deuteron two-dimensional exchange NMR in solids. *J. Chem. Phys.*, 79:269–290, 1988.
- [39] D. Canet. *Nuclear magnetic resonance: Concepts and methods*. John Wiley Sons, 1996.
- [40] J. H. Davis. Deuterium nuclear magnetic resonance and relaxation in partially ordered systems. *Advances in Magnetic Resonance*, 13:195–223, 1989.
- [41] J. H. Davis, K. R. Jeffery, M. Bloom, M. I. Valic, and T. P. Higgs. Quadrupolar echo deuteron magnetic resonance spectroscopy in ordered hydrocarbon chains. *Chem. Phys. Lett.*, 42:390–394, 1976.
- [42] K. P. Pauls, A. L. MacKay, O. Soderman, M. Bloom, A. K. Tanjeo, and R. S. Hodges. Dynamic properties of the backbone of an integral membrane polypeptide measured by ^2H NMR. *Eur. Biophys. J.*, 12:1–11, 1985.
- [43] D. Frenkel and B. Smit. *Understanding molecular dynamics simulations: From algorithms to applications*. Academic Press, 1996.

- [44] J. B. Gobson, A. N. Goland, M. Milgram, and G. H. Vineyard. Dynamics of radiation damage. *Phys. Rev.*, 120:1229–1253, 1960.
- [45] A. Rahman. Correlations in the motion of atoms in liquid argon. *Phys. Rev.*, 136:A405–A411, 1964.
- [46] L. Kale, R. Skeel, M. Bhandarkar, R. Brunner, A. Gussoy, J. Phillips, A. Shinzaki, K. Varadarajan, and K. Schulten. NAMD2: Greater scalability for parallel molecular dynamics. *J. Comp. Phys.*, 151:283–312, 1999.
- [47] S. E. Feller, D. Yin, R. W. Pastor, and A. D. MacKerell Jr. Molecular dynamics simulation of unsaturated lipid bilayers at low hydration: Parameterization and comparison with diffraction studies. *Biophys. J.*, 73:2269–2279, 1997.
- [48] J. Gullingsrud, D. Kosztin, and K. Schulten. Structural determinants of mscl gating by molecular dynamics simulations. *Biophys. J.*, 80:2074–2081, 2001.
- [49] D. C. Rapaport. *The art of molecular dynamics simulation*. Cambridge University Press, 1995.
- [50] Goldstein. *Statistical mechanics*. Academic Press, 1975.
- [51] A. D. MacKerell, D. Bashford, M. Bellott, R. L. Dunbrack, J. D. Evenseck, M. J. Field, S. Fischer, J. Gao, H. Guo, S. Ha, D. Joseph-McCarthy, L. Kuchnir, F. T. K. Lau, C. Mattos, S. Michnick, T. Ngo, D. T. Nguyen, B. Prodhom, W. E. Reiher, B. Roux, M. Schlenkrich, J. C. Smith, R. Stote, J. Straub, M. Watanabe, J. Wiorcikiewicz-Kuczera, D. Yin, and M. Karplus. All-atom empirical potential for molecular modeling and dynamics studies of proteins. *J. Phys. Chem. B*, 102:3586–3616, 1998.
- [52] M. E. Tuckerman and G. J. Martyna. Understanding modern molecular dynamics: Techniques and applications. *J. Chem. Phys.*, 104:159–178, 2000.

- [53] J. P. Ryckaert, G. Ciccotti, and H. J. C Berendsen. Numerical integration of the cartesian equations of motion of a system with constraints: Molecular dynamics of n-alkanes. *J. Comp. Phys.*, 23:327–341, 1977.
- [54] D. J. Griffith. *Electrodynamics*. Cambridge University Press, 1987.
- [55] P. Lorrain, D. R. Corson, and Francois Lorrain. *Electromagnetic fields and waves*. W. H. Freeman and Company, 1988.
- [56] T. Darden, D. York, and Lee Padersen. Particle mesh ewald: An nlogn method for ewald sums in large systems. *J. Chem. Phys.*, 98:10089–10092, 1993.
- [57] H. C. Andersen. Molecular dynamics simulations at constant pressure and/or temperature. *J. Chem. Phys.*, 72:2384–2393, 1980.
- [58] S. E. Feller, Y. Zhang, and R. W. Pastor. Constant pressure molecular dynamics simulation: The Langevin piston method. *J. Chem. Phys.*, 103:4613–4621, 1995.
- [59] S. Nose and M. L. Klein. *Mol. Phys.*, 101:1055, 1983.
- [60] G. J. Martyna, D. J. Tobias, and M. L. Klein. Constant pressure molecular dynamics. *J. Chem. Phys.*, 101:4177–4189, 1994.
- [61] R. B. Gennis. *Biomembranes: Molecular structure and function*. Springer-Verlag, New York, NY, 1989.
- [62] R. E. Koeppe II, J. A. Killian, and D. V. Greathouse. Orientations of the tryptophan 9 and 11 side chains of the gramicidin channel based on ^2H NMR spectroscopy. *Biophys. J.*, 66:14–24, 1994.
- [63] R. S. Prosser, S. I. Daleman, and J. H. Davis. The structure of an integral membrane peptide: A ^2H NMR study of gramicidin. *Biophys. J.*, 66:1415–1428, 1994.

- [64] F. M. Marassi, A. Ramamoorthy, and S. J. Opella. Complete resolution of the solid-state NMR spectrum of a uniformly ^{15}N labeled membrane protein in phospholipid bilayers. *Proc. Natl. Acad. Sci. U. S. A.*, 94:8551–8556, 1997.
- [65] G. Schaftenaar and J. H. Noordik. Molden: A pre and post processing program for molecular and electronic structures. *Journal of Computer-Aided Molecular design*, 14:123–134, 2000.
- [66] R. S. Armen, O. D. Uitto, and S. E. Feller. Phospholipid component volumes: Determination and application to bilayer structure calculations. *Biophys. J.*, 75:734–744, 1998.
- [67] W. L. Jorgensen, J. Chandrasekhar, J. D. Madura, R. W. Impey, and M. L. Klein. Comparison of simple potential functions for simulating liquid water. *J. Chem. Phys.*, 79:926–935, 1983.
- [68] A. T. Brünger. *X-plor, version 3.1: A system for x-ray crystallography and NMR*. Yale University, 1992.
- [69] M. Schlenkrich, J. Brickman, A. D. MacKerell, and M. Karplus. Empirical potential energy function for phospholipids: Criteria for parameter optimization and applications. In K. M. Merz and B. Roux, editors, *Biological membranes: A molecular perspective from computation and experiment*, pages 31–81. Birkhauser, 1996.
- [70] W. Humphrey, A. Dalke, and K. Schulten. Visual molecular dynamics. *J. Mol. Graphics*, 14:33–38, 1996.
- [71] R. L. Dunbrack Jr. and M. Karplus. Backbone-dependent rotamer library for proteins: Applications to side-chain prediction. *J. Mol. Biol.*, 230:543–574, 1993.

- [72] K. Belohorcova, J. H. Davis, T. B. Woolf, and B. Roux. Structure and dynamics of an amphiphilic peptide in a lipid bilayer: A molecular dynamics study. *Biophys. J.*, 73:3039–3055, 1997.
- [73] S. A. Pandit and M. L. Berkowitz. Molecular dynamics simulation of dipalmitoylphosphatidylserine bilayer with Na⁺ counterions. *Biophys. J.*, 82:1818–1827, 2002.
- [74] E. Lindahl and O. Edholm. Mesoscopic undulations and thickness fluctuations in lipid bilayers from molecular dynamics simulation. *Biophys. J.*, 79:426–433, 2000.
- [75] W. Shinoda, N. Namiki, and S. Okazaki. Molecular dynamics study of a lipid bilayer: Convergence, structure, and long-time dynamics. *J. Chem. Phys.*, 106:5731–5743, 1997.
- [76] H. Heller, M. Schaefer, and K. Schulten. Molecular dynamics simulation of a bilayer of 200 lipids in the gel and in the liquid crystal phases. *J. Phys. Chem.*, 97:8343–8360, 1993.
- [77] M. Pasenkiewicz-Gierulaj, T. Rog, K. Kitamura, and A. Kusumi. Cholesterol effects on the phosphatidylcholine bilayer polar region: A molecular simulation study. *Biophys. J.*, 78:1376–1389, 2000.
- [78] J. F. Nagle and S. Tristram-Nagle. Structure of lipid bilayers. *Biochem. et Biophys. Acta*, pages 159–195, 2000.
- [79] J. Seelig and N. Waespe-Sarcevic. Molecular order in cis and trans unsaturated phospholipid bilayers. *Biochem.*, 17:3310–3315, 1979.
- [80] S. O. Smith, C. S. Smith, and B. J. Bormann. Strong hydrogen bonding interactions involving a buried glutamic acid in the transmembrane domain of the neu/erbB-2 receptor. *Nature Struct. Biol.*, 3:252–258, 1996.

- [81] W. P. Russ and D. M. Engelman. The GxxxG motif: A framework for transmembrane helix-helix association. *J. Mol. Biol.*, 296:911–919, 2000.
- [82] J-P Duneau, N. Garnier, and M. Genest. Insight into signal transduction: Structural alterations in transmembrane helices probed by multi-1 ns molecular dynamics simulations. *J. Biomol. Struct*, 15:555–572, 1997.
- [83] J. P. Duneau, S. Crouzy, Y. Chapron, and M. Genest. Dynamics of the transmembrane domain of the erbB-2 receptor. *Theor. Chem. Acc.*, 101:87–91, 1999.
- [84] N. Sajot, N. Garnier, and M. Genest. Dimer models for erbB-2/neu transmembrane domains from molecular dynamics simulations. *Theor. Chem. Acc.*, 101:67–72, 1999.
- [85] N. Sajot and M. Genest. Structure prediction of the dimeric neu/erbB-2 transmembrane domain from multi-nanosecond molecular dynamics simulations. *Eur. Biophys. J.*, 28:648–662, 2000.
- [86] J-P Duneau, S. Crouzy, N. Garnier, Y. Chapron, and M. Genest. Molecular dynamics simulations of the erbB-2 transmembrane domain within an explicit membrane environment: Comparison with vacuum simulations. *Biophys. Chem.*, 76:35–53, 1999.
- [87] S. O. Smith, D. Song, S. Shekar, M. Groesbeek, M. Ziliox, and S. Aimoto. Structure of the transmembrane dimer interface of glycoporphin A in membrane bilayers. *Biochem.*, 40:6553–6558, 2001.
- [88] A. Senes, M. Gerstein, and D. M. Engelman. Statistical analysis of amino acid patterns in transmembrane helices: The GxxxG motif occurs frequently and in association with β -branched residues. *J. Mol. Biol.*, 296:921–936, 2000.

- [89] B. J. Bormann, W. J. Knowles, and V. T. Marchesi. Synthetic peptides mimic the assembly of transmembrane glycoproteins. *J. Biol. Chem.*, 264:4033–4037, 1989.
- [90] M. A. Lemmon, J. M. Flanagan, H. R. Treutlein, J. Zhang, and D. M. Engelman. Synthetic peptides mimic the assembly of transmembrane glycoproteins. *Biochem.*, 31:12719–12725, 1992.
- [91] A. Senes, M. Gerstein, and D. M. Engelman. Statistical analysis of amino acid patterns in transmembrane helices: The GxxxG motif occurs frequently and in association with β -branched residues at neighboring positions. *J. Mol. Biol.*, 296:921–936, 2000.
- [92] S. O. Smith, M. Eilers, D. Song, E. Crocker, W. Ying, M. Groesbeek, G. Metz, M. Ziliox, and S. Aimoto. Implications of threonine hydrogen bonding in the glycophorin A transmembrane helix dimer. *Biophys. J.*, 82:2476–2486, 2002.
- [93] M. A. Lemmon, J. M. Flanagan, H. R. Treutlein, J. Zhang, and D. M. Engelman. Sequence specificity in the dimerization of transmembrane α -helices. *Biochem.*, 31:12719–12725, 1992.
- [94] H. I. Petrache, A. Grossfield, K. R. MacKenzie, D. M. Engelman, and T. B. Wolf. Modulation of glycophorin A transmembrane helix interactions by lipids bilayers: Molecular dynamics calculations. *J. Mol. Biol.*, 302:727–746, 2000.
- [95] D. Park. *Introduction to quantum theory*. McGraw-Hill, 1992.

Appendix A. NMR Theory

The Classical Description of NMR

An explanation of the NMR phenomenon is presented in this section using a classical description. The classical point of view is often used to describe the bulk magnetization in a spin system. Additionally, the classical description can be used to easily describe the action of a radio frequency (RF) field on the bulk magnetization.

When a magnetic dipole is placed in a magnetic field it experiences a torque and precesses about the z direction, which is described by [28]

$$\frac{d\vec{\mu}}{dt} = \vec{\mu} \times \gamma \vec{H}_0. \quad (\text{A.1})$$

The frequency of precession is often referred to as the Larmor frequency [27, 29], given by γH_0 , where γ is defined as the gyromagnetic ratio [29]. Since γ is a quantity which is dependent on the type of nucleus, then the precession frequency or Larmor frequency (*i.e.* γH_0) is unique for differing magnetic nuclei [29]. A solution to this differential equation can be written as

$$\begin{aligned} \vec{\mu} &= \mu_x \mathbf{i} + \mu_y \mathbf{j} + \mu_z \mathbf{k} \\ &= |\vec{\mu}_i| (\cos(\gamma H_0 t + \phi) \mathbf{i} - \sin(\gamma H_0 t + \phi) \mathbf{j} + \cos \theta \mathbf{k}) \end{aligned} \quad (\text{A.2})$$

where ϕ is the phase of the dipole precession about the z axis. If we consider a system of dipoles at equilibrium there will be a random distribution of phases [30] for dipole components in the x - y plane so that a vector summation over all of the dipoles is expected to give no net contribution perpendicular to the applied field. However,

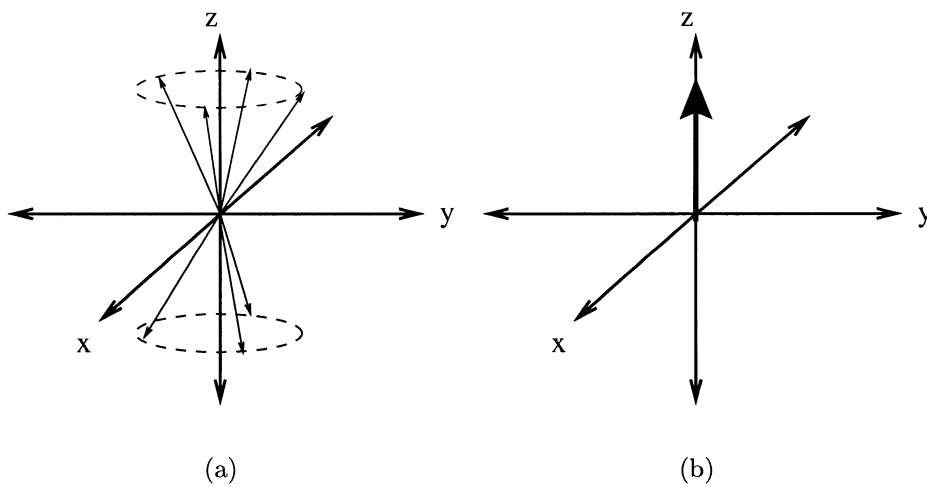


Figure A.1: Net magnetization in the NMR experiment. (a) In a static magnetic field dipoles will precess about the field direction. The z component of the dipole is aligned parallel or anti-parallel to static field direction. (b) An ensemble of spins will exhibit a random distribution of phases leading to a net equilibrium magnetization aligned along the field direction.

the favorable alignment of the dipoles along the field direction will result in a net magnetization \vec{M} along the z direction. This is illustrated in Figure A.1. Since the magnetization is proportional to a summation over all dipoles in the system [31], which is just a measure of the average dipole, then it follows that the magnetization also obeys an equation similar to Equation A.1. Consequently [27],

$$\frac{d\vec{M}}{dt} = \vec{M} \times \gamma \vec{H}_0 \quad (\text{A.3})$$

which describes the precession of magnetization about the direction of the applied field at the Larmor frequency. Since the magnetization is initially aligned along the z direction then $\frac{d\vec{M}}{dt} = 0$ at equilibrium.

Obtaining information about the spin environment and molecular motions/structure is achieved by manipulation of the net magnetization through the use of short duration RF pulses. In the NMR experiment a sample is placed in a conductive coil. The coil axis is oriented perpendicular to the static field direction and an alternating current is applied to the coil. This produces a linearly polarized oscillating magnetic field of the form $\vec{H}_{RF} = 2H_1 \cos(\Omega t)\mathbf{i}$ [28, 29] oriented along the coil axis which is arbitrarily set to the \mathbf{i} -direction. A linearly polarized oscillating magnetic field can be decomposed into two counter rotating circularly polarized components [28]. The field can be written

$$\vec{H}_{1+}(t) = H_1(\cos(\Omega t)\mathbf{i} + \sin(\Omega t)\mathbf{j}), \quad (\text{A.4})$$

and

$$\vec{H}_{1-}(t) = H_1(\cos(\Omega t)\mathbf{i} - \sin(\Omega t)\mathbf{j}) \quad (\text{A.5})$$

where H_1 is the field strength, and $\vec{H}_{1+}(t)$ and $\vec{H}_{1-}(t)$ describe time varying right and left circularly polarized components respectively. Applying a rotation of coordinates

by an angle Ωt about the \mathbf{k} -axis in the laboratory frame yields

$$\begin{aligned}\vec{H}'_{1-}(t) &= \begin{pmatrix} \cos \Omega t & \sin \Omega t & 0 \\ -\sin \Omega t & \cos \Omega t & 0 \\ 0 & 0 & 1 \end{pmatrix} \begin{pmatrix} H_1 \cos \Omega t \\ H_1 \sin \Omega t \\ 0 \end{pmatrix} \\ &= H_1 \mathbf{i}'\end{aligned}\tag{A.6}$$

This illustrates that the right circularly polarized component is stationary in a frame of reference rotating with frequency Ω with respect to the stationary laboratory frame. This frame of reference is commonly referred to as the “rotating frame” [29]. Using the same rotation matrix one can show that the left circularly polarized component becomes

$$\vec{H}'_{1+}(t) = H_1(\cos(2\Omega t)\mathbf{i}' - \sin(2\Omega t)\mathbf{j}').\tag{A.7}$$

With respect to the rotating frame this component oscillates in the \mathbf{i}' - \mathbf{j}' plane with frequency 2Ω . The time average of this component is effectively zero over one cycle so hereafter we consider only the component which is right circularly polarized, \vec{H}_{RF} , written as [27, 29]

$$\vec{H}_{RF} = H_1(\cos(\Omega t)\mathbf{i} + \sin(\Omega t)\mathbf{j})\tag{A.8}$$

in the laboratory frame of reference. One should note that by writing $-\Omega$ in place of Ω gives the left circularly polarized component.

In order to describe the effect of RF radiation on the system magnetization, it requires that we re-evaluate the equation of motion of the magnetization in terms of the rotating frame of reference. We start by considering a frame of reference with three mutually orthogonal axes x' , y' , and z' , with unit vectors \mathbf{i}' , \mathbf{j}' , and \mathbf{k}' rotating with angular velocity $\vec{\Omega}$ about the z' axis, which coincides with the z axis of the laboratory frame [29]. The time derivative of magnetization is [28]

$$\frac{d\vec{M}}{dt} = \left(\frac{d\vec{M}}{dt} \right)_{rot} + M_x \frac{d\mathbf{i}'}{dt} + M_y \frac{d\mathbf{j}'}{dt} + M_z \frac{d\mathbf{k}'}{dt}.\tag{A.9}$$

where $\left(\frac{d\vec{M}}{dt}\right)_{rot}$ is the rate of change of \vec{M} in the rotating frame and M_x , M_y , and M_z are the components of the magnetization. Since the time derivative of the unit vector is

$$\frac{d\mathbf{i}'}{dt} = \vec{\Omega} \times \mathbf{i}',$$

then the time derivative of magnetization can be written as

$$\frac{d\vec{M}}{dt} = \left(\frac{d\vec{M}}{dt}\right)_{rot} + \vec{\Omega} \times \vec{M}. \quad (\text{A.10})$$

Using Equation A.3,

$$\left(\frac{d\vec{M}}{dt}\right)_{rot} + \vec{\Omega} \times \vec{M} = \vec{M} \times \gamma \vec{H}_0. \quad (\text{A.11})$$

Rewriting Equation A.3 the time derivative of \vec{M} in the rotating frame of reference is

$$\begin{aligned} \left(\frac{d\vec{M}}{dt}\right)_{rot} &= \vec{M} \times \gamma \left(\vec{H}_0 + \frac{\vec{\Omega}}{\gamma}\right) \\ &= \vec{M} \times \gamma \vec{H}_{eff}. \end{aligned} \quad (\text{A.12})$$

In the presence of an RF pulse rotating with frequency Ω Eq. A.12 may be written as

$$\left(\frac{d\vec{M}}{dt}\right)_{rot} = \vec{M} \times \gamma \left(\left(H_0 + \frac{\Omega}{\gamma}\right) \mathbf{k}' + H_1 \mathbf{i}' \right) \quad (\text{A.13})$$

where we have used the fact that both \vec{H}_0 and $\vec{\Omega}$ are parallel to the z' direction of the rotating frame to obtain this result and the RF pulse is parallel to the x' axis in the rotating frame as described by Equation A.6. At resonance $H_0 + \frac{\Omega}{\gamma} \approx 0$ so the static magnetic field drops out of the equations of motion of the magnetization [29]. In a frame rotating at the Larmor frequency, the only field experienced by the magnetization is H_1 which lies along the \mathbf{i}' axis, perpendicular to the z direction. This will cause the magnetization to precess (about H_1) with angular frequency γH_1 as illustrated in Figure A.2. The desired angle of rotation is achieved by letting the magnetization precess about H_1 for a short period of time. After turning off the RF pulse

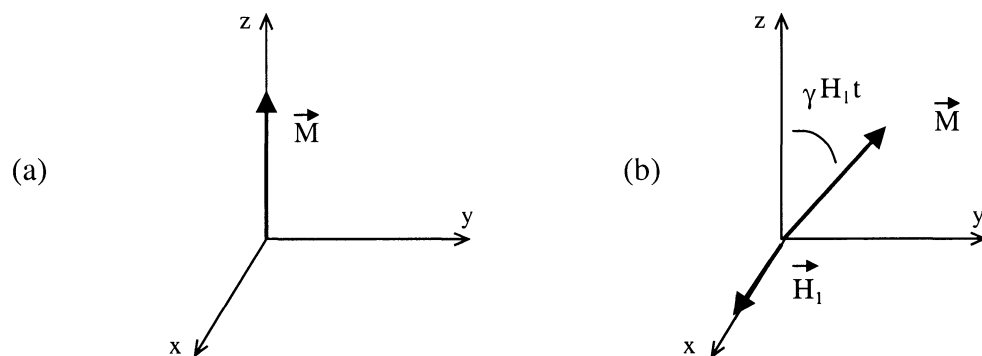


Figure A.2: The effect of an RF pulse on equilibrium magnetization. (a) Magnetization at equilibrium. (b) Application of an RF pulse for a time t causes the magnetization to tip away from the z axis by an amount $\gamma H_1 t$.

the magnetization precesses freely about the static magnetic field in the laboratory frame according to Eq. A.3 [29]. During free precession of the magnetization, the changing magnetic flux induces an emf in the coil surrounding the sample which can be measured using a NMR spectrometer. A further description of the signal detection process and details concerning the operation of the NMR spectrometer are described in Chapter 4.

For spin- $\frac{1}{2}$ particles this classical description provides a complete picture of the evolution of a spin system under the influence of an RF field [27]. However, for deuterons, which are spin-1 particles, the picture is a little more complicated due to the presence of three possible spin orientations and the interaction of electric fields with the deuteron quadrupole moment. Therefore, the equations of motion for the net magnetization which have been formulated here using the classical description need to be further extended using the density matrix approach which provides a complete picture of the evolution of system magnetization. Before the density matrix is introduced, a description of the NMR phenomenon using quantum mechanics is presented.

The Quantum Description of NMR

The Zeeman Interaction

The NMR phenomenon is a direct result of the quantum spin angular momentum of the nucleus. The spin angular momentum of an atomic nucleus results in a dipole moment and the magnetic dipole operator for a single spin can be written as [26]

$$\begin{aligned}\hat{\boldsymbol{\mu}} &= \gamma\hbar\hat{\boldsymbol{I}} \\ &= \gamma\hbar(\hat{I}_x\mathbf{i} + \hat{I}_y\mathbf{j} + \hat{I}_z\mathbf{k})\end{aligned}\tag{A.14}$$

where \hbar is Planck's constant divided by 2π and $\hat{\boldsymbol{I}}$ is the nuclear spin operator. For an isolated dipole moment interacting with a static magnetic field oriented along the

z direction, the Hamiltonian is given by [27, 28]

$$\begin{aligned}\hat{H}_Z &= -\hat{\vec{\mu}} \cdot \vec{H}_0 \\ &= -\gamma\hbar\vec{H}_0\hat{I}_z\end{aligned}\tag{A.15}$$

Substituting the eigenvector $|m\rangle$ of the operator \hat{I}_z into the Schrödinger equation yields

$$-\gamma\hbar H_0\hat{I}_z|m\rangle = -\gamma\hbar H_0 m|m\rangle\tag{A.16}$$

where $m = -I, -I + 1 \dots I$ and I is the nuclear spin quantum number [27].

The deuteron has a spin of 1 so the eigenvalues lead to $m = \pm 1, 0$ and the energy eigenvalues are given by

$$E_1 = -\gamma\hbar H_0, \quad E_0 = 0, \quad E_{-1} = \gamma\hbar H_0.\tag{A.17}$$

The application of a static magnetic field splits the degenerate spin energy level into three eigenstates referred to as Zeeman levels (See Figure A.3). These levels describe the alignment of the magnetic dipole with respect to the applied static field direction. The energy difference between the Zeeman levels is $\hbar\omega_0$ where $\omega_0 = \gamma H_0$ is the just the Larmor precession frequency presented earlier in the classical explanation of the NMR phenomenon. This energy difference is typically small and transitions may be induced between the energy levels using radio RF radiation [29]. Inducing transitions between the nuclear spin states corresponds to a change in the orientation of the z component of the nuclear spin.

The relative populations of the Zeeman levels is governed by Boltzmann statistics. In terms of the partition function Z for the system, the population of energy level E_m is

$$p(E_m) = \frac{e^{-\frac{E_m}{k_b T}}}{Z}.\tag{A.18}$$

In the high temperature approximation we can expand the exponential using a Taylor series which gives

$$p(E_{-1}) = \frac{1}{3} \left(1 + \frac{\hbar\omega_0}{k_b T} \right), \quad p(E_0) = \frac{1}{3}, \quad p(E_1) = \frac{1}{3} \left(1 - \frac{\hbar\omega_0}{k_b T} \right)\tag{A.19}$$

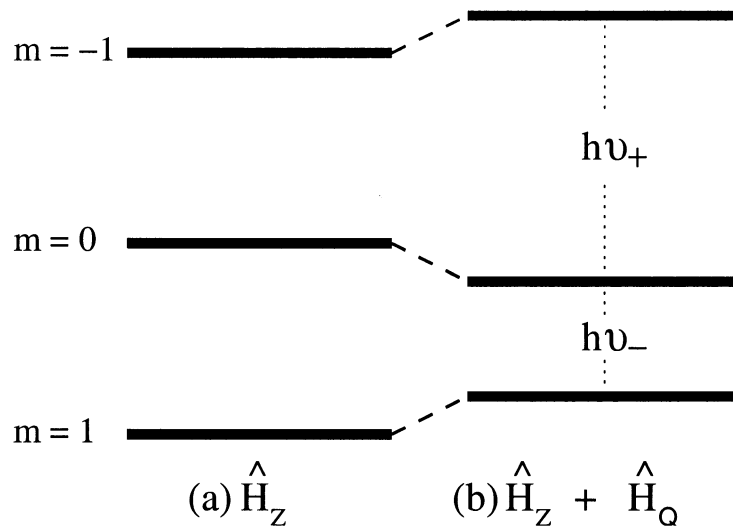


Figure A.3: Zeeman splitting of nuclear spin energy levels. (a) When placed in a static magnetic field the degenerate $I = 1$ state splits into three energy states that describe the orientation of the magnetic dipole in the magnetic field. (b) For a deuteron the Zeeman energy levels are shifted by the quadrupolar interaction.

for the populations for the Zeeman levels [30]. Since the energy difference (*i.e.* $\hbar\omega_0$) between levels is small compared to k_bT this leads to an excess of approximately one in 10^8 spins occupying the lower energy level where the z component of the dipoles are aligned with the magnetic field direction. This population difference leads the presence of equilibrium magnetization. From the expectation value of the z component of the dipole operator, $\langle \hat{\mu}_z \rangle = \gamma \hbar m$, the statistical average of the z component of the nuclear dipole is [31]

$$\bar{\mu}_z = \sum_m \gamma \hbar m p(E_m) \quad (\text{A.20})$$

and the summation is over the possible spin orientations. Upon substitution of $p(E_m)$ into the above equation we have,

$$\bar{\mu}_z = \frac{2\gamma^2 \hbar^2}{3k_B T} H_0. \quad (\text{A.21})$$

Since the magnetization is proportional to the average dipole moment then [27]

$$\begin{aligned} M_z &= N \bar{\mu}_z \\ &= \frac{2N\gamma^2 \hbar^2}{3k_B T} H_0 \end{aligned} \quad (\text{A.22})$$

where N is the number of spins in the system. Due to the difference in populations of the spin states, the system has non-zero equilibrium magnetization which is analogous to the classical description for a system of dipoles.

The Connection with Classical Mechanics

The quantum picture provides a convenient way to describe magnetic dipole transitions in the NMR spin system and provides a description of the presence of equilibrium magnetization resulting from the population difference between the Zeeman states. In order to illustrate the connection between the quantum and classical pictures we consider the expectation values of the components of the nuclear dipole and show that they behave as classical vector quantities.

The time dependent Schrödinger equation for a nucleus in an arbitrary state $|\psi\rangle$ can be written as [95]

$$-\frac{\hbar}{i} \frac{\partial |\Psi\rangle}{\partial t} = E|\Psi\rangle. \quad (\text{A.23})$$

The solution to this time dependent equation,

$$|\Psi\rangle = \sum_m a_m |m\rangle e^{-i\frac{E_m}{\hbar}t}, \quad (\text{A.24})$$

provides a description of the spin system through an expansion with complex expansion coefficients a_m and orthonormal basis or state vectors, $|m\rangle$, which define spin orientation [28]. Using Equation A.14 and A.24, the expectation value of the x component of the dipole operator can be written as

$$\begin{aligned} \langle \hat{\mu}_x \rangle &= \langle \Psi | \hat{\mu}_x | \Psi \rangle \\ &= \gamma \hbar \sum_{m,m'} a_m^* a_{m'} \langle m | \hat{I}_x | m' \rangle e^{i\frac{E_m - E_{m'}}{\hbar}t}, \end{aligned} \quad (\text{A.25})$$

in a manner similar to Slichter [28]. Using the definition for raising and lowering operators, \hat{I}_+ and \hat{I}_- respectively, \hat{I}_x can be written as [27, 33]

$$\hat{I}_x = \frac{1}{2}(\hat{I}_+ + \hat{I}_-).$$

Further simplification follows through substitution of $E_m - E_{m'} = \gamma H_0$ for the energy difference between Zeeman levels. Using the properties of the raising and lowering operators [95] leads to vanishing diagonal elements (ie $m = m'$) leaving [28]

$$\begin{aligned} \langle \hat{\mu}_x \rangle &= \gamma \hbar (a_0^* a_1 \langle 0 | \hat{I}_x | 1 \rangle e^{-i\frac{\gamma H_0}{\hbar}t} + a_0 a_1^* \langle 1 | \hat{I}_x | 0 \rangle e^{i\frac{\gamma H_0}{\hbar}t}) \\ &\quad + a_0^* a_{-1} \langle 0 | \hat{I}_x | -1 \rangle e^{-i\frac{\gamma H_0}{\hbar}t} + a_0 a_{-1}^* \langle -1 | \hat{I}_x | 0 \rangle e^{i\frac{\gamma H_0}{\hbar}t}. \end{aligned} \quad (\text{A.26})$$

The expansion coefficients are complex numbers which can be expressed using the notation of Slichter by [28],

$$a_1 = b e^{i\beta}, \quad a_0 = a e^{i\alpha}, \quad a_{-1} = c e^{i\delta} \quad (\text{A.27})$$

where α , β , and δ are phase factors. Using the raising and lowering operator definition of \hat{I}_x [28], $\langle 0|\hat{I}_x|1\rangle = \sqrt{2}$ and $\langle 0|\hat{I}_x|-1\rangle = \sqrt{2}$. The same definition holds for the complex conjugates of these matrix elements. Finally, after some algebraic manipulation, Equation A.26 can be written as

$$\langle \hat{\mu}_x \rangle = \gamma \hbar \sqrt{2} (ab \cos(\gamma H_0 t + \alpha - \beta) + ac \cos(\gamma H_0 t + \delta - \alpha)) \quad (\text{A.28})$$

In a similar manner the expectation values $\langle \hat{\mu}_y \rangle$ and $\langle \hat{\mu}_z \rangle$ can be determined and are given by

$$\langle \hat{\mu}_y \rangle = \gamma \hbar \sqrt{2} (ab \sin(\gamma H_0 t + \alpha - \beta) + ac \sin(\gamma H_0 t + \delta - \alpha)) \quad (\text{A.29})$$

and

$$\langle \hat{\mu}_z \rangle = \gamma \hbar (a^2 - b^2). \quad (\text{A.30})$$

The x and y components of the nuclear dipole precess about the z direction with an angular frequency γH_0 which is precisely the Larmor frequency while the z component remains constant. This result illustrates that the expectation values of the components of the dipole moment behave as classical vector quantities.

Equations A.28 through A.30 illustrate the classical nature of a quantum dipole in a magnetic field. Using the above equations one can construct the equation of motion of the dipole vector. However, rather than present a derivation based on the above result, the classical equation of motion can be derived by starting with the Liouville equation. The time evolution of an arbitrary operator \hat{O} evolves in time under the influence of a Hamiltonian \hat{H} according to [32]

$$\frac{d\hat{O}}{dt} = \frac{i}{\hbar} [\hat{H}, \hat{O}]. \quad (\text{A.31})$$

Under the influence of the Zeeman interaction, the time evolution of the x component of the nuclear spin operator can then be written as [28]

$$\frac{d\hat{I}_x}{dt} = \frac{i}{\hbar} \gamma \hbar H_0 [\hat{I}_z, \hat{I}_x] \quad (\text{A.32})$$

The commutation relations for components of angular momentum [28, 95] can be used to simplify the previous equation. Substituting $[\hat{I}_z, \hat{I}_x] = -i\hat{I}_y$ Equation A.32 becomes

$$\frac{d\hat{I}_x}{dt} = \gamma H_0 \hat{I}_y. \quad (\text{A.33})$$

The time evolution of \hat{I}_y and \hat{I}_z are also determined in this manner and are [28]

$$\frac{d\hat{I}_y}{dt} = -\gamma H_0 \hat{I}_x \quad (\text{A.34})$$

and

$$\frac{d\hat{I}_z}{dt} = 0. \quad (\text{A.35})$$

Equation A.35 illustrates that the z component of spin angular momentum is a conserved quantity. Using the above equations which represent the time evolution of the components of the nuclear spin operator, the vector operator equation can be represented by

$$\frac{d\hat{\vec{I}}}{dt} = \hat{\vec{I}} \times \gamma \vec{H}_0, \quad (\text{A.36})$$

and from the definition of the nuclear dipole presented in Equation A.14, the preceding equation leads to the expectation value of dipole moment [28],

$$\frac{d\langle \hat{\vec{\mu}} \rangle}{dt} = \langle \hat{\vec{\mu}} \rangle \times \gamma \vec{H}_0 \quad (\text{A.37})$$

which describes the precession of an isolated magnetic dipole moment about the direction of the applied magnetic field with frequency γH_0 .

In this section it was shown that the quantum mechanical description of NMR leads to a classical equation of motion for a magnetic dipole moment in a static magnetic field. Both the quantum and classical pictures provide a detailed picture of the NMR phenomenon. The quantum description provides detail concerning the spin energy levels and the populations of the spin energy states while the classical picture provides a visual picture of the precessing spins and the bulk magnetization. Together, both descriptions can be used to understand the effect of RF pulses on the spin system. In order to further develop the ideas presented here, a more detailed picture of the behavior of RF pulses is explored in the next section.

The Hamiltonian of a RF Field

The Hamiltonian of a nuclear dipole in the laboratory frame in the presence of a static magnetic field and an applied RF pulse is given by

$$\begin{aligned}\hat{H} &= \hat{H}_Z + \hat{H}_{RF} \\ &= -\hat{\boldsymbol{\mu}} \cdot (\vec{H}_0 + \vec{H}_{RF}).\end{aligned}\tag{A.38}$$

Substitution of expression A.8 into the above equation yields [28]

$$\hat{H} = -\gamma\hbar H_0 \hat{I}_z - \gamma\hbar H_1 \hat{I}_x \cos(\Omega t) + \gamma\hbar H_1 \hat{I}_y \sin(\Omega t)\tag{A.39}$$

which is a logical extension of the static field Hamiltonian presented in Equation A.15.

However, the term

$$\hat{I}_x \cos(\Omega t) + \hat{I}_y \sin(\Omega t)$$

in this equation describes the rotation of an operator, in the plane subtended by \hat{I}_x and \hat{I}_y , about the z axis and can be written in terms of a unitary transformation [32].

Using the unitary transformation [28, 33]

$$e^{-i\Omega t \hat{I}_z} \hat{I}_x e^{i\Omega t \hat{I}_z} = \hat{I}_x \cos(\Omega t) + \hat{I}_y \sin(\Omega t)$$

Equation A.39 can be written as

$$\hat{H} = -\gamma\hbar H_0 \hat{I}_z - \gamma\hbar H_1 e^{-i\Omega t \hat{I}_z} \hat{I}_x e^{-i\Omega t \hat{I}_z}.\tag{A.40}$$

The wavefunction Ψ describing the nuclear state in the laboratory frame can also be described in terms of a unitary transformation of the wavefunction in a frame of reference rotating with an angular velocity $\vec{\Omega} = \Omega \mathbf{k}$ where the z' axis coincides with the z axis of the laboratory frame. Rotation of the scalar wavefunction can be written as

$$|\Psi\rangle = e^{-i\Omega t \hat{I}_z} |\Psi'\rangle\tag{A.41}$$

where $|\Psi'\rangle$ is the wavefunction in the rotating frame of reference [27]. Substituting Equations A.40 and A.41 into the Schrödinger equation leads to the Hamiltonian in

the rotating frame of reference. In a frame of reference rotating with the frequency of the applied RF (*i.e.* Ω) the Hamiltonian [27, 28]

$$\hat{H} = -\gamma\hbar \left(\frac{\Omega}{\gamma} + H_0 \right) \hat{I}_z - \gamma\hbar H_1 \hat{I}_x \quad (\text{A.42})$$

which consists of two parts. The first term is the Zeeman Hamiltonian in the rotating frame (*i.e.* \hat{H}'_Z) and the second term is the RF Hamiltonian in the rotating frame (*i.e.* \hat{H}'_{RF}). The resonance condition is satisfied when $\Omega = -\gamma H_0$ and then Equation A.42 reduces to

$$\hat{H} = -\gamma\hbar H_1 \hat{I}_x. \quad (\text{A.43})$$

In a frame of reference rotating at the Larmor frequency the nuclear spin interacts solely with the applied RF field. Since \hat{I}_x can be written as a linear combination of raising and lowering operators then the action of this Hamiltonian is to change the orientation of the z component of nuclear spin. It should be noted that application of a pulse along the y direction of the rotating frame gives the Hamiltonian $-\gamma\hbar H_1 \hat{I}_y$.

Quantum Statistical Description of NMR

The Density Matrix

In reality an ensemble of nuclear spins undergoes transitions between the spin states upon application of an RF pulse. As presented in the previous section (The Quantum Description of NMR) the populations of the Zeeman levels are governed by Boltzmann statistics. The net magnetization resulting from alignment of spins along the direction of the applied static field is proportional to the difference in the populations of spins occupying the spin states. In this section the density matrix is introduced and will be used to illustrate the presence of equilibrium magnetization in the system. NMR may be considered a problem in nonequilibrium quantum statistical mechanics. In NMR, quantum systems are typically composed of $\approx 10^{23}$ particles [30]. Solutions of the Schrödinger equation for the quantum system are impossible and we never

have a complete specification of the quantum system [30]. Instead, observables are calculated using quantum statistical averages.

Using a quantum statistical approach the expectation value of an operator \hat{O} is given by

$$\langle \hat{O} \rangle = \langle \Psi | \hat{O} | \Psi \rangle. \quad (\text{A.44})$$

where $|\Psi\rangle$ describes the state of a nuclear spin system and is given by

$$|\Psi\rangle = \sum_n a_n(t) |n\rangle. \quad (\text{A.45})$$

which is a solution to the time dependent Schrödinger equation since $|n\rangle$ describe the nuclear spin states. Using Equation A.45 for the arbitrary state of a nuclear spin, Equation A.44 can be written as [95]

$$\langle \hat{O} \rangle = \sum_{m,n} a_m^*(t) a_n(t) \langle m | \hat{O} | n \rangle. \quad (\text{A.46})$$

By taking an ensemble average, the density matrix elements are defined as

$$\langle n | \hat{\rho} | m \rangle = \overline{a_m^*(t) a_n(t)} \quad (\text{A.47})$$

where $\hat{\rho}$ is the density operator. Substituting the previous equation into Equation A.46 and using $\sum_m |m\rangle \langle m| = 1$ the expectation value can be written as

$$\begin{aligned} \langle \hat{O} \rangle &= \sum_{nm} \langle n | \hat{\rho} | m \rangle \langle m | \hat{O} | n \rangle \\ &= \sum_{nm} \langle n | \hat{\rho} | m \rangle \langle m | \hat{O} | n \rangle \\ &= \sum_n \langle n | \hat{\rho} \hat{O} | n \rangle \\ &= \text{Tr}(\hat{\rho} \hat{O}) \end{aligned} \quad (\text{A.48})$$

From Equation A.47 we can write the diagonal elements of the density matrix as

$$\langle n | \hat{\rho} | n \rangle = \overline{|a_n(t)|^2}. \quad (\text{A.49})$$

In this equation $\overline{|a_n(t)|^2}$ is just the quantum mechanical probability that the ensemble is in state n . The diagonal elements of the density matrix are the equilibrium populations of the eigenstates. Off diagonal terms will have the form [30]

$$a_m^*(t)a_n(t) = |a_m(t)||a_n(t)|e^{i(\beta_n - \alpha_m)}. \quad (\text{A.50})$$

The exponential term is a phase factor. If we assume a random distribution of spin phases at equilibrium and perform an ensemble average, that is,

$$\overline{a_m^*(t)a_n(t)} = \overline{|a_m(t)||a_n(t)|e^{i(\beta_n - \alpha_m)}} \quad (\text{A.51})$$

then all off diagonal elements of the density matrix will be zero at equilibrium [30].

Now that we have a description of the density matrix and how it can be used to calculate statistical averages of observable quantities, the next step is to develop an equation which describes the time evolution of the density operator. We begin by considering Equation A.45 which is a solution of the time dependent Schrödinger equation for a system in some arbitrary state. Substituting this equation into the time dependent Schrödinger equation yields

$$\begin{aligned} -\frac{\hbar}{i} \frac{d\Psi}{dt} &= \hat{H}\Psi \\ -\frac{\hbar}{i} \sum_n \frac{da_n(t)}{dt} |n\rangle &= \sum_n a_n(t) \hat{H}|n\rangle. \end{aligned} \quad (\text{A.52})$$

If we project the state $|k\rangle$ onto the the above equation and use the properties of these orthonormal vectors (*i.e.* $\langle n|m\rangle = \delta_{nm}$) then we can write [28, 30],

$$\begin{aligned} -\frac{\hbar}{i} \sum_n \frac{da_n(t)}{dt} \langle k|n\rangle &= \sum_n a_n(t) \langle k|\hat{H}|n\rangle \\ \frac{da_k(t)}{dt} &= -\frac{i}{\hbar} \sum_n a_n(t) \langle k|\hat{H}|n\rangle, \end{aligned} \quad (\text{A.53})$$

which relates the rate of change of $a_k(t)$ in terms of the system interaction Hamiltonian. We now consider the time derivative of the product of two time dependent

amplitudes, $a_n(t)$ and $a_m(t)$, associated with the state vectors $|n\rangle$ and $|m\rangle$ respectively. This can be written as [28]

$$\frac{d}{dt}a_n(t)a_m^*(t) = \frac{da_n(t)}{dt}a_m^*(t) + a_n(t)\frac{da_m^*(t)}{dt} \quad (\text{A.54})$$

and using the result obtained in Equation A.53,

$$\begin{aligned} \frac{d}{dt}a_n(t)a_m^*(t) &= -\frac{i}{\hbar} \sum_k a_k(t)a_m^*(t)\langle n|\hat{H}|k\rangle + \frac{i}{\hbar} \sum_k a_n(t)a_k^*(t)\langle k|\hat{H}|m\rangle \\ &= -\frac{i}{\hbar} \sum_k \left(\langle n|\hat{H}|k\rangle a_k(t)a_m^*(t) - a_n(t)a_k^*(t)\langle k|\hat{H}|m\rangle \right) \end{aligned} \quad (\text{A.55})$$

By averaging over the whole ensemble [30]

$$\frac{d}{dt}\overline{a_n(t)a_m^*(t)} = -\frac{i}{\hbar} \sum_k \left(\langle n|\hat{H}|k\rangle \overline{a_k(t)a_m^*(t)} - \overline{a_n(t)a_k^*(t)}\langle k|\hat{H}|m\rangle \right), \quad (\text{A.56})$$

and since $\overline{a_k(t)a_m^*(t)} = \langle k|\hat{\rho}|m\rangle$ then

$$\begin{aligned} \frac{d}{dt}\langle n|\hat{\rho}|m\rangle &= -\frac{i}{\hbar} \sum_k \left(\langle n|\hat{H}|k\rangle\langle k|\hat{\rho}|m\rangle - \langle n|\hat{\rho}|k\rangle\langle k|\hat{H}|m\rangle \right) \\ &= -\frac{i}{\hbar}\langle n|\hat{H}\hat{\rho} - \hat{\rho}\hat{H}|m\rangle \end{aligned} \quad (\text{A.57})$$

where we have used the definition $\sum_k |k\rangle\langle k| = 1$. Finally, from Equation A.57 we can deduce the Liouville equation given by [30]

$$\frac{d\hat{\rho}}{dt} = -\frac{i}{\hbar}[H, \hat{\rho}] \quad (\text{A.58})$$

which describes the time evolution of the density operator under the influence of an interaction Hamiltonian \hat{H} . This equation provides a starting point for investigation of the time evolution of a spin-1 system of particles. Before we consider the time evolution of the density matrix we must define the density operator based on equilibrium conditions

Equilibrium Magnetization

In order to define a starting configuration for the spin-1 system, we consider the equilibrium density operator. This is determined by considering the Boltzmann distribution for populations of the Zeeman states. Neglecting the perturbation to the Zeeman levels by the quadrupolar interaction the equilibrium density operator is [28]

$$\hat{\rho} = \frac{e^{-\frac{\hat{H}_Z}{k_B T}}}{Z}. \quad (\text{A.59})$$

Using the definition of the Zeeman Hamiltonian, given by Equation A.15, to simplify expression A.59 and then expanding the exponential we can write

$$\begin{aligned} \hat{\rho} &= \frac{e^{\frac{\gamma \hbar H_0 \hat{I}_z}{k_B T}}}{Z} \\ &= \frac{1}{Z} \left(1 + \frac{\gamma \hbar H_0 \hat{I}_z}{k_B T} \right) \end{aligned} \quad (\text{A.60})$$

assuming that the high temperature approximation is valid. By treating the spins as Boltzmann particles, the partition function for the system is [31, 50]

$$\begin{aligned} Z &= \sum_m e^{-\frac{E_m}{k_B T}} \\ &= e^{-\frac{E_{-1}}{k_B T}} + e^{-\frac{E_0}{k_B T}} + e^{-\frac{E_1}{k_B T}} \end{aligned} \quad (\text{A.61})$$

where E_m are the energy eigenvalues for the spin states defined by the state vectors $|m\rangle$ which are described in Section A.2.1. Using a Taylor series, each exponential term can be expanded at high temperatures to give

$$Z \approx 3 + O\left(\frac{E_m}{k_B T}\right) \quad (\text{A.62})$$

so that Equation A.60 can finally be written as

$$\hat{\rho} = \frac{1}{3} \left(1 + \frac{\gamma \hbar H_0 \hat{I}_z}{k_B T} \right). \quad (\text{A.63})$$

Using the properties of the density operator it is possible to calculate the quantum statistical average of some system observable. In this case we wish to illustrate the presence of equilibrium magnetization in the spin system. The total z-magnetization operator can be written as [31]

$$\begin{aligned}\widehat{M}_z &= N\hat{\mu}_z \\ &= \gamma\hbar N\hat{I}_z\end{aligned}\tag{A.64}$$

where N is the number of spins in the ensemble. Consequently, the expectation value of z-magnetization is

$$\langle\widehat{M}_z\rangle = Tr(\hat{\rho}\widehat{M}_z)\tag{A.65}$$

$$= \frac{1}{3}\left(\gamma\hbar NTr(\hat{I}_z) + \frac{\gamma^2\hbar^2 N}{k_b T}H_0Tr(\hat{I}_z^2)\right)\tag{A.66}$$

and since $Tr(\hat{I}_z) = 0$ and $Tr(\hat{I}_z^2) = I(I+1)(2I+1)/3$ [32] then the equilibrium magnetization is given by

$$\langle\widehat{M}_z\rangle = \frac{2\gamma^2\hbar^2 N}{3k_b T}H_0.\tag{A.67}$$

The quantum statistical approach leads to an equilibrium magnetization aligned along the static field direction which is given by Curie's law [26] where the susceptibility is

$$C = \frac{2\gamma^2\hbar^2 N}{3k_b}.\tag{A.68}$$

Quantum Statistical Description of the Quadrupolar Echo

The classical picture provides a description of the evolution of magnetization or coherence during the NMR experiment. From the classical point of view each individual dipole contributes to a net magnetization which can be manipulated using RF radiation. However, this picture does not suffice for a spin-1 system. Fortunately, the quantum statistical or density matrix approach does provides a complete description. A spin-1 system is best described by a space which is spanned by 9 orthogonal operators. For convenience we choose [30]

$$\begin{aligned}
\hat{O}_1 &= \frac{1}{\sqrt{2}}\hat{I}_x & \hat{O}_2 &= \frac{1}{\sqrt{2}}\hat{I}_y & \hat{O}_3 &= \frac{1}{\sqrt{2}}\hat{I}_z \\
\hat{O}_4 &= \frac{1}{\sqrt{6}}(3\hat{I}_z^2 - I^2) & \hat{O}_5 &= \frac{1}{\sqrt{2}}(\hat{I}_x\hat{I}_z + \hat{I}_z\hat{I}_x) & \hat{O}_6 &= \frac{1}{\sqrt{2}}(\hat{I}_y\hat{I}_z + \hat{I}_z\hat{I}_y) \\
\hat{O}_7 &= \frac{1}{\sqrt{2}}(\hat{I}_x^2 + \hat{I}_y^2) & \hat{O}_8 &= \frac{1}{\sqrt{2}}(\hat{I}_x\hat{I}_y + \hat{I}_y\hat{I}_x) & \hat{O}_9 &= \frac{1}{\sqrt{3}}\hat{1}
\end{aligned}$$

as the basis for our orthogonal set. It is important to note that all elements of the orthogonal set obey $Tr(\hat{O}_m\hat{O}_n) = \delta_{mn}$ [30] and are, in fact, orthonormal operators.

In section 2.3.2 we defined the equilibrium density matrix as

$$\hat{\rho} = \frac{1}{3} \left(1 + \frac{\gamma\hbar H_0}{k_B T} \hat{I}_z \right)$$

which can be rewritten in this new basis as

$$\hat{\rho} = \frac{1}{3} \left(\frac{1}{\sqrt{3}} + \frac{\sqrt{2}\gamma\hbar H_0}{k_B T} \hat{O}_3 \right).$$

Since, the observable quantities are defined by the trace of the density matrix with any of the nine orthonormal operators and $Tr(\frac{1}{\sqrt{3}}\hat{1}\hat{O}_n) = 0$ then the density operator can be rewritten in the reduced form [33]

$$\begin{aligned}
\hat{\rho} &= \frac{\gamma\hbar H_0}{3k_B T} \hat{I}_z \\
&= \frac{\sqrt{2}\gamma\hbar H_0}{3k_B T} \hat{O}_3.
\end{aligned} \tag{A.68}$$

In order to track the time evolution of the equilibrium density matrix under the influence of RF pulses we can expand in terms of the orthonormal set by writing [30],

$$\hat{\rho} = \sum_{n=1}^8 c_n(t) \hat{O}_n \tag{A.69}$$

where we have taken into account that writing the ninth operator (*i.e.* $\hat{1}$) has no affect on the final state of the density matrix. That is, the trace of any observable with this operator is zero [33].

We can think of $c_n(t)$ as the components of a vector $\hat{\rho}$ which change in time as the operator $\hat{\rho}$ rotates in this 9-D operator space under the influence of specific Hamiltonians. Substitution of this expansion of $\hat{\rho}$ into the Liouville equation and taking the trace with an operator \hat{O}_p yields,

$$\frac{dc_p(t)}{dt} = -\frac{i}{\hbar} \sum_n c_n(t) Tr(\hat{O}_n[\hat{H}, \hat{O}_p]) \quad (\text{A.70})$$

and has been readily described by Davis [30].

Now that we have a starting point we will consider the action of an RF pulse on the density operator representing the spin-1 system. We start by considering the effect of a pulse with field strength H_1 along the \hat{I}_x direction. As presented in Section A.2.3, the Hamiltonian of a pulse along the x direction is

$$\hat{H}_{RF} = -\gamma\hbar H_1 \hat{I}_x \quad (\text{A.71})$$

and if we switch to the notation for the operators \hat{O}_n then we have

$$\hat{H}_{RF} = -\sqrt{2}\hbar\omega_1 \hat{O}_1 \quad (\text{A.72})$$

where we have assumed that $\omega_1 = \gamma H_1$. Now since the density operator initially has one component along the \hat{O}_3 direction then it follows that

$$\frac{dc_3(t)}{dt} = \frac{i}{\hbar} \sum_n c_n(t) Tr(\hat{O}_n[\sqrt{2}\hbar\omega_1 \hat{O}_1, \hat{O}_3]) \quad (\text{A.73})$$

Using the commutation relations for the operators \hat{I}_x and \hat{I}_z , expression A.73 can be simplified to get [30]

$$\frac{dc_3(t)}{dt} = \omega_1 \sum_n c_n(t) Tr(\hat{O}_n \hat{O}_2) \quad (\text{A.74})$$

from which one would deduce that $n = 2$ since $Tr(\hat{O}_n \hat{O}_m) = \delta_{nm}$. Finally this equation can be written as

$$\frac{dc_3(t)}{dt} = \omega_1 c_2(t) \quad (\text{A.75})$$

and using the same arguments, one would find that the only other non-zero expression in this set of coupled differential equations is

$$\frac{dc_2(t)}{dt} = -\omega_1 c_3(t). \quad (\text{A.76})$$

The solution to this set of coupled differential equations is

$$\begin{aligned} c_2(t) &= A \cos(\omega_1 t) + B \sin(\omega_1 t) \\ c_3(t) &= C \cos(\omega_1 t) + D \sin(\omega_1 t) \end{aligned} \quad (\text{A.77})$$

and applying the conditions (ie $c_3(0) = \frac{\sqrt{2}\hbar\omega_0}{3k_B T}$, $c_2(0) = 0$ and $|\hat{\rho}| = \text{constant}$) then

$$\begin{aligned} c_2(t) &= \frac{\sqrt{2}\hbar\omega_0}{3k_B T} \sin(\omega_1 t) \\ c_3(t) &= \frac{\sqrt{2}\hbar\omega_0}{3k_B T} \cos(\omega_1 t) \end{aligned} \quad (\text{A.78})$$

so that the density operator during the pulse can be written as

$$\hat{\rho} = \frac{\sqrt{2}\hbar\omega_0}{3k_B T} \cos(\omega_1 t) \hat{O}_3 + \frac{\sqrt{2}\hbar\omega_0}{3k_B T} \sin(\omega_1 t) \hat{O}_2 \quad (\text{A.79})$$

which is equivalent to the solution for the Liouville equation where the Hamiltonian is \hat{H}_{RF} due to a pulse with a field strength of H_1 . This solution, which is just a rotation of $\hat{\rho}$ in the operator space, can be formally written as [30, 33]

$$\begin{aligned} \hat{\rho}(t) &= e^{-i\frac{\hat{H}_{RF}t}{\hbar}} \hat{\rho}(0) e^{i\frac{\hat{H}_{RF}t}{\hbar}} \\ &= e^{i\frac{\sqrt{2}\gamma\hbar H_1 \hat{O}_2 t}{\hbar}} \hat{\rho}(0) e^{-i\frac{\sqrt{2}\gamma\hbar H_1 \hat{O}_2 t}{\hbar}} \\ &= e^{i\sqrt{2}\omega_1 t \hat{O}_2} \hat{\rho}(0) e^{-i\sqrt{2}\omega_1 t \hat{O}_2} \end{aligned} \quad (\text{A.80})$$

which just describes a rotation of the density operator at $t=0$ about the operator $-\hat{O}_1$ by an angle $\omega_1 t$. So the action of the RF Hamiltonian for the pulse is to rotate the component of the operator \hat{O}_3 onto \hat{O}_2 about the operator $-\hat{O}_1$. At the end of a $\omega_1 t = 90^\circ$ pulse, the density operator is

$$\hat{\rho} = \frac{\sqrt{2}\hbar\omega_0}{3k_B T} \hat{O}_2. \quad (\text{A.81})$$

The trace of this expression with \hat{M}_x is

$$\begin{aligned} Tr \left(\frac{\sqrt{2}\hbar\omega_0}{3k_B T} \hat{O}_2 \hat{M}_y \right) &= Tr \left(\frac{\sqrt{2}\hbar\omega_0}{3k_B T} \hat{O}_2 N \sqrt{2}\gamma\hbar \hat{O}_2 \right) \\ &= \frac{2N\gamma^2\hbar^2}{3k_B T} Tr \hat{O}_2^2 \\ &= \frac{2N\gamma^2\hbar^2}{3k_B T} H_0 \end{aligned}$$

where we have used $Tr(\hat{O}_n^2) = 1$ and the expression for the Larmor frequency $\omega_0 = \gamma H_0$. We see that this expression is the same as the expression obtained for the equilibrium z-magnetization. So, the effect of the pulse is to rotate the z-magnetization about the y axis and onto the x axis which is the exact behavior observed in the classical case presented in Section A.1. However, this is the extent to which the magnetization can be described classically in the spin-1 system. By considering Equation A.70 one can calculate the transfer of coherence from one operator component to another through solution of the coupled differential equations. The magnetization can be thought of as a coherence which rotates in the 9D operator space and may be influenced by the action of RF pulses and the quadrupolar interaction. The solutions to these differential equations has been carried out extensively by Davis [30] and Schmidt *et al.* [38]. The effect of various RF pulse Hamiltonians and the quadrupolar interaction Hamiltonian on the set of operators described above are illustrated in Tables A.1 through A.3 and are presented in a notation similar to Schmidt *et al.* [38].

The density operator then evolves under the influence of the quadrupolar coupling for a time τ . Using the results presented in Table A.3, this is explicitly written as

$$\hat{\rho} = \frac{\sqrt{2}\hbar\omega_0}{3k_B T} (\cos \omega_Q \tau \hat{O}_2 - \sin \omega_Q \tau \hat{O}_5) \quad (\text{A.82})$$

where ω_Q is the quadrupole coupling frequency. Now, at this time a pulse of strength H_1 is applied along the $-I_y$ direction. The Hamiltonian for the pulse is $H_{RF} = -\sqrt{2}\hbar\omega_1 \hat{O}_2$. Under the influence of this Hamiltonian the density operator can be

rewritten as

$$\hat{\rho} = \frac{\sqrt{2}\hbar\omega_0}{3k_B T} (\cos \omega_Q \tau \hat{O}_2 - \sin \omega_Q \tau (\cos 2\omega_1 t_1 \hat{O}_5 + \frac{\sqrt{3}}{2} \sin 2\omega_1 t_1 \hat{O}_4 - \frac{1}{2} \sin 2\omega_1 t_1 \hat{O}_3)) \quad (\text{A.83})$$

and assuming that $\omega_1 t_1 = 90^\circ$, in the same manner as the first pulse, Equation A.83 can be written as

$$\hat{\rho} = \frac{\sqrt{2}\hbar\omega_0}{3k_B T} (\cos \omega_Q \tau \hat{O}_2 + \sin \omega_Q \tau \hat{O}_5). \quad (\text{A.84})$$

After the pulse the system is allowed to evolve during t under the influence of the quadrupolar interaction and can be written as

$$\begin{aligned} \hat{\rho} &= \frac{\sqrt{2}\hbar\omega_0}{3k_B T} [\cos \omega_Q \tau (\cos \omega_Q t \hat{O}_2 - \sin \omega_Q t \hat{O}_5) + \\ &\quad \sin \omega_Q \tau (\cos \omega_Q t \hat{O}_5 + \sin \omega_Q t \hat{O}_2)] \\ &= \frac{\sqrt{2}\hbar\omega_0}{3k_B T} [(\cos \omega_Q \tau \cos \omega_Q t + \sin \omega_Q \tau \sin \omega_Q t) \hat{O}_2 + \\ &\quad (\sin \omega_Q \tau \cos \omega_Q t - \cos \omega_Q \tau \sin \omega_Q t) \hat{O}_5] \\ &= \frac{\sqrt{2}\hbar\omega_0}{3k_B T} (\cos(\omega_Q [t - \tau]) \hat{O}_2 + \sin(\omega_Q [t - \tau]) \hat{O}_5) \end{aligned} \quad (\text{A.85})$$

where the sine and cosine double angle formulae have been employed for simplification.

At $t = \tau$ after the second pulse, the density operator is

$$\hat{\rho} = \frac{\sqrt{2}\hbar\omega_0}{3k_B T} \hat{O}_2 \quad (\text{A.86})$$

and taking the trace with the operator $M_y = \sqrt{2}N\gamma\hbar\hat{O}_2$ yields

$$\begin{aligned} (\rho \hat{M}_y) &= \text{Tr} \left(\frac{\sqrt{2}\hbar\omega_0}{3k_B T} \hat{O}_2 \sqrt{2}N\gamma\hbar\hat{O}_2 \right) \\ &= \frac{2N\gamma^2\hbar^2}{3k_B T} H_0 \text{Tr}(\hat{O}_2^2) \\ &= \frac{2N\gamma^2\hbar^2}{3k_B T} H_0 \end{aligned} \quad (\text{A.87})$$

Operator \hat{O}_n	$e^{i\sqrt{2}\alpha\hat{O}_1}\hat{O}_ne^{-i\sqrt{2}\alpha\hat{O}_1}$
\hat{O}_1	\hat{O}_1
\hat{O}_2	$\cos \alpha \hat{O}_2 - \sin \alpha \hat{O}_3$
\hat{O}_3	$\cos \alpha \hat{O}_3 + \sin \alpha \hat{O}_2$
\hat{O}_4	$\frac{1}{2}(3 \cos^2 \alpha - 1)\hat{O}_4 - \frac{\sqrt{3}}{2} \sin^2 \alpha \hat{O}_7 - \frac{\sqrt{3}}{2} \sin 2\alpha \hat{O}_6$
\hat{O}_5	$\cos \alpha \hat{O}_5 + \sin \alpha \hat{O}_8$
\hat{O}_6	$\cos 2\alpha \hat{O}_6 - \frac{\sqrt{3}}{2} \sin 2\alpha \hat{O}_4 - \frac{1}{2} \sin 2\alpha \hat{O}_7$
\hat{O}_7	$(1 - \frac{1}{2} \sin^2 \alpha) \hat{O}_7 - \frac{\sqrt{3}}{2} \sin^2 \alpha \hat{O}_4 + \frac{1}{2} \sin 2\alpha \hat{O}_6$
\hat{O}_8	$\cos \alpha \hat{O}_8 - \sin \alpha \hat{O}_5$

Table A.1: Unitary transformation of the operator \hat{O}_n about the operator \hat{O}_1

Operator \hat{O}_n	$e^{i\sqrt{2}\alpha\hat{O}_2}\hat{O}_n e^{-i\sqrt{2}\alpha\hat{O}_2}$
\hat{O}_1	$\cos \alpha \hat{O}_1 + \sin \alpha \hat{O}_3$
\hat{O}_2	\hat{O}_2
\hat{O}_3	$\cos \alpha \hat{O}_3 - \sin \alpha \hat{O}_1$
\hat{O}_4	$\frac{1}{2}(3 \cos^2 \alpha - 1)\hat{O}_4 + \frac{\sqrt{3}}{2} \sin 2\alpha \hat{O}_5 + \frac{\sqrt{3}}{2} \sin^2 \alpha \hat{O}_7$
\hat{O}_5	$\cos 2\alpha \hat{O}_5 + \frac{\sqrt{3}}{2} \sin 2\alpha \hat{O}_4 - \frac{1}{2} \sin 2\alpha \hat{O}_7$
\hat{O}_6	$\cos \alpha \hat{O}_6 - \sin \alpha \hat{O}_8$
\hat{O}_7	$(1 - \frac{1}{2} \sin^2 \alpha) \hat{O}_7 + \frac{1}{2} \sin 2\alpha \hat{O}_6 + \frac{\sqrt{3}}{2} \sin^2 \alpha \hat{O}_4$
\hat{O}_8	$\cos \alpha \hat{O}_8 + \sin \alpha \hat{O}_6$

Table A.2: Unitary transformation of the operator \hat{O}_n about the operator \hat{O}_2

which is precisely the magnitude of the equilibrium magnetization. So at $t = \tau$ after the second pulse the coherence is refocused along the y axis. Components of the density operator that lay along the x and y directions (ie \hat{O}_1 and \hat{O}_2) signify magnetization components which can induce an emf in the coil surrounding the sample and is detected in this measurement as a quadrupolar echo.

Operator \hat{O}_n	$e^{i\sqrt{\frac{2}{3}}\omega_q t \hat{O}_4} \hat{O}_n e^{-i\sqrt{\frac{2}{3}}\omega_q t \hat{O}_4}$
\hat{O}_1	$\cos(\omega_q t) \hat{O}_1 - \sin(\omega_q t) \hat{O}_2$
\hat{O}_2	$\cos(\omega_q t) \hat{O}_2 + \sin(\omega_q t) \hat{O}_1$
\hat{O}_3	\hat{O}_3
\hat{O}_4	\hat{O}_4
\hat{O}_5	$\cos(\omega_q t) \hat{O}_5 - \sin(\omega_q t) \hat{O}_6$
\hat{O}_6	$\cos(\omega_q t) \hat{O}_6 + \sin(\omega_q t) \hat{O}_5$
\hat{O}_7	\hat{O}_7
\hat{O}_8	\hat{O}_8

Table A.3: Transformation of the operator \hat{O}_n under the influence of first order quadrupolar coupling.

